Novel modelling, monitoring and state estimation methods for lithium-ion batteries

Xuan Liu
School of Electronic and Electrical Engineering
University of Leeds

A thesis submitted for the degree of Doctor of Philosophy

August 2021

Declaration

The candidate confirms that the work submitted is his own, except where work which has formed part of jointly-authored publications has been included. The contribution of the candidate and the other authors to this work has been explicitly indicated below. The candidate confirms that appropriate credit has been given within the thesis where reference has been made to the work of others.

Details of the publications and the ones under preparation that have been used in this thesis are as follows:

In chapter 2:

- Liu, X., Li, K. and Li, X., 2018. The electrochemical performance and applications of several popular lithium-ion batteries for electric vehicles - a review. Advances in Green Energy Systems and Smart Grid, pp.201-213.

  As the lead author, the candidate reviewed all the related materials and wrote the paper.

  Prof. Kang Li, my supervisor, supervised the work, provided excellent technical advice, modified and proof-read the draft of the paper.

  Dr. Xiang Li discussed the concepts of the paper.

- Liu, X. and Li, K., 2020. Energy storage devices in electrified railway systems: A review. Transportation Safety and Environment, 2(3), pp.183-201.

As the lead author, the candidate reviewed all the related materials and wrote the paper.

Prof. Kang Li, my supervisor, supervised the work, provided excellent technical advice, modified and proof-read the draft of the paper.

In chapter 3:

- Liu, X. and Li, K. State of charge estimation of lithium-ion batteries based on a temperature-compensated dual polarisation battery model using extended Kalman filter. (under preparation)

As the lead author, the candidate put forward ideas, performed the experiments, developed methodology and wrote the paper.

Prof. Li, my supervisor, supervised the work, provided excellent technical advice, modified and proof-read the draft of the paper.

In chapter 4:

- Liu, X., Li, K., Li X, Rente, B., Fabian, M. and Sun, T. A data-driven based temperature calibration method for Fiber Bragg-grating sensors in real-time battery temperature monitoring application. (under preparation)

As the lead author, the candidate put forward ideas, performed the experiments, developed methodology and wrote the paper.

Prof. Kang Li, my supervisor, supervised the work, provided excellent technical advice, modified and proof-read the draft of the paper.

Dr. Bruno Rente provided technical support for sensor installation and discuss the data analysis.

Dr. Matthias Fabian provided suggestions for experimental design.

Prof. Tong Sun provided suggestions on fiber sensor design.

In chapter 5:

- Liu, X., Li, K., Li X, Rente, B., Fabian, M. and Sun, T. Battery SOC estimation aided with non-embedded FBG strain sensors. (under preparation)

As the lead author, the candidate put forward ideas, performed the experiments, developed methodology and wrote the paper.

Prof. Kang Li, my supervisor, supervised the work, provided excellent technical advice, modified and proof-read the draft of the paper.

Dr. Bruno Rente provided technical support for sensor installation and discuss the data analysis.

Dr. Matthias Fabian provided suggestions for experimental design.

Prof. Tong Sun provided suggestions on fiber sensor design.

Acknowledgements

First and foremost, I would like to express my sincere gratitude to my supervisor, Professor Kang Li, for his continuous support and encouragement during my PhD study. His invaluable advice and research insights helped me build the foundation of my research and guided me to find the research directions. Especially in my most difficult times, his encouragement and patient guidance helped me to regain confidence. Without his inspiration and patience, I could not have reached this point.

I would like to offer my special thanks to all my colleagues, Dr. Shaojun Gan, Dr. Yanxia Wang, Dr. Xiang Li, Miss Yihuan Li, Miss Mingjia Yin and Mr Peiliang Sun. It was their kind help and support that made me have a wonderful time at University of Leeds.

I would also like to thank University of Leeds for sponsoring my research and PhD study, and offering me such a great opportunity for expanding my horizon.

Finally, I would like to express my deepest gratitude to my parents and wife for their love and support. Without their tremendous understanding and encouragement, it will be impossible for me to reach where I am today.

I dedicated this thesis to my parents.

Abstract

Lithium-ion batteries have received a lot of attention in recent years due to the advantages such as high energy density, high power density, high efficiency, long service life and environmentally friendly, etc. However, lithium-ion batteries can only operate in a narrow operation window, they are sensitive to the charging/discharging current, cut-off voltages and operating temperature. A battery management system (BMS) is essential for lithium-ion batteries, not only prevents the cells from operating in an inappropriate condition, but it also helps to improve the battery performance and efficiency. This thesis is focused on the development of some novel modelling, monitoring and state estimation methods for lithium-ion batteries.

A battery model plays an important role in BMS, which needs to be accurate and reliable. In this thesis, a dual polarisation (DP) battery model with temperature compensation is developed. The model parameters such as capacity, open circuit voltage (OCV), internal resistance and capacitance are identified via the recursive least squares (RLS) algorithm based on the experimental data tested at different temperatures. The developed model is then verified using the collected test data covering a range of temperature settings. To further verify the efficacy of the developed model, it is combined with the extended Kalman filter (EKF) algorithm to estimate the battery SOC at different temperature profile.

As the foundation of a BMS design, monitoring of the battery temperature profile should be comprehensive, accurate, reliable and timely. The conventional temperature sensors utilised in BMS are generally manufactured in probe form, which means that one probe can only measure the temperature of a single location. However, the temperature distribution of a battery is non-uniform, hence a single location temperature measurement is insufficient. Furthermore, in the applications such as grid energy storage and EVs, battery cells are generally connected in series and parallel as a battery pack composed of thousands of cells to provide required energy and power. If the temperature monitoring of each battery cell is required, the number of temperature sensors required will be enormous. Adopting such a large number of temperature sensors connected with numerous wires not only occupies large space but also brings considerable challenges to the wiring management in order to reduce the electromagnetic interference. In contrast to conventional temperature monitoring techniques, Fiber Bragg grating (FBG) temperature sensor is immune to electromagnetic interference, and can be integrated into a single optical fiber, which means that multi-points temperature measurements of a battery pack can be achieved using one fiber. Therefore, a battery test system using FBG sensors for battery temperature monitoring is firstly established in this work. Similar to other types of temperature sensors, FBG sensors also require regular calibrations to ensure accuracy and reliability. However, the conventional FBG sensor calibration method requires a high-standard laboratory environment and it can only be performed offline, which affects the normal operation of the ESS. To address the drawbacks of the conventional FBG temperature calibration method, a

novel data-driven based temperature calibration method for FBG sensors is then developed based on the data collected from the test system. Compared with the conventional temperature calibration method, the developed method can be used online without affecting the normal operation of the batteries. The efficacy of the developed method is verified using the collected test data.

Another key function of BMS is the estimation of battery internal sates, such as state of charge (SOC) and state of health (SOH). For battery SOC estimation, a strain based battery model is firstly developed using the back-propagation neural network (BPNN). The developed strain based BPNN model is then utilised for battery SOC estimation with the combination of the unscented Kalman filter (UKF) algorithm. The effectiveness of the developed SOC estimator is verified using the collected test data.

For SOH estimation, the battery ageing test is carried out on four lithium-ion cells at room temperature. A closed-loop SOH estimation method is then developed based on the UKF algorithm. The developed SOH estimation method combines the advantages of the capacity regression based method and the charing curve analysis method. The efficacy of the developed SOH estimation method is verified using collected from the battery ageing test.

Abbreviations

$BESS$	Battery based energy storage system
BMS	Battery management system
BP	Back propagation
$BPNN$	Back propagation neural network
CC	Constant current
$CC-CV$	Constant current constant voltage
CV	Constant voltage
DOD	Depth of discharge
DP	Dual polarisation
DST	Dynamic stress test
DTW	Dynamic time warping
ECM	Equivalent circuit model
EKF	Extended Kalman filter
EMD	Empirical mode decomposition
ESS	Energy storage system
EV	Electric vehicles
FBG	Fiber Bragg gating
FCM	Fuzzy C-means
FRA	Fast recursive algorithm
$HPPC$	Hybrid pulse power characterisation
ICA	Incremental capacity analysis

IMF	Intrinsic mode function
KNN	K-nearest neighbours
LCO	Lithium cobalt oxide
LFP	Lithium iron phosphate
LMO	Lithium manganese oxide
$LOCO$	Leave one cycle out
LS	Least square
$LSTM$	Long-short time memory
LTO	Lithium titanium oxide
MAE	Mean absolute error
$MaxAE$	Maximum absolute error
ME	Mean error
MSE	Mean square error
NCA	Nickel cobalt aluminium
NMC	Nickel manganese cobalt oxide
NN	Neural network
OCV	Open circuit voltage
$P2D$	Pseudo two dimensional
PCA	Principal component analysis
PCM	Phase change material
PDE	Partial differential equation
PDF	Probability density function
$PNGV$	Partnership for a new generation vehicle
$PSFB$	Poly-sulphide flow battery
PSO	Particle swarm optimisation
RTD	Resistance temperature detector
RBF	Radial basis function

RFB	Redox flow battery
RLS	Recursive least squares
$RMSE$	Root mean square error
RNN	Recurrent neural network
SEI	Solid electrolyte interphase
SOC	State of charge
SOE	State of energy
SOH	State of health
SOP	State of power
SPM	Single particle model
SVM	Support vector machine
UKF	Unscented Kalman filter
UT	Unscented transformation
$VRFB$	Vanadium redox flow battery
$ZBFB$	Zinc-bromine flow battery

Contents

List of Figures

List of Tables

Chapter 1

Introduction

In recent years, the public has paid more attention to the global warming and environmental sustainability challenges facing the mankind. A legally international treaty on climate change - the Paris Agreement was adopted by 196 countries on 12 December 2015 which aims to limit global warming to well below 2 °C compared to pre-industrial levels [4]. In order to achieve this long-term temperature goal, the governments of various countries have developed different strategies and policies to reduce carbon emissions. In the UK, new vehicles powered wholly by petrol and diesel will not be sold from 2030. The government of the UK has also legislated to achieve net-zero emission by 2050 - to strike a balance between the amount of greenhouse gas produced and the amount removed from the atmosphere. On the path to net-zero emissions, energy storage system (ESS) has been widely utilised in various sectors, such as industry, transportation and building, etc.

ESS is a system that can harvest energy from various sources and convert the harvested energy to the required energy forms for later use [5]. Today, various forms of ESSs have been proposed and utilised in different applications. Among various types of ESSs, lithium-ion battery based ESS stands out due to the advantages in terms of energy density, power density, cycle efficiency, self-discharge, storage duration, service life, capital cost and environmental impact [6].

1.1 Lithium-ion battery

The prototype of lithium-ion battery was invented by Akira Yoshino in 1985, then a commercial lithium-ion battery was developed by Sony and Asahi Kasei in 1991 [7]. Significant progress has been made on lithium-ion battery technologies over the past 30 years, including materials improvements in anode, cathode, electrolyte and separator, and the enhancements in structure design [8].

1.1.1 Lithium-ion battery working principles

A typical lithium-ion battery usually consists of an external can, internal layers and some protection elements, as depicted in Fig. 1.1. The internal layers are composed of anode, cathode and separator and soaked in the electrolyte. The internal layers can be rolled into various shapes (e.g. cylinder or prismatic) according to different needs. The anode is usually made of lithium-doped carbon material, and the cathode is generally composed of lithium-containing metal oxide materials. In order to facilitate chemical reactions, modern lithium-ion batteries generally deploy porous electrodes to increase the active area [8]. The separator is a permeable membrane which is placed between the anode and cathode to prevent a short circuit.

The essence of the operational mechanism of lithium-ion batteries is the movement of lithium ions inside the battery, as shown in the the schematic diagram Fig. 1.2. In the charging process, lithium ions move through the electrolyte from the cathode (positive electrode) to the anode (negative electrode) and attach to the carbon materials. During the discharge process, the lithium ions flow back through the electrolyte from the anode to the cathode. The electrons produced at

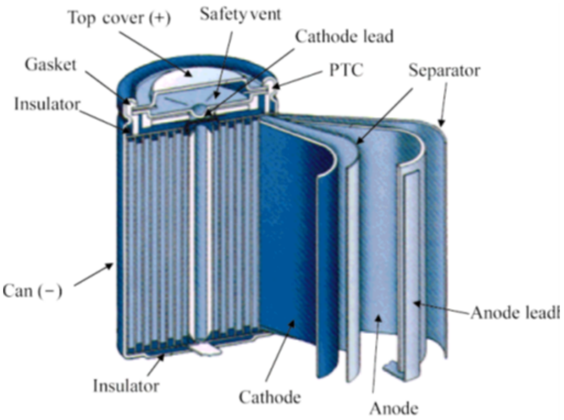

Figure 1.1: Lithium-ion battery structure [1]

the anode flow through external circuit, producing the load current.

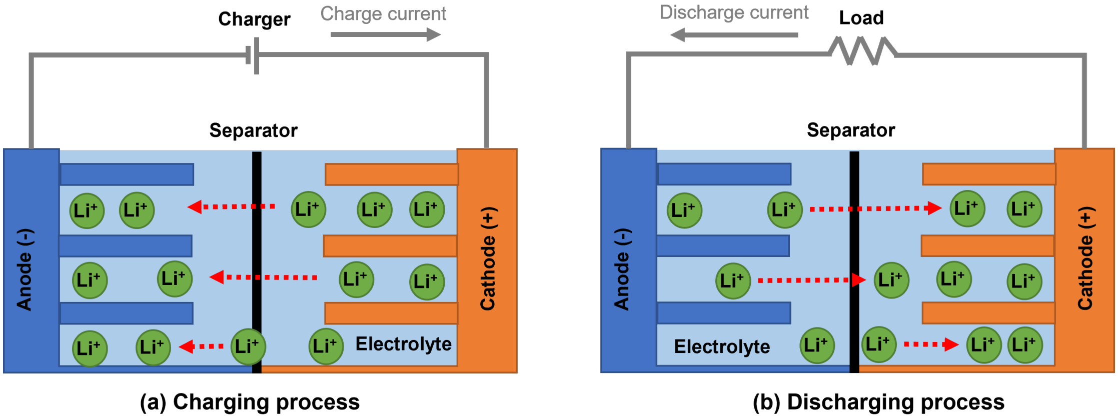

(a) Charging process

(b) Discharging process

Figure 1.2: Working principle of lithium-ion battery

Take the lithium-iron phosphate ($LiFePO_4$) battery as an example, the reaction during charging at the cathode is

$$LiFePO_4 \rightarrow FePO_4 + Li^+ + e^-$$

and at the anode is

$$Li^+ + e^- + C_6 \rightarrow LiC_6$$

During discharging, the reactions occur reversely.

1.1.2 Lithium-ion battery applications

Lithium-ion batteries are widely used in portable devices (e.g. mobile phones, tablets, laptops, wearable devices, etc.) due to the advantages of high energy density, long service life, no memory effect and low material cost, etc. In recent years, lithium-ion batteries have also been widely utilised in transportation and power grids to improve energy efficiency and reduce greenhouse gas emissions.

1.1.2.1 Applications of lithium-ion batteries in electric vehicles

Electric vehicles (EVs) are recognised as one of the best alternatives to internal combustion engine (ICE) based vehicles in order to improve fuel efficiency and reduce emissions in the transportation sector. Generally speaking, EVs can be divided into three categories, such as battery EVs (BEVs), hybrid EVs (HEVs) and plug-in hybrid EVs (PHEVs) [9]. A BEV has one or more electric motors powered by a large on-board battery pack. Battery is the only power source for BEVs. A HEV generally has two power sources, e.g., a downsized ICE and a battery pack. Since the ICE operates at low speed with very low fuel efficiency [10], a HEV generally rolls under electric power when it starts. The ICE then kicks in when the vehicle achieves specific speed. Unlike BEVs, the battery pack of a HEV generally can only be charged during the regenerative braking process. A PHEV is a particular type of HEV whose battery can be charged by plugging into the grid. Compared with HEVs, PHEVs generally can travel a longer distance on electric power alone due to their increased battery size and ability to recharge from the grid. Compared with the conventional vehicles powered by ICEs, EVs have the following advantages:

- Higher efficiency. The average tank-to-wheel efficiency of a typical ICE car is around 30% [11] and it will fall significantly in city drive due to the frequent stop-and-start operations [12]. On the contrary, the ICE in a HEV generally operates with high efficiency. The battery-to-wheel efficiency can reach up to 87% [13].

- Less emissions. A BEV produces no emission during the operation, and a HEV produce 30% less emission than a conventional ICE vehicle in terms of tank-to-wheel emission [12]. Considering the overall well-to-wheel, EVs and HEVs still offer less emissions than the ICE vehicles [14].
- Better driving experience. Compared with ICE vehicles, EVs have less moving parts in the powertrain. Therefore, EVs can generate lower propulsion noise and less vibrations than the ICE vehicles. Moreover, EVs can offer faster accelerations because the torque output of an electric motor can increase from zero to peak almost instantaneously.

1.1.2.2 Applications of lithium-ion batteries in power grid

In recent years, power systems have been gradually shifted from centralised to decentralised energy generation to improve power supply security and acceptance of renewable generations, and to reduce transmission loss. In order to effectively realise the decentralisation of the power grid, lithium-ion batteries have been widely used in modern power systems to provide various grid services [15; 16]. Generally, the applications of lithium-ion batteries in power grid can be grouped into the following three categories:

1. Generation side:
    - Renewable energy integration. Lithium-ion batteries are commonly used for renewable energy sources (RES) integration which converts

the variable intermittent output power from RES into a relatively stable output.

- Peak shaving. Lithium-ion batteries can provide a fast response to supply peak power demand and avoid increasing generating capacity to meet the peak demand of a highly variable load. The lithium-ion batteries recharge during off-peak periods for later use.
- Frequency regulation. The mismatch between generation and load may cause grid frequency deviations. Lithium-ion batteries can be charged or discharged to adjust the grid frequency and maintain the grid frequency within the required limits.
- Spinning reserve. Lithium-ion batteries maintain a specific SOC value to respond to a generation outage. Lithium-ion batteries can offer a response within milliseconds or minutes.

2. Transmission and distribution side:

   - Network investment deferral. Lithium-ion batteries can be utilised to provide enough incremental capacity for the transmission system in order to defer the need for the investments.
   - Voltage support. Lithium-ion batteries provide voltage support by performing as dynamic reactive power supplies, injecting or absorbing reactive power in the transmission systems.
   - Congestion relief. Grid congestion often occurs when the heat or electric capacity of the transmission line cannot meet the power transmission demand. Congestion of the power grid may increase line dissipation, reduce transmission efficiency, and even cause power outages. Lithium-ion batteries can be installed at the congested locations of the transmission systems to alleviate the congestion. When the transmitted

energy exceeds the limit of the transmission line, the excess energy will be absorbed by the lithium-ion battery (via the charging process) and released (via the discharging process) during the peak time of demand.

3. End-user side:

   - Power quality and reliability enhancement. Lithium-ion batteries can be utilised to improve the power quality and mitigate the events such as voltage variations, lower power factors, harmonics and interruptions in service.
   - Energy management. Lithium-ion batteries can be used to reduce the overall electric service costs by load shifting (peak shaving). Through load shifting with lithium-ion batteries, consumers can reduce their demand charges.

1.2 Battery management system

In order to guarantee the safety and efficiency of the operations, a BMS is essential to ensure the batteries can operate safely and efficiently within the proper voltage and temperature windows. A BMS includes multiple functionalities to monitor, protect, control and manage the batteries. Generally, the functionalities of BMS can be summarised as:

1. Monitoring: A BMS generally monitors the batteries by taking measurements of battery terminal voltage, current, ambient and surface temperatures, etc. Real-time battery monitoring also provides necessary information for other BMS functionalities. In other words, real-time battery monitoring is a prerequisite for other BMS functionalities.

2. Protection: It is one of the necessary functions of a BMS to avoid the battery operating under unsafe conditions. A battery management system should be able to effectively avoid improper operations such as over-current, over-voltage, under-voltage, over-temperature, under-temperature, over-fast temperature rise, over-pressure, over-charging, over-discharging, electric leakage, and short circuit. Moreover, the battery management system also needs to be able to detect and diagnose faults during the operation. These faults generally include sensor fault, actuator fault, battery fault and communication fault, etc. When the BMS detects a fault, it needs to respond properly, such as cutting off the circuit and alarming.

3. State estimation: In addition to the directly measurable signals, the internal states of a battery such as the state of charge (SOC), state of power (SOP), state of energy (SOE), state of health (SOH) and internal temperature, etc. can also significantly affect the battery performance. When these battery internal states exceed the appropriate intervals, it will cause battery performance degradation and even lead to safety issues. However, these internal states generally cannot be measured directly or accurately. As important indicators of battery operating status, the battery internal states thus need to be estimated in real-time to ensure the battery can operate safely and efficiently.

4. Charging/discharging control: The charging and discharging control units should be integrated into the BMS in order to adjust the battery charging/discharging current and voltage within proper windows. Properly adjusting the battery charging/discharging current and voltage can not only avoid the occurrence of unsafe operations but also can improve the battery operation efficiency and prolong the service life.

5. Thermal management: According to the temperature distribution within the battery pack, the BMS needs to control the thermal management units to ensure all the cells inside the battery pack can operate within the proper temperature range. When the battery temperature is too low, the battery needs to be pre-heated. When the battery temperature is too high, an appropriate cooling can suppress temperature rise and avoid thermal runaway. The most commonly used cooling methods include air-cooling, liquid-cooling, refrigerant-cooling, phase change material (PCM) based cooling and heat pipe systems.

6. Battery equalisation: Since there could be numerous battery cells in one battery pack, balancing these cells is the key to battery pack performance optimisation. Cell variance and unbalanced external circuits are the main origins that cause battery imbalance. The performance of a battery pack is generally limited by the worse cells. If no proper equalisation is applied, the imbalance situation will deteriorate. When the battery pack is seriously unbalanced, it may cause a safety hazard. Therefore, the equalisation of battery cells is necessary to prolong battery pack service life and ensure battery safety operation. The most utilised battery equalisation methods include passive balancing and active balancing. The essence of passive balancing is to waste the electric energy on the most charged battery to heat energy. The cost and complexity of passive balancing are relatively low, but it has limited energy efficiency. The essence of active balancing is to transfer the energy from the most charged cells to the least charged cells via the power electronic device, such as capacitors, inductors or DC-DC converters. Compared with the passive balancing method, active balancing can effectively improve energy efficiency and reduce heat generation during the balancing process, but it is relatively complicated and costly.

7. Other functionalities: A BMS is also desirable to conduct online calibrating, program update and downloading, etc. Networking and communication functionalities are therefore generally integrated into the BMS. Moreover, the BMS also stores the essential data of the batteries, such as battery SOC, SOH, cycle numbers, operation profile and fault code, etc.

1.3 Research motivations and contributions

Despite the rapid development of battery management system technology in recent years, there are still some challenges in current BMS [17; 18; 19], such as battery modelling, signal monitoring and internal states estimation, etc.

1.3.1 Battery modelling

As the first step of BMS design, a battery model plays a vital role in BMS development. An accurate and reliable battery model can not only ensure the safe operation of the battery, but also help to improve the system efficiency, prolong the service life, and avoid unnecessary damage. In recent years, many battery models have been developed with different accuracy, reliability and complexity. As one of the most popular battery modelling methods, equivalent circuit models (ECMs) utilise electronic components (such as voltage source, resistors, capacitors and impedance) to describe the dynamic electric behaviours of batteries. ECMs generally have a relatively simple model structure, and the model parameters are easy to identify. Therefore, ECMs have gained a lot of interest in real-time applications.

The existing studies related to battery ECM modelling mainly focus on the model configuration. Various structures of battery models have been developed, such as the Thevenin model, due polarisation (DP) model, 3rd order RC model and

PNGV model, etc. In addition to the selection of model structure, the temperature influence on model accuracy and reliability is seldom mentioned in the literature. It is worth noting that as a critical factor, the temperature can significantly affect the battery performance and limit its application [20]. It is still a challenge to build a battery model that can perform well at different temperatures.

1.3.2 Battery temperature monitoring

As the foundation of a BMS, battery temperature monitoring should be accurate, reliable and timely. Real-time battery temperature monitoring not only protects the battery from operating in unsafe conditions but also helps to develop advanced battery control strategies. Since the battery is a sealed object, only the ambient and surface temperatures of a battery can be measured directly. The most commonly used temperature sensors in BMS include thermistors, resistance temperature detectors and thermocouples, etc. Although these temperature sensors can usually provide accurate temperature measurements, they all face the same issue - they are generally manufactured in probe form, which means that one probe can only measure the temperature of a single location. However, the temperature profile of single location is non-uniform inside and outside, hence single location measurement is insufficient. Further, due to the limitation of electrochemical characteristics of the materials inside the battery, the voltage and capacity of a single cell are very limited. Therefore, in the applications such as grid energy storage and EVs, battery cells are generally connected in series and parallel as a battery pack composed of thousands of cells to provide sufficient energy and power. However, if the temperature monitoring of each battery cell is required, the number of temperature sensors required will be enormous. Adopting such a large number of temperature sensors not only affects the overall energy density and power density of the energy storage but may also bring significant challenges to the wiring management. Finally, the batteries are often operated in harsh environment, including strong electromagnetic inferences, which cause signal drifts and corruptions.

1.3.3 Battery SOC estimation

As a crucial function of the BMS, the battery SOC estimation needs to be accurate and reliable to ensure the batteries can operate safely and efficiently. SOC is the level of charge of a battery relative to its available capacity. It determines the ratio of electric charge left in the battery available for further operation. Accurate SOC estimation also helps with battery voltage prediction, SOE estimation, SOP estimation, etc.

Despite the demanding necessity, accurate SOC estimation is difficult to acquire in real-time since SOC is an implicit state of battery that cannot be measured directly or accurately. Many approaches have been developed for battery SOC estimation and they can be mainly divided into two categories: model-free SOC estimation methods and model-based SOC estimation methods. The most commonly used model-free SOC estimation methods include the Ampere-hour method and OCV method. These methods are simple and easy to implement. However, these methods require certain conditions to work well. In Ah method, the initial SOC value must be a known value without error. If there is an error in the initial value of the SOC, the subsequent SOC estimation of the battery will be biased. Additionally, Ah method has a high requirement for the accuracy of battery current measurement since the measurement error of current will be accumulated during the entire SOC estimation. In OCV method, the battery should be accurately determined in advance. However, the battery OCV is also difficult to estimate during the charging and discharging processes. In order to overcome the disadvantages of the model-free SOC estimation methods, the model-based methods for SOC estimation have been widely utilised. The battery SOC can be estimated via one or more proper battery models. Many battery models have been used for SOC estimation, such as the electrochemical models, ECMs and neural network (NN) models, etc. Moreover, different types of observers and filters also have been applied for battery SOC estimation. However, most of the research on battery SOC estimation build the models using test data taken at room temperature. It is still a challenge to ensure the accuracy and reliability of battery SOC estimation at different temperatures.

Another point worth noting is that almost all current SOC estimation methods are developed based on measurable electrical signals, such as battery terminal voltage and current. However, the measurements of current and voltage are usually corrupted by noise. As one of the main sources of SOC estimation errors, sensor noise significantly affects the accuracy and reliability of SOC estimation. It also worth noting that the practicality of electrical measurements is also limited, such as the issues of insulation, corrosion and electromagnetic compatibility, etc.

1.3.4 Battery SOH estimation

SOH is a figure of merit of the condition of a battery compared to its ideal conditions. An accurate SOH estimation helps to manage the battery operation to prolong the battery service life, avoid failures and optimize the battery maintenance plan. Even though the importance of accurate SOH estimation is very high, there still does not exist a consensus on how SOH should be determined since it does not correspond to a particular physical quality. The parameters that can be used to determine battery SOH include capacity, internal resistance, self-discharge rate, ability to accept a charge, and the total amount of energy charged/discharged, etc.

For the applications in EVs and grid energy storage, battery remaining available capacity is usually utilised as the indicator for SOH estimation since the cyclability and deliverability of the battery need to be prioritised. As the easiest and most precise method of SOH estimation, the battery SOH can be determined directly if the battery maximum available capacity can be accurately measured. The Ampere-hour method is usually used to calculate the battery maximum available capacity via counting the charge transferred through the battery during the full charging or discharging process. Direct capacity measurement can theoretically provide very high accuracy by using high-precision measurement techniques. Therefore, this method is usually utilised for capacity calibration in the laboratory. However, this method is not suitable for practical applications because it is difficult to stop and measure the fully charged capacity for energy storage in operating. Moreover, the accuracy of the remaining capacity measurement highly depends on the precision of the current sensor. The errors in current measurement will be accumulated until the end of the entire process.

1.3.5 Research contributions

The main contributions of this work can be summarised as follows:

1. In order to build an accurate and reliable battery model which can operate at different temperatures, a DP model with temperature compensation is developed in this thesis. The developed temperature compensated battery model can operate in a wide range of temperature (0 °C to 50 °C) with accurate and reliable performance in battery terminal voltage prediction. Furthermore, the developed temperature compensated battery model is utilised for SOC estimation at various temperatures. The test results indicate that the developed temperature compensated battery model can not only accurately predict the battery terminal voltage at different temperatures, but also contribute to the battery SOC estimation.

2. A cutting-edge sensing technology - fiber sensing technology is utilised in battery temperature monitoring. Firstly, a battery temperature test platform based on Fiber Bragg grating (FBG) sensors is established. Multi-points temperature measurements are obtained using one optical fiber with the integration of FBG sensors. The conventional FBG temperature calibration method generally requires a high-standard laboratory environment and it can only be performed offline. In order to overcome the drawbacks of the conventional FBG calibration method, a data-driven based FBG sensor temperature calibration method is then developed. The validation results show that the developed method has good accuracy and reliability in battery temperature monitoring. Compared with the conventional temperature calibration method, the developed method can be used online without affecting the normal operation of the batteries. Moreover, the developed method does not require a high-standard test requirement, and it is more friendly in engineering applications.

3. A novel battery SOC estimation method based on FBG sensing technology is developed. The developed method can estimate battery SOC without the measurement of battery voltage and operates as a strain-based SOC estimator. In this case, the battery SOC estimation will not be affected by the error of voltage measurement. This method is suitable for the applications where the battery voltage cannot be measured. Furthermore, the developed SOC estimation can also perform battery SOC estimation aided with battery voltage measurement as an enhanced strain based SOC estimator. In this case, the robustness of the SOC estimator is enhanced, and the influence of voltage measurement error on SOC estimation is also significantly reduced. The enhanced SOC estimator is suitable for the applications where battery voltage cannot be accurately measured.

4. An adaptive filter based SOH estimation method is developed by combining the advantages of the capacity regression model based method and the charging curve analysis based methods. The charging analysis based method is utilised as a feedback system for the capacity regression-based method to provide a reference of capacity estimation. Meanwhile, the capacity regression model based method is utilised to provide experience for the charing curve analysis based method to enhance the robustness. Compared with the conventional SOH estimation methods, the developed SOH estimation method can offer more accurate and reliable SOH estimation performance.

1.4 Outline of thesis

This thesis mainly deals with the development of BMS algorithms for lithium-ion batteries, including battery modelling, real-time temperature monitoring, battery SOC and SOH estimation. The remaining chapters of this thesis are organised as follows:

- In chapter 2, a literature survey about battery modelling, sensing technologies and states estimation techniques is presented. A brief introduction of the operation principles and properties of lithium-ion batteries is firstly given. Different battery modelling methods are then compared and analysed. A cutting edge sensing technology for BMS - FBG sensing technology is then introduced in detail. Finally, the current methods in battery SOC and SOH estimation have been reviewed.
- In chapter 3, a DP model with temperature compensation is developed. The model parameters are identified by the recursive least squares (RLS) algorithm via the experimental tests at different temperatures. The model

parameters such as battery capacity, OCV, internal resistances and capacitances are modelled as the variables which depend on the battery operating temperatures. The efficacy of the developed temperature compensated model is validated at different temperatures. Furthermore, the developed temperature compensated DP model is then utilised for SOC estimation at various temperatures with the application of the extended Kalman filter (EKF) algorithm.

- In chapter 4, a data-driven based FBG sensor temperature calibration method is developed. Firstly, the Fuzzy C-means algorithm is used to extract the linear relationship between the measured wavelength shift and temperature variation. The empirical mode decomposition (EMD) technique is then applied to decompose the remaining wavelength information. The intrinsic mode functions (IMFs) and the residual achieved by the EMD technique are classified according to their frequency characteristics. The rest wavelength information is further modelled as a system compensation that depends on the cell SOC and cycle number. Therefore, the battery temperature can be determined in real-time according to the information of the wavelength shift measured by the FBG sensor, the battery SOC and cycle number. Finally, the developed battery temperature monitoring method is validated via experimental tests.

- In chapter 5, a strain based SOC estimator is developed for SOC estimation. Unlike insert FBG sensors inside the cell, the FBG sensors are mounted on the surface of the cell in this work to collect the strain data during the charging and discharging processes. The non-embedded layout will not cause any damage to the battery, and thus it will not affect the performance of the battery in terms of lifespan and maximum usable capacity, etc. Moreover, the non-embedded layout also can be flexibly installed or uninstalled based on application needs, which means that it is more friendly in engineering applications. A back propagation neural network (BPNN) based model is developed to predict the strain information according to the battery SOC. The model structure is determined by using the leave one cycle out (LOCO) method for the charging and discharging processes. For comparison, a combined model is built for battery terminal voltage prediction. Both the strain based model and the voltage based model are used for SOC estimation combined with the utilisation of UKF. In order to further enhance the estimation accuracy of the strain based SOC estimator, an enhanced strain based SOC estimator is then developed by combining the strain based model and the voltage based model.

- In chapter 6, two popular types of SOH estimation methods, namely the capacity regression model and the charging curve analysis based method have been reviewed. In order to improve the SOH estimation accuracy, an adaptive filter based SOH estimation method is developed in this chapter by combining the advantages of the capacity regression model and the charging curve analysis method. The charging curve analysis method is utilised as a feedback system for the capacity regression model to provide a reference for capacity estimation. Meanwhile, the capacity regression model is utilised to provide experience for the charing curve analysis method to enhance the robustness. Comparing with the conventional SOH estimation methods, the developed SOH estimation method has advantages in terms of accuracy and reliability.
- Chapter 7 concludes this thesis. The research contributions in this work and some suggestions for future work are summarised.

Chapter 2

Literature survey

This chapter focuses on the literature survey about the properties of lithium-ion battery and the development of lithium-ion battery BMS. Firstly, a comprehensive comparison of common types of batteries is presented. Compared with other types of batteries, lithium-ion battery has clear advantages in terms of energy density, power density, operational temperature, service life and environment impact, etc. Thus, some key electrical and thermal properties of lithium-ion battery are then reviewed. The understanding of these lithium-ion battery properties can not only ensure the battery safe operation, but also contribute to the further development of the BMS. Different types of lithium-ion battery models then are reviewed and some of the typical battery models have been introduced in details. Moreover, the techniques of temperature monitoring that are commonly used in battery based ESS have been presented. Then, the methods of battery internal states estimation, such as SOC estimation and SOH estimation are presented. Finally, the applications of FBG sensing technology in BMS have been comprehensively reviewed.

2.1 Comparison of different types of batteries

Batteries can be seen as one of the most widely used energy storage devices which store electricity in the form of chemical energy during the charging process and convert the stored chemical energy to electricity during the discharging process. A typical battery is generally composed of three key components, the anode (negative electrode), the cathode (positive electrode) and the electrolyte. Nowadays, many types of batteries have been invented to meet various operating requirements by using different chemical materials in the electrodes. In this section, various types of battery based ESSs have been reviewed, including lead-acid batteries, nickel-based batteries, sodium-based batteries, lithium-ion batteries and redox flow batteries.

2.1.1 Lead-acid batteries

As the oldest type of rechargeable battery, lead-acid battery was invented in 1859 by Gaston Planté [21]. Lead-acid batteries have the advantages such as low cost, ease of management, high reliability and technological maturity. Therefore, they are widely utilised in cost-sensitive applications. The anode of a typical lead-acid battery is made of metallic lead in spongy form, and the cathode is generally made of lead oxide materials. In order to prevent short circuits, the anode and cathode are generally separated by a microporous membrane-based separator. The anode, cathode and separator are immersed in the electrolyte that is made of dilute sulphuric acid. During the charging process, lead and lead oxide are produced at the surface of the electrodes via the chemical reactions of lead sulphate and water. On the contrary, the anode and cathode react with the electrolyte to produce lead sulphate and electric energy during the discharging process. Thus, there will be more sulphate crystals produced if the lead-acid battery is over-discharged. The sulphate crystals may break the separator and even cause short circuits [22; 23]. The conventional lead-acid battery has disadvantages in energy density and cycle capability, various types of enhanced lead-acid batteries thus have been developed, such as valve-regulated lead-acid batteries, deep-cycle lead-acid batteries and advanced lead-acid batteries [24; 25]. However, all of these lead-acid batteries face the same issue - the utilisation of toxic metal lead may cause metal pollution during the manufacturing process and the disposal state [26].

2.1.2 Nickel-based batteries

Nickel Cadmium (Ni-Cd) battery was invented in 1899, then it has had a high market share under the continuous improvement of performance until the emergence of lithium-ion batteries [27; 28]. The anode of a typical Ni-Cd battery is generally made of metallic cadmium and the cathode is generally made of nickel oxide hydroxide. The anode and cathode are immersed in the electrolyte that is made of alkaline potassium hydroxide. Since the chemical reactions during the charging process are endothermic, which can effectively avoid significant temperature rise during the charging process. Therefore, Ni-Cid batteries are capable of fast charging operations. Moreover, Ni-Cd battery has a wider operating temperature window compared with the other types of batteries. However, Ni-Cd faces two main issues, the 'memory effect and the high self-discharge rate. The 'memory effect' is also known as the 'lazy battery effect', it refers to the cell gradually lose its maximum capacity if it recharges after partial discharging [29]. The high self-discharge rate can significantly affect the overall operating efficiency of the ESS. Another drawback of Ni-Cd battery is the lower operating voltage, which means that more Ni-Cd cells are required to meet a specific operating requirement in voltage. Furthermore, it is difficult to balance the Ni-Cd cells inside a pack since each cell may have different self-discharge rates. Additionally, Ni-Cd batteries may cause environmental hazards since toxic heavy material (i.e. cadmium) is utilised [30].

To address the disadvantages of Ni-Cd batteries, Ni-MH batteries have been developed in order to achieve better performance in energy density and cycle capability. Ni-MH battery is more environmentally friendly than the Ni-Cd battery since its anode is generally made of hydride alloy. Although the ‘memory effect’ of Ni-MH batteries has been significantly improved, the high self-discharge rate is still a challenge to be solved.

2.1.3 Sodium-based batteries

The working principle essence of sodium-based batteries is the movement of sodium ions between the anode and cathode. The anode of a typical sodium-based battery is generally made of molten sodium. Depending on the materials utilised in the cathode, a variety of sodium-based batteries have been developed. Sodium sulphur (NaS) and sodium nickel chloride ($NaNiCl_2$) batteries are the two types of the most commonly used sodium-based batteries. For a typical NaS battery, its cathode is generally made of molten sulphur, and the electrolyte is generally made of solid alumina ceramic materials. NaS batteries have the advantages such as high energy density, high power density, negligible self-discharge, long service life and low material cost [31]. However, the requirement of high operational temperature (in the range between 300 °C to 350 °C) is the main disadvantage of NaS batteries [32].

The sodium nickel chloride battery was developed in 1985 under the Zeolite Battery Research Africa Project. Therefore, sodium nickel chloride battery is also known as ZEBRA battery. Compared with NaS battery, ZEBRA battery has a higher operating voltage level and better safety features [33] but lower energy density [34]. ZEBRA battery is a typical molten-salt battery that requires a high operational temperature. The optimal operating temperature of a ZEBRA is generally in the range of 270 °C to 350 °C [35]. However, there are limited applications that can meet such high operating temperature requirements. Therefore, various types of sodium-based batteries that can operate at room temperature have been proposed [36; 37; 38]. However, the research in this area is still in its infancy and the related technologies are not currently mature enough. There is still a long way to go for their commercialisation.

2.1.4 Lithium-ion batteries

In recent years, the market share of lithium-ion batteries in portable has increased significantly due to their widespread applications in portable devices and EVs [28]. The essence of lithium-ion battery working principle is the movement of lithium-ions inside the cell. The lithium ions move from the cathode to the anode during the charging process and travel back in the discharging process. Compared with other rechargeable batteries, lithium-ion batteries have advantages such as high energy density, high power density, long service life and no 'memory effect', etc. A wide range of lithium-ion batteries has been developed by adapting different materials in the electrodes, such as Lithium Cobalt Oxide (LCO) battery, Lithium Manganese Oxide (LMO) battery, Lithium Nickel Manganese Cobalt Oxide (NMC) battery, Lithium Nickel Cobalt Aluminium Oxide (NCA) battery, Lithium Iron Phosphate (LFP) battery and Lithium Titanate (LTO) battery, etc [39]. Depending on the characteristics of the cells, lithium-ion batteries can be divided into two main categories, namely high-power batteries and high-energy batteries.

LFP batteries and LMO batteries are two typical high-power lithium-ion batteries. They can provide relatively high current rates in both the charging and discharging processes. For example, the maximum continuous and pulse discharging current rates of some specialised LFP batteries can reach 3C and 10C, respectively [39]. LFP batteries can offer stable output power output over a wide range of SOC because their discharge voltage curves are quite flat [40]. Moreover, LFP batteries also have better safety features and cycle capability [41]. However, the main shortcoming of LFP batteries is the relatively low energy density. Although the self-discharge rate of a typical LFP battery is much lower than the lead-acid and nickel-based batteries, it is still relatively high in comparison with the other lithium-ion batteries. Compared with LFP batteries, LMO batteries can offer better performance in terms of energy density and self-discharge rate, but the cycle capabilities of LMO batteries are constrained. Both NMC and NCA batteries are nickel-based lithium-ion batteries. They can offer higher specific energy due to the utilisation of cobalt material, but this also leads to higher material costs. In some applications such as EVs, LMO batteries blend with NMC enhance the energy density and prolong the service life [42]. However, NMC and NCA batteries still face some challenges in terms of cycle capability and stability [41]. While LTO batteries have emerged as one of the most promising lithium-ion batteries due to their excellent performance in power capability and cycle life [43], the main disadvantages of LTO batteries are the relatively low energy density and high material cost [44].

2.1.5 Redox flow batteries

Redox flow battery (RFB) is a type of flow battery that employs two active materials in liquid form to provide electrical energy. The two active solutions are separately stored in the external tanks, namely the anolyte tank and the catholyte tank. The active solutions are pumped through the system, reduction and oxidation reactions then occur on both sides of the separator which is made of an ion-exchange membrane. The energy capacity of the RFB is related to the volume of active solutions, and the power capacity depends on the size of the reaction area. In comparison with conventional batteries, RFBs have advantages such as excellent scalability, long cycle life and fast response time [45]. RFBs have almost no self-discharge because the electrolytes are stored in the external tanks separately. Furthermore, the cell temperature of RFBs can be handled easily due to the special structure design. However, if RFBs operate under inappropriate temperatures, solution precipitation may occur, which leads to capacity fading and even cause a failure. Therefore, the operating temperature of a typical RFBs is generally limited between 15 to 35 °C [46]. Moreover, low specific energy and power are the main reasons that RFBs cannot be widely utilised [47].

A comprehensive comparison of common types of batteries is represented in Table 2.1. It can be seen that compared with other types of batteries, lithium-ion battery has obvious advantage in terms of energy density, power density, operational temperature, self-discharge rate, life time and environment impact. However, lithium-ion batteries can only operate within suitable operation windows in terms of voltage and temperature. Exceeding the restrictions of these windows can result in battery performance degradation and even lead to safety issues such as fire and explosion. Therefore, the battery management system is indispensable in ensuring the batteries can operate safely and reliably.

2.2 Key properties of lithium-ion battery

Lithium-ion batteries can only operate in a narrow operation window, they are sensitive to the charging/discharging current, cut-off voltages and operating temperature. Inappropriate operating conditions will cause the degradation of lithium-ion batteries to increase, even causing fire and explosion. In order to gain a better understanding of the management and operation strategies, the fundamental

Table 2.1: Comparison of different types of batteries

Characteristics	Lead-acid battery	Ni-Cd battery	Ni-MH battery	Zebra battery	Lithium-ion battery
Gravimetric energy density (Wh/kg)	30 - 50	50 - 75	54 - 120	100 - 120	150 - 250
Gravimetric power density (W/kg)	75 - 300	150 - 300	200 - 1200	150 - 200	500 - 2000
Volumetric energy density (Wh/L)	50 -90	60 -150	190 - 490	150 - 180	400 - 650
Volumetric power density (W/L)	10 - 400	75 - 700	500 - 3000	220 - 300	1500 - 10,000
Nominal cell voltage (V)	2	1.2	1.2	2.58	3.3 - 3.7
Charging temperature (°C)	-20 - 50	0 - 45	0 - 45	270 - 350	0 - 45
Discharging temperature (°C)	-20 - 50	-20 - 65	-20 - 65	270 - 350	-20 - 60
Daily self-discharge (%)	0.05 - 0.3	0.2 - 0.6	1 - 2	10 - 15	0.1 -0.3
Life time (years)	5 - 15	15 - 20	15 - 20	10 - 20	8 - 15
Cycle life (cycles)	500 - 2000	1500 - 3000	1500 - 3000	> 2500	1000 - 10,000
Environmental impact	Serious	Serious	Medium	Slight	Slight

electrochemical properties of a lithium-ion battery should be studied in details. However, it is difficult to present a comprehensive coverage of lithium-ion battery properties from all different angels, therefore, a few but most important properties which may influence battery state estimation and charge/discharge strategies are investigated in this section.

2.2.1 Battery capacity

The capacity of a battery cell is generally measured in unit of Ampere-hour (Ah), which determines the maximum energy amount that a battery can extract under the specified operating conditions. For a lithium-ion battery, the capacity is generally measured via a standard capacity test which should be repeated three times to take an average value. According to the instruction in [48], the standard capacity test of a lithium-ion battery includes two phases, the charging phase and the discharging phase. The battery is charged under a Constant Current Constant Voltage (CCCV) charging profile since it starts with a constant current charging followed by a constant voltage charging. The battery cell is charged under a constant current to specific voltage level (the upper cut-off voltage) firstly, then the battery cell is charged under the constant voltage with a decreasing current to achieve a full charge, until the charging current is lower than a specific current which is called charging stop current. For the discharging phase, the battery cell is discharged under a constant current (CC) until the terminal voltage reduce to the lower cut-off voltage. The upper and lower cut-off voltages of a lithium-ion battery depend on the different chemical materials adopted in the electrodes. The charging/discharging current and stop current are determined by the nominal capacity of the battery cell, which are governed by C-rates. The capacity of the battery cell can be calculated by integrating the charge/discharge current over time.

During the discharge process, the amount of available electric charges decreases due to the continuous progress of the chemical reactions. When there is no available electric charges to support the battery to discharge, this battery is fully discharged, which means the SOC value of the battery is 0/%. Vice versa, the battery SOC equals to 100% if the battery is fully charged. However, the definition of SOC is slightly different in different publications. In this thesis, the SOC is defined as the ratio of the available capacity to the current capacity, not the rated capacity since the actual capacity of a lithium-ion battery various under different operation conditions. Charging/discharging current rate is one of the key factors which affect battery capacity. The magnitude of the current which can fully discharge a battery from 100% to 0% is by 1 hour defined as 1C current rate, if the current increases to 2C, the battery can be fully discharged by 0.5 hours. Although increasing the current rate can reduce charging/discharging time, it also reduces the capacity that can actually be charged or discharged. This phenomenon can be modelled by the Peukert's law, such as shown in Eq. (2.1).

$$C_I = It = C_r(\frac{C_r}{IH})^{k_{pe}-1} \tag{2.1}$$

where I is the actual discharge current and t is the actual time to discharge the battery. C_r represents the rated battery capacity and H represents the rated discharge time. k_{pe} is the Peukert constant which is a number greater than 1. C_I represents the battery effective capacity at the discharge rate I.

2.2.2 Battery OCV

The open circuit voltage (OCV) of a battery equals to its terminal voltage if the battery is connected with no load and the internal equilibrium is reached. Therefore, the OCV of a lithium-ion battery can be measured as the terminal voltage if the battery is rested for a long period time [49]. Battery OCV depends on several factors, SOC is one of them. Generally, the OCV value of a battery rises with the increasing of SOC. Moreover, OCV can be used to express the potential difference between the positive and negative electrodes under an internal equilibrium, thus, the OCV values (measured at the same SOC value) are different for the batteries which contain dissimilar chemical materials in the electrodes. Fig. 2.1. presents the OCV values of the LFP and NMC batteries at different SOC points. It can be seen that the OCV curve of the NMC battery is steeper and close to linear, the OCV curve of the LFP battery is more flat and nonlinear. It also should be noting that the battery relaxes to a voltage value which is higher than the OCV after charging process and it relaxes to a lower value than the OCV after discharging process. This phenomenon is more serious in LFP batteries and it can be expressed as the hysteresis effect [50]. In order to overcome this problem, Hussein et al. [51] proposed an OCV measurement approach which takes the average value of the charging and discharging voltage curve under a very low current rate (C/30).

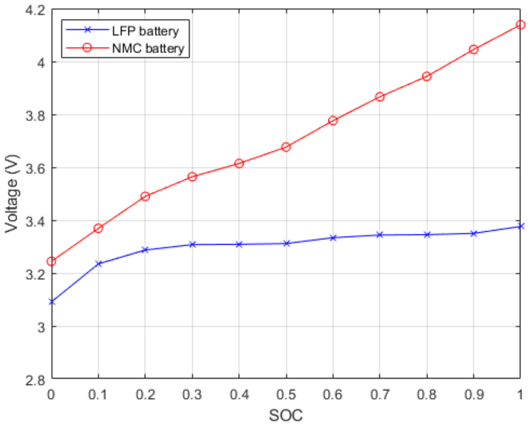

Figure 2.1: OCV vs SOC curves for typical LFP and NMC batteries

Moreover, since the SOC is defined as the ratio of the available capacity to the battery current capacity, the OCV-SOC relationship only appears a slightly difference during the ageing.

2.2.3 Effect of temperature

Temperature is a critical factor which influence the performance of a lithium-ion battery. Generally, the usable capacity increases with the rise of temperature until to a specific value and it decreases rapidly when the temperature falls below room temperature. In addition to the impacts on the usable capacity, temperature also influences battery internal resistance. According to the experiment results in [52], the battery internal resistance increases nonlinearly when the battery temperature falls below room temperature. Moreover, at the lower operating temperature, the internal resistance is more sensitive to the variation of SOC since the active particles travels slower at low temperature.

It is widely recognised that high temperature accelerates the electrolyte decomposition and also expedites the formation of SEI [53]. The side reactions inside the battery are also accelerated at high temperature, which also contributes to battery ageing. The upper limit of the operating temperature of a lithium-ion battery is usually around 50 °C to 60 °C. The battery electrolyte is more active at high temperature which also accelerates the decomposition reaction. The decomposition product is combined with the anode, which consumes cathode materials and results in cathode structure change [54]. Therefore, high operating temperature affects battery cathode significantly and causes relatively small effect on the anode. Moreover, thermal runaway may occur if the battery operates at too high temperature. The experiment results in [55] indicate that thermal runaway may occur spontaneously if the temperature of a lithium-ion battery increases to 80 °C. The thermal runaway features of a prismatic lithium-ion battery are evaluated in [56], the experiment results indicate that the melting of the separator occurs around 130 °C. In order to avoid the appearance of over-temperatures, different approaches of battery internal temperature were proposed, and many battery cooling systems were developed [57].

Unlike the high temperature effect, low temperature causes greater effect on the anode than the cathode. The rate of chemical reactions inside a lithium-ion battery is reduced at low temperatures. However, lithium plating phenomenon may occur when a lithium-ion battery operates at low temperature. Lithium plating is recognised as a major factor which causes lithium-ion batteries have higher internal resistance at low temperature [58]. During the charging process at normal temperature, lithium ions travel from the cathode to the anode and intercalate into the active materials. However, when the lithium-ion battery is charging at low temperature, the cyclable lithium are reduced to form metallic Li as a layer structure at the anode [59]. Therefore, lithium-ion batteries should be avoided from charging if the operating temperature is too low. In order to allow lithium-ion batteries to work in low temperature environments, various external [60; 61; 62] and internal (self) [63; 64; 65] pre-heating technologies for lithium ion batteries were developed.

2.2.4 Effect of ageing

The ageing effect limits the performance of a lithium-ion battery throughout its whole service life, no matter the cell is in operation or not. As ageing continues to occur, two phenomena become more apparent, the fading of capacity and the rise of impedance. The capacity fading is generally caused by the loss of cyclable lithium and active materials [66]. The loss of cyclable lithium can occur at both positive and negative electrodes due to the side reactions [67]. The loss of active materials may be caused by several factors, such as the structural change and delamination of the electrodes, material isolation and dissolution [68]. The foremost origin of impedance rise is the growth of the solid electrolyte interphase (SEI), which limits electrode electrical contact [69]. SEI is formed naturally during the first charge process in order to prevent the negative electrode from corrosion [70]. However, as the ageing process continues, the SEI film is also gradually thickened. The formation and growth of the SEI film require lithium ions which causes cathode materials consumption during the charging process [71]. The ageing process of a battery can be divided into two parts, the calendar ageing and the cycle ageing. If no charging/discharging process takes place, only calendar ageing occurs to the battery. When the battery is operating under the charging or discharging processes, both calendar and cycle ageing occur.

Calendar ageing describes the degradation which is caused during battery storage, it is highly according to the battery storage conditions [66]. During the storage, no external charging/discharging takes place, only self-discharge occurs. The condition of storage temperature is one of the main factors which affects battery calendar ageing and self-discharge rate. At high temperature, the loss of the lithium increases due to the acceleration of the growth of SEI layer and the side reactions [72]. At low temperature, these phenomena have been suppressed, but other problems arise, such as loss of material diffusion, lithium plating and chemicals structural change [73].

The SOC level during storage is another factor which influences calendar ageing. SOC represents the proportion of ions and charges at the electrodes, which also implies the potential disequilibrium at the electrode and the electrolyte [66]. Therefore, under the same storage temperature, high storage SOC presents a higher battery degradation [74]. Comparing with the effect of high storage temperature, high storage SOC presents restrictive impact [75]. Furthermore, the effect of calendar ageing on the battery becomes severe as the storage time increases. According to the test results in [76], the capacity loss and resistance increase of a lithium-ion battery under calendar ageing are nonlinear with the storage time, which presents a tendency to square root kind of the storage time. However, the experiment results in [74] indicate that calendar ageing has a linear relationship with the storage time, and only a slight trend of correlation with the square root of storage time can be observed.

Cycle ageing only occurs when the battery operates in the charging or discharging process. All the factors which influence calendar ageing must be considered in cycle ageing since calendar ageing appears whether the battery in operating or not [66]. In addition to the factors mentioned in calendar ageing, depth of discharge (DOD) is another factor that affects battery cycling ageing. According to the test results in [77], batteries which cycled under larger DOD present more severe degradation performance. Moreover, the study presented in [74] indicates that the batteries cycled around higher or lower SOC levels tend to degrade faster than the ones cycled around middle SOC range. Charging/discharging current rate also has significant impacts on the battery cycle ageing. High current rate accelerates ageing phenomenon in terms of capacity fading and resistance rise. The experiment results in [78] show that after 300 cycles, the results of capacity fade of the cells that were cycled under 1C, 2C and 3C discharge current are 9.5%, 13.2% and 16.9% respectively.

2.3 Battery models

As discussed in Chapter 1, various battery models have been developed with different levels of accuracy and complexity. According to the presence of physical explanation of the electrochemical process of the battery, these models can be mainly divided into three groups: white-box models, grey-box models and black-box models. In this section, some commonly used battery models for lithium-ion batteries are reviewed and compared.

2.3.1 Electrochemical models

The electrochemical model is a typical white-box battery model that uses the mechanisms of electrochemical processes to describe the electrical behaviour of the battery [79]. The single-particle model (SPM) is the most popular simplified electrochemical model which utilizes a single particle to represent the concentration distribution of lithium-ion in the electrode. Therefore, the SPM can be used to describe the diffusion of solid-phase of the electrodes [80]. However, the electrolyte dynamics are neglected in the conventional SPM. Therefore, various improved SPMs have been developed with the consideration of the electrolyte dynamic effects [81; 82; 83].

The pseudo-two-dimensional (P2D) model [84] is another popular electrochemical model which regards the battery anode and cathode as being composed of numerous spherical particles surrounded by electrolyte. The intercalation and deintercalation processes of lithium-ions are modelled based on the porous electrode theory and the charge transfer process in the electrolyte is modelled according to the concentrated solution theory. The P2D model can comprehensively examine the main and side reactions inside the battery by several coupled partial differential equations (PEDs). Based on the P2D model, some coupled battery models have been developed to describe different features of battery, such as the electro-chemo-mechanical coupled model [85], electrochemical-thermal-capacity fade coupled model [86], and electrochemical-thermal-mechanical degradation model [87], etc.

Electrochemical models are accurate in describing battery dynamic voltage response since the electrochemical processes occurring inside the battery can be clearly represented. However, the electrochemical models are difficult to use for real-time simulation since many model parameters are involved in electrochemical models. Determining these parameters not only takes a lot of time but also requires an in-depth understanding of the battery structure and properties. Moreover, complex numerical techniques are required to solve the PDEs in the the electrochemical models, which makes the electrochemical models are unsuitable for real-time simulation due to the high computational cost. Therefore, electrochemical models are often used to analyse the internal electrochemical processes of the battery and develop other simplified models.

2.3.2 ECMs

ECMs describe battery dynamic voltage behaviour by using electric elements, such as voltage source, resistors and capacitors, etc. The Rint model is the simplest ECM which presents the voltage behaviour of a battery with only two electrical components, an ideal voltage to present OCV and a resistor to present the ohmic resistance of a battery [2]. The schematic diagram of a Rint model is presented in Fig. 2.2. The terminal voltage in the Rint model can be represented as:

$$V_t = V_{OC} + IR \tag{2.2}$$

where V_t represents the battery terminal voltage, V_{oc} represents the OCV, R represents the battery ohmic resistance, I is the current through the battery.

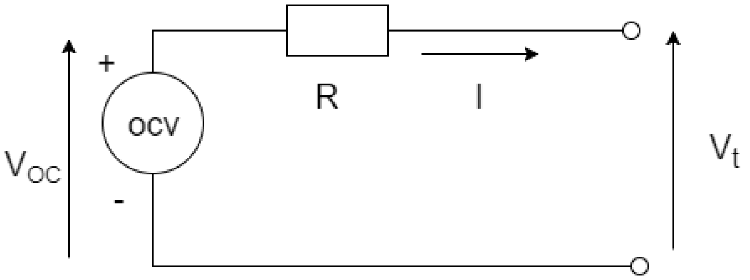

Figure 2.2: Rint Model [2]

Although the Rint model is simple and easy to implement, it has limited ability to express battery dynamic behaviour for a long operation time due to the lack of polarisation voltage expression. Therefore, RC network based models have been proposed to overcome the drawback of Rint model.

Among the ECMs, RC network models are highly acclaimed. The structure of a RC network ECM contains an OCV voltage source, a resistor, one or more RC parallel networks connected in series with the resistor. The RC network models are usually defined as the n^{th} order RC ECMs depending on the number n of RC networks utilised in the circuit. Generally, the selection of model order is a trade-off between the model accuracy and complexity [88]. The first and second order RC network ECMs are more popular than the ones with a higher order [89].

The first-order RC network is also known as Thevenin model, which contains a voltage source to represent the OCV, a resistor R_0 to represent battery internal ohmic resistance, a RC parallel network to represent the polarisation behaviours. The resistor R_p in the RC parallel network stands for the polarisation resistance, the capacitor C_p is used to represent the transient response during charging and discharging. A schematic diagram of the first-order RC network ECM is presented in Fig. 2.3. The discretised voltage equations of the first-order RC model can be expressed as:

$$\begin{cases} V_{p,k+1} = e^{\frac{-\Delta t}{\tau_p}} V_{p,k} + (1 - e^{\frac{-\Delta t}{\tau_p}}) I_k R_p \\ V_{t,k} = V_{OC,k} + I_k R_0 + V_{p,k} \end{cases} \tag{2.3}$$

where k represents the kth sample time, Δt represents the sampling period, τ_p is the time constant of the RC network, $\tau_p = R_p \ C_p$.

2.3.3 Empirical models

Empirical models describe the battery dynamic features by using empirical equations. Unlike the equivalent circuit models, empirical models usually do not require to take any specific tests, e.g. the OCV test and HPPC test, etc. Shepherd model

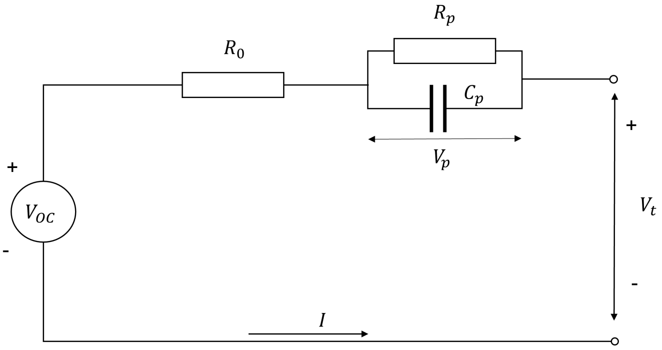

Figure 2.3: First-order RC network model

[90], Unnewehr model [91] and Nernst model [92] are the most popular empirical models for lithium-ion batteries, the mathematical equations of these three empirical models are expressed as:

- Shepherd's model

$$V_t = k_0 + R_0 I + k_1/SOC \tag{2.4}$$

- Unnewehr Universal Model

$$V_t = k_0 + R_0 I + k_2 SOC \tag{2.5}$$

- Nernst Model

$$V_t = k_0 + R_0 I + k_3 ln(SOC) + k_4 ln(1 - SOC) \tag{2.6}$$

where V_t represents the battery terminal voltage, I represents the current, R_0 represents the battery internal resistance, K_0, K_1, K_2, K_3 and K_4 are constant coefficients to fit the model. The shepherd model, Unnewehr model and Nernst model can also be combined in order to achieve more accurate performance [93; 94; 95], the mathematical equation of the combined model can be expressed as:

$$V_t = k_0 + R_0 I + k_1 SOC + k_2/SOC + k_3 ln(SOC) + k_4 ln(1 - SOC) \tag{2.7}$$

Although the empirical models are simple and easy to implement, their accuracy and reliability are generally low. Moreover, empirical models are usually only suitable for some specific applications, such as the applications with constant current and constant temperature conditions.

2.3.4 Black-box models

Black-box models describe the battery dynamic behaviour by using intelligent algorithms without priori knowledge about the underlying electrochemical processes occurring inside the battery.

Neural network (NN) model is one of the most popular Black-box models, which emulates the working process of human brain neurons. In [96], a back-propagation neural network (BPNN) based battery model is developed to capture the voltage response of step discharge current of a lithium-ion battery. The output of this BPNN model is the battery terminal voltage and the model inputs are the battery current, temperature, SOC and the measured voltages of the previous five samples. In [97], a long-short time memory (LSTM) based recurrent neural network (RNN) model is developed to describe the long-term nonlinear relationship between the battery states and the measurable signals. Particle filter method is then applied to estimate the battery SOC. In [98], a (RBF) kernel based support vector machine (SVM) battery model is established to describe the battery dynamic voltage response. The model inputs include battery current, temperature and SOC, the model output is the battery terminal voltage. The model can achieve accurate simulating results with small amounts of experimental data. Moreover, an improved

RBF based battery model is proposed in [99] to capture the dynamic voltage response of a lithium-ion battery. In this model, the Levenberg-Marquardt algorithm is employed to tune the model parameters and a subset selection method, namely fast recursive algorithm (FRA) [100] is applied to select the model inputs.

2.4 Battery SOC estimation

As a crucial function of the BMS, the estimation of battery SOC should be accurate and reliable to ensure the battery can operate safely and efficiently. Various battery SOC estimation have been proposed in the literature with different levels of accuracy and complexity. Generally, the battery SOC estimation methods can be divided into two groups, the model-free methods and the model-based methods.

2.4.1 Model-free methods

Coulombic counting method, which is also as know as Ampere-hour (Ah) method, is one of the most commonly used model-free methods in battery SOC estimation. It integrates the charging or discharging current to calculate the remaining charge in the battery. The expression of Ah method in SOC estimation is given as follows:

$$SOC_{t_k} = SOC_{t_0} + \frac{1}{C_n}\int_{t_0}^{t_k} (\eta \times I_t - S_d)dt \tag{2.8}$$

where SOC_{t_0} is the initial battery SOC, C_n represents the battery capacity, I_t is the load current at time t (positive sign for charging and negative sign for discharging). η and S_d represent the battery coulombic efficiency and self-discharging rate, respectively. η and S_d may vary depending on the type of battery and the working condition. Lithium-ion batteries generally have very high coulombic efficiency and very low self-discharging rate, it is widely assumed that $\eta = 1$ and $S_d = 0$ for lithium-ion batteries.

Coulombic counting method is simple and straightforward to apply for battery SOC estimation, it is widely utilised in various applications. However, as an open-loop method, coulombic counting method is vulnerable to the error of current measurement since the current measurement error is accumulated during the charging/discharging processes. Moreover, the initial battery SOC value needs to be determined accurately, otherwise there will be a bias in the SOC estimation. Therefore, the coulombic counting method needs to be calibrated periodically to ensure the accuracy and reliability.

The OCV-based method is another common used model-free method for battery SOC estimation. The OCV-based method estimates battery SOC relies upon the one-to-one relationship between the battery OCV and SOC. However, battery OCV is also difficult to determine, it may take a very lone time (several hours) for the battery terminal voltage to stabilise. Moreover, some lithium-ion batteries, such as the lithium iron phosphate batteries generally have a very flat OCV-SOC curve. Therefore, in the flat OCV-SOC curve region, a small OCV measurement error may cause a large error in SOC estimation.

Some other model-free methods, such as battery impedance-based methods [101; 102] and magnetism methods [103] are also proposed for battery SOC estimation. However, these methods generally require specific equipment, which is difficult to be widely used.

2.4.2 Model-based methods

The core idea of model-based battery SOC estimation method is to establish the relationship between the measurable battery signals (such as current, voltage and temperature, etc) with the battery SOC. There are various model-based methods that utilise different types of battery models for SOC estimation, such as the methods using electrochemical models [104; 105], ECMs [106; 107; 108], black-box models [109; 110], etc. Some model-based methods estimate battery SOC with the utilisation of filters or observers. In this way, the battery model needs to be formulated into standard state-space equations and different state estimation methods then can be applied for real time SOC estimation, such as the KF method [111], EKF method [112; 113], UKF method [114; 115], sliding mode observer [116] and H-infinity methods [107], etc.

Since battery SOC usually needs to be estimated in real-time, some simplified electrochemical models (such as SPMs and order-reduced SPMs) are more suitable for real-time battery SOC estimation. An order-reduced SPM based SOC estimation method combined with EKF algorithm (namely SPM-EKF method) is proposed in [104]. The order-reduced SPM regards the lithium-ion concentration in the positive electrode as an algebraic function of the lithium-ion concentration in the negative electrode, the finite central-difference method is then applied to discretize the order-reduced SPM. Finally, the EKF algorithm is utilised for SOC estimation. In [105], an improved SPM based SOC and capacity estimation strategy is proposed. The SPM is first improved by incorporating the lithium-ion concentration distribution in the electrolyte phase, and two EKFs with different time scales are applied to estimate the battery SOC and capacity.

ECMs are the most widely used battery models for real-time SOC estimation due to their advantages in model accuracy and simplicity. In [106], an online battery SOC estimator is developed based on the Thevenin model. An EKF is utilised to identify the parameters in the Thevenin model online and an UKF is applied to estimate the battery SOC in real-time. In [107], a multi-model based SOC estimation approach is proposed. The Thevenin model, DP model and 3rd-order RC model are employed to estimate battery SOC respectively using the H-infinity algorithm. Bayes theorem-based method is then applied to determine the optimal wights of these three models. Finally, the optimal SOC is achieved as a fusion of the estimated SOCs from the three models with the corresponding weights.

The black-box models, such as NN-based models have been widely utilised in battery SOC. In [109], an RBF-NN-based battery model is developed for battery SOC estimation with the combination of Ah method. The RBF-NN-based battery model is employed to predict the battery terminal voltage and the EKF is utilised to estimate battery SOC. In [110], an optimal BPNN based SOC estimation method is developed. Principal component analysis (PCA) is employed to select the most significant input features for the BPNN model and particle swarm optimisation (PSO) algorithm is applied to determine the model structure.

2.5 Battery SOH estimation

SOH is a figure of merit of the condition of a battery compared to its ideal conditions. An accurate SOH estimation not only helps to develop suitable management and operation procedures prolong the battery service life but also contributes to failure avoidance and optimising the schedules of battery maintenance. Even though given the importance of SOH, there still does not exist a consensus on how SOH should be determined since it does not correspond to a particular physical quality. The parameters that can be used to determine battery SOH include capacity, internal resistance, self-discharge rate, ability to accept a charge, and the total amount of energy-charged/discharged, etc. In some applications, such as EVs, the cyclability and deliverability of the battery need to be prioritised because battery capacity reflects how much energy can be stored into a fully charged battery. Thus, the remaining capacity of the battery is usually used to determine SOH. The calculation of SOH is generally defined as the ratio between the maximum available capacity of the battery and its nominal capacity [117], as shown in

Eq. (2.9).

$$SOH = \frac{C_n}{C_0} \times 100\% \tag{2.9}$$

where C_n is the maximum available capacity in present condition, C_0 is the rated capacity of the battery. When C_0 is given, the battery SOH can be determined by the estimation of C_n. Therefore, the battery capacity estimation techniques can be utilised for battery SOH estimation. Various battery capacity estimation methods have been developed in the literature, and they can be typically divided into two categories: direct methods and indirect methods.

2.5.1 Direct method

As the easiest and most precise method for SOH estimation, the battery SOH can be determined directly if the battery present capacity can be accurately measured. Coulomb counting method is generally used to calculate the battery present capacity via counting the charge transferred through the battery during the full charging or discharging process. Direct capacity measurement can theoretically provide very high accuracy by using high-precision measurement techniques. Therefore, this method is usually utilised for capacity calibration in laboratory environments. However, this method is not suitable for EV applications because it is difficult to stop and measure the fully charged capacity for a running EV. Moreover, the accuracy of remaining capacity measurement highly depends on the precision of the current sensor, the errors in the current measurement will be accumulated until the end of the entire process.

2.5.2 Indirect methods

The indirect SOH estimation methods can be roughly divided into two categories: the SOC-based methods and the SOC-free methods. The SOC-based method estimates the battery capacity or internal resistance by the SOC information of a battery, thereby determining the battery SOH. For example, the battery present available capacity can be calculated based on the SOC information via Coulomb counting method, as follows

$$C_a = \int_{t_1}^{t_2} \frac{\eta I(t)}{3600} dt / (z(t_2) - z(t_1)) \tag{2.10}$$

where η is the columbic efficiency, which is generally assumed to be 1 in lithium-ion batteries due to the relatively low rate of side reactions. I represents the measured current in ampere. $z(t_1)$ and $z(t_2)$ represent the battery SOC value at time t_1 and t_2 respectively.

The capacity can also be regarded as an internal state of a battery, and the equivalent circuit model and adaptive filter can be utilised for joint estimation of SOC and capacity [40; 118; 119; 120]. However, accurate SOC estimation is also difficult to obtain in practical applications. Furthermore, inaccurate SOC estimation will greatly affect on the estimation of SOH, and even cause the filter to fail to converge [121]. In addition to the SOC-based method, various SOC-free SOH estimation methods have been developed according to the analysis of entire degradation data of batteries. Battery SOH can be determined by obtaining the relationship between the health indicators and battery capacity.

2.5.2.1 Capacity regression model based methods

The number of cycles of a battery can be observed as a health indicator to form a simple way to estimate battery SOH. The core idea of cycle number based capacity regression model is to find the relationship between the SOH of a battery and the number of cycles has experienced. Polynomial, exponential and power law are usually used as fitting models. In [122], a second-order polynomial regression model of maximum available capacity of a battery is developed. Cycle number is the only variable in this model, and the model is expressed as follows

$$C_n = an^2 + bn + c \tag{2.11}$$

where C_n represents the maximum available capacity of a battery at cycle n, n represents the number of cycles. a, b and c are the model parameters which can be identified by least squares approach. A similar second-order polynomial regression model for SOH estimation can be found in [123], and again the cycle number is the only variable in this model. Since the main ageing mechanism of a lithium-ion battery is the loss of lithium ion inventory, the capacity loss is thus can be considered to follow a power law relation with the cycle number. Therefore, Arrhenius law can be used to model the relationship between the relative capacity loss and cycle number [72; 124; 125], the mathematical expression of the relative capacity loss can be described as

$$\xi = A * e^{-\frac{E_a}{RT}} * n^z \tag{2.12}$$

where ξ represents the relative capacity loss of a battery with unit of %, E_a represents the activation energy with unit of J/mol, R is the gas constant with the unit of J/K/mol, T represents temperature with unit of K. n is the cycle number and z is the power law factor. When the temperature is given, the parameters A, E_a/R and z could be directly obtained by curve fitting. Once the parameters have been identified, the battery SOH can be calculated as

$$SOH = 1 - A * e^{-\frac{E_a}{RT}} * n^z \tag{2.13}$$

The cycle number based methods are simple and easy to implement, but they all face two severe challenges: one is that the cycle number information of the batteries employed on EVs could have a large error or even unknown in some cases, which causes this method to fail. The other challenge is that this cycle number based method primarily estimates the SOH by recording the number of complete charges and discharges. In some applications, full charged/discharged cycles are rare in normal operations. Although conversion coefficients can be used to covert the incomplete cycles into full charged/discharged cycles, additional experimental tests are required to determine the conversion coefficients. Moreover, the conversion accuracy between the cycles of different depths of discharge is difficult to guarantee.

It is widely recognised that battery ageing is a slow and irreversible process, and the cyclability and deliverability of a battery will gradually degrade with use. Therefore, the maximum available capacity of a battery can be modelled into a recursive form. In [126], the battery charge capacity of the kth cycle is modelled as follows

$$C_n = \eta C_{n-1} + \beta_1 e^{\frac{\beta_2}{\Delta t_k}} \tag{2.14}$$

where C_n and C_{n-1} represent the charge capacity of the nth and the (n-1)th cycle respectively. Δt_k is the rest period between the nth and (n+1)th cycle. β_1 and β_2 are model parameters can be determined by curve fitting approach.

According to the cycle number based model shown in Eq. (2.12), a recursive model of the relative capacity loss is developed in [124]. The relative capacity loss recursive model is expressed in Eq. (2.15).

$$\xi_{n_p} = \xi_{n_{p-1}} + (n_p - n_{p-1})k_1 e^{\frac{k2}{T}} \xi_{n_{p-1}}^{k3} \tag{2.15}$$

where ξ_{n_p} represents the relative capacity loss of a battery after n_p times cycle. k_1, k_2 and k_3 are the constants to be determined.

Generally, if the capacity calibration can be performed regularly, the capacity recursive based regression models can achieve accurate SOH estimation results. However, capacity calibration usually requires at least one complete charging-discharging cycles. It is difficult to perform frequent capacity calibration for EV applications due to the cost of time and energy. If the capacity calibration cannot be performed in time, as an open-loop method, the capacity regression models may face failure once a large error exists, and the errors will continue to accumulate.

2.5.2.2 Charging curve analysis based methods

Since Constant-Current-Constant-Voltage (CCCV) method is one of the most common charging methods for lithium-ion batteries [127; 128; 129], a series of approaches based on the charging curves of voltage or current have been developed in the literature. It is well known that the battery internal information is difficult to be obtained from the voltage curve directly. To tackle this challenge, cyclic voltammogram method is widely used to analyze battery capacity degradation. Incremental capacity analysis (ICA) is one of the most popular cyclic voltammogram methods that are used in lithium-ion batteries. ICA is a powerful electrochemical characterisation technique which processes the voltage data in the constant current (CC) phase to generate IC curves. The IC curves can be calculated by integrating capacity corresponding to small voltage intervals (dQ/dV) through the charging process.

$$\frac{dQ}{dV} = \frac{\Delta Q}{\Delta V} = \frac{Q_t - Q_{t-1}}{V_t - V_{t-1}} \tag{2.16}$$

where Q_t and V_t represent the battery capacity and terminal voltage at time t. The voltage plateaus can therefore be converted into recognisable IC peaks. These IC peaks can be used to determine battery SOH due to their unique shapes, amplitudes and positions at different battery ageing states [130]. The approaches that adopt the position values of the IC peaks for battery SOH evaluation can be found in [131; 132; 133].

It is worth noting that the formation of ICA curve is very sensitive to the measurement of voltage [134]. In order to obtain smooth ICA results and accurate IC peak positions, the pre-processing of the voltage data is necessary. The common voltage pre-processing techniques include moving average filter, median filter and Gaussian filter, etc. Moreover, ICA approach generally requires a very low current rate test condition (e.g. 25/C). In practical EV applications, it is difficult to capture such a small current accurately. In addition, the dV calculation in ICA approach may encounter problems due to the voltage plateaus.

To tackle above challenges, the partial charging capacity based on the local interval between two IC peaks are utilised for SOH estimation [135; 136; 137; 138]. In [135], a probability density function (PDF) based method is proposed to replace the conventional IC curves. As a derivative of the ICA approach, the PDF based method can effectively solve the problems encountered in dV calculation.

In addition to using the voltage curve in the constant current (CC) charging phase (i.e. ICA and PDF based method), the current curve in the constant voltage (CV) phase can also be utilised for determining battery SOH. As the health status declines, the battery capacity will gradually decrease, resulting in a time change in the CC phase and the CV phase under the same CCCV charging profile. In general, the aged battery takes shorter time in the CC charging phase while longer time in the CV charging phase. In the CV phase, the current decreases to the cut-off value with a unique curve shape at different ageing states. Therefore, the current charging curve in the CV phase can be used to determine the battery SOH. In [139], the current behaviour during the CV phase is modelled as

$$I(t) = A(C_L)e^{-B(C_L)t} + C(C_L) \tag{2.17}$$

where $I(t)$ represents the current at time t, C_L represents the capacity loss, A, B and C are the model parameters which had corresponding relationships with the capacity loss.

Similar to ICA and PDF approaches, the CV charging curve method does not require the historical data of the battery (such as the cycle number and previous capacity), and the SOH estimation can be performed only based on the current data of the present cycle. The CV charging curve method has two main drawbacks. One is that it requires specific working condition - CV charging condition. For the applications of EV charging, the CV charging mode usually exists in the final stage of the conventional charging mode (CCCV charging), but it is rare in fast charging mode. Another drawback is that there is no significant change in the current curve in the CV phase at certain SOH levels, which leads to a lower SOH estimation accuracy.

2.6 FBG sensing in BMS

Due to the shortcomings of the electrical sensors, such as being easily interfered by electromagnetic fields in harsh working conditions and difficult to be multiplexed, etc, the utilisation of optical fiber sensing technologies have received a lot of attention in recent years. As one of the most popular optical fiber sensing approaches, FBG sensing technique has also been applied in BMS.

2.6.1 FBG working principle

A FBG is made by exposing the core of a fiber to a periodic pattern of laser light with defined energy. The refractive index of the fiber core is increased by the exposure and a fixed index modulation (a grating) can be created according to the exposure pattern. At each position where the refraction changes, a small amount of the light will be reflected. All the reflected lights can be combined coherently to one large reflection at a particular wavelength. The wavelength where the maximum reflection occurs is defined as the Bragg wavelength (λ_B), which can be calculated as:

$$\lambda_B = 2 * n_{eff} * \Lambda \tag{2.18}$$

where n_{eff} is the effective refractive index and Λ is the grating period.

The changes in temperature and strain can lead to the variations in both of the effective refractive index and the grating period. A change in temperature affects n_{eff} due to the thermo-optic effect and it also causes the variation in Λ due to the thermal expansion effect. A change in strain causes a variation in n_{eff} due to the stress-optic effect and also leads to a displacement of Λ. Therefore, the changes in temperature and strain can be determined by the measurement of λ_B if appropriate temperature-strain decoupling methods are applied.

2.6.2 FBG applications in BMS

According to the working principle of FBGs, FBG sensing technologies are mainly applied to measure the internal and external signals of the battery, such as temperature and strain.

For temperature monitoring, FBG sensors can be attached to the surface or electrodes of a battery to monitor the battery external temperature [140; 141; 142]. In [140], FBG sensors are attached to the surface of a smartphone battery to monitor the surface temperature variations at different locations of the battery. The temperature monitoring results obtained by the FBG sensors are compared with the ones obtained by K-type thermocouples under different operating conditions. The results show that FBG sensors can achieve better performance in terms of resolution and response time. A FBG-based temperature sensor is proposed in [141] to monitor the temperatures of battery external electrodes. This sensor consists a metal (aluminium alloy) ring and a bare FBG (attached to the inner groove of the metal ring), which can be gloved on the external electrodes of the cell. In [142], a thermal sensing network which contains 37 FBG sensors is proposed to monitor the temperature distribution of a battery pack consisting of three prismatic batteries. The FBG sensors are attached on the pre-designed locations of the battery surface (top, middle and bottom zones) in order to identify the zones where hot-spots are more likely to occur. In addition to measuring the external temperature, FBG sensors can also be embedded inside the cell to measure the internal temperature [143; 144]. In [143], FBG sensors are placed both inside and outside the cell to monitor the internal and external temperature variations of the cell, the results show that the measured internal and external temperatures have the same changing trend. In [144], a fiber with four FBG sensors is embedded inside a cylindrical lithium-ion battery to determine the axial temperature gradient inside the cell. The proposed sensor system is threaded through a bespoke aluminium tube in order to eliminate the strain effect.

For strain monitoring, the FBG sensors can be either attached to the surface of the cell for surface strain measurement [145; 146], or embedded inside the cell for internal strain measurement [147; 148; 149]. In [145], a FBG-based strain sensor is attached to the surface of a pouch cell to determine the battery volume change during the operations. The proposed strain sensor comprises two FBGs, namely the bonded FBG and the reference FBG. The bonded FBG is utilised to respond to both strain and temperature changes, its two ends are bonded at the cell surface with epoxy glue. The reference FBG operates as a thermal compensation sensor which is sensitive only to temperature changes, it is loosely attached to the cell surface. An enhanced sensitivity FBG-based strain sensor is proposed in [146] to monitor battery surface strain variation. The proposed sensor consists of two FBGs (the bonded FBG and the reference FBG) and a sensitivity-enhanced structure. Compared to the bare FBG sensor, this proposed sensitivity-enhanced strain sensor can achieve much better strain response. In [147], two FBG-based strain sensor are embedded into a pouch cell. One FBG is attached to the battery anode and the other FBG is implanted in the anode. Reproducible peak shifting can be observed in both FBGs at different SOC levels. The results show that the implanted FBG is more sensitive than the attached FBG due to the influence of transverse strain.

Based on the measurement of strain and temperature, FBG sensors are also utilised in battery states estimation. In [149], the FBG sensors are embedded inside the battery to monitor the strain variations of the electrode during charging and discharging process. Extended Kalman filter (EKF) is implemented for SOC estimation based on an empirically developed strain prediction model. A machine learning based SOC estimation approach is reported in [150]. The strain data were obtained from a FBG based sensor network which is mounted on the surface of the batteries. The dynamic time warping (DTW) approach is employed to determine the ‘distance’ between the measured strain curve and the reference strain curve. K-nearest neighbours (KNN) algorithm is then applied as a classifier to estimate the battery SOC.

2.7 Chapter summary

A literature survey on battery modelling, states estimation and monitoring with FBG sensing technique is presented in this chapter. A comprehensive comparison of different types of batteries is firstly made. The key properties of lithium-ion batteries, such as capacity, OCV, temperature effect and ageing effect are then introduced. A good understanding of these properties is the foundation for the development of advanced state estimation techniques for BMS.

Different types of battery models, such as electrochemical models, ECMs, empirical models and black-box based models are reviewed. The pros and cons of these models are analysed in terms of accuracy and complexity. It is concluded that electrochemical models generally have accurate performance and high computational complexity, which are not suitable for real-time applications that have limited computational capabilities. Empirical models are simple and easy to implement, however they usually have limited accuracy and are only suitable for some specific applications, such as constant current and constant temperature operating conditions. ECMs and black-box based models have a good balance between accuracy and complexity, different model configurations can be selected according to the application requirement in terms of accuracy and complexity.

The review of battery states estimation methods is focused on the estimation of battery SOC and SOH, which are the two most important battery states that can affect the battery performance. The methods of battery SOC estimation can be summarised as two groups, model-free methods and model-based methods. The model-free methods are generally straightforward and easy to implement. However, they suffer from the problems such as error accumulation (Ah method) and time-consuming (OCV-based method). In model-based SOC estimation methods, battery models are usually used in a close-loop with the applications of filters or observers. Therefore, the model-based SOC estimations methods generally are more robust. The estimation of battery SOH can be mainly summarised as direct methods and indirect methods. The direct SOH estimation methods are accurate but they are difficult to implement in real BMS. Indirect methods analyse the measured signals of a battery, such as voltage, current and temperature to determine the battery SOH. However, the analysis results are greatly influenced by the measurement error. Therefore, a close-loop method may be helpful for SOH estimation.

Finally, the working principle of FBG sensors is introduced and their applications in BMS are reviewed. The applications of FBG sensing technology in BMS applications mainly focuses on the monitoring of battery temperature and strain variations. It also has great potential in the applications such as battery state estimation, fault diagnosis, and early warning, etc.

Chapter 3

Battery modelling

The battery model plays a critical role in battery performance simulation and states estimation for the model-based battery management system (BMS). Different types of battery models have been developed to describe the dynamic voltage behaviours of lithium-ion batteries. Among them, the most commonly used models are electrochemical models, black-box models, and equivalent circuit models (ECMs). Electrochemical models utilise the mechanisms of the electrochemical process to describe the electrical behaviours of the battery. Electrochemical models are accurate in describing the battery dynamic response since the electrochemical process occurring inside the battery can be clearly represented. However, the electrochemical models are difficult to use for real-time simulation since many model parameters are involved. Determining these parameters not only takes a lot of time but also requires an in-depth understanding of the battery structure and properties. Moreover, complex numerical techniques are required to solve the partial differential equations in the electrochemical models, which makes the electrochemical models are unsuitable for real-time simulation due to the high computational cost. Black-box models describe the battery dynamic behaviour by using intelligent algorithms without prior knowledge about the underlying electrochemical processes occurring inside the battery. However, the accuracy and reliability of the black-box battery models are highly influenced by the quantity and quality of the input variables. An accurate and reliable black-box battery model generally requires a large amount of offline battery tests data. Battery ECMs are highly acclaimed due to the advantages of accuracy, low complexity and ease of implementation. The parameters in battery ECMs have specific physical meanings and are easy to identify. Therefore, the equivalent circuit model is widely used in practical engineering. The existing studies related to battery ECMs modelling mainly focus on the model constructions, and different model constructions have been developed in recent years. In addition to the selection of model construction, the influence of temperature on the model accuracy is seldom mentioned in the literature. The parameters inside an ECM, such as the battery capacity, open circuit voltage (OCV), internal resistance and time constant could significantly change at different temperatures. Therefore, the temperature compensation is necessary to be considered to ensure that the battery ECM can operate accurately and reliably under different temperature environments. Some temperature-compensated ECMs have been developed accordingly in the literature.

The key idea of the temperature-compensated model is to consider the influence of temperature on the model parameters. In [151], a temperature-compensated Rint model was developed. The effects of temperature on the OCV and internal resistance are considered, but the influence of temperature on the polarisation effect cannot be reflected due to the limitation of the model construction. In [152], a temperature-compensated Thevenin model was established for battery SOC estimation with the incorporation of an extended Kalman filter (EKF). The temperature range considered in this model is 37 °C to 40 °C, which is suitable for the applications of implantable medical devices but not for other applications, such as EVs and utility energy storage. A wider temperature range (0 °C to 40 °C) temperature-compensated Thevenin model was further investigated in [153], and an unscented Kalman filter (UKF) is used for SOC estimation. However, Thevenin model cannot capture the battery polarisation effect accurately. In order to deal with the shortcomings of the above models, a DP model with temperature is developed in this chapter. Compared with the Rint model and the Thevenin model, the DP model can accurately capture the battery polarisation effects.

3.1 The DP model with temperature-compensation

A variety of battery ECMs, including the Rint model, the RC model, the Thevenin model, the dual polarisation (DP) model and the partnership for a new generation of vehicle (PNGV) model have been summarised and compared in [154], and it reveals that the DP model has an optimal performance among the examined ECMs. The DP model is also known as the second-order RC model, which is performed by adding an extra RC parallel network to the Thevenin model, as shown in Fig. 3.1. As an improved Thevenin model, the DP model simulates the polarisation effects as the concentration polarisation and the electrochemical polarisation separately [154]. The electrical behaviour of the DP model can be expressed as:

$$\begin{cases} \dot{V_1} = -\dfrac{V_1}{R_1C_1} + \dfrac{I}{C_1} \\ \dot{V_2} = -\dfrac{V_2}{R_2C_2} + \dfrac{I}{C_2} \\ V_t = V_{OC} + I * R_0 + V_1 + V_2 \end{cases} \tag{3.1}$$

where V_{oc} and V_t represents the battery OCV and terminal voltage, respectively. I is the current passing through the battery. R_0 represents the ohmic resistance, R_1 and C_1 represent the effective resistance and capacitance in the electrochem-

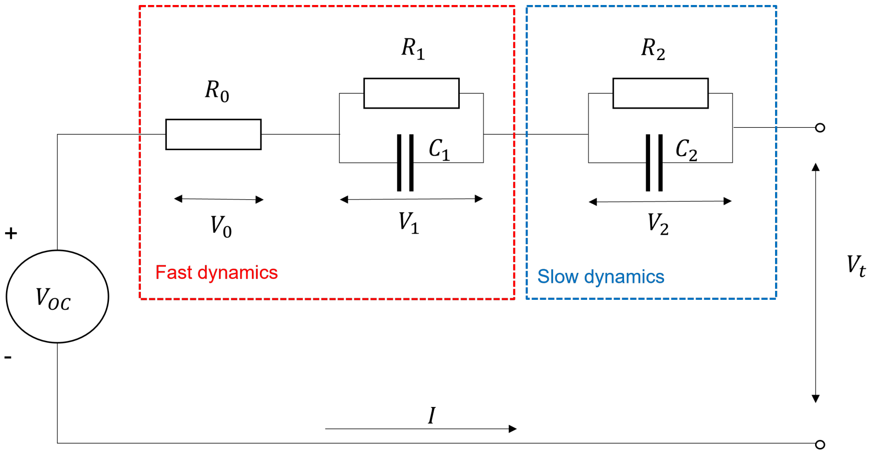

Figure 3.1: Schematic diagram for the DP model

ical polarisation, respectively. R_2 and C_2 represent the effective resistance and capacitance in the concentration polarisation, respectively. V_1 and V_2 represent the voltage across C_1 and C_2, respectively.

The discrete-time expression of the DP model can be expressed as:

$$\begin{cases} V_{1,k} = e^{\frac{-\Delta t}{\tau_1}} V_{1,k-1} + (1 - e^{\frac{-\Delta t}{\tau_1}}) I_{k-1} R_1 \\ V_{2,k} = e^{\frac{-\Delta t}{\tau_2}} V_{2,k-1} + (1 - e^{\frac{-\Delta t}{\tau_2}}) I_{k-1} R_2 \\ V_{t,k} = V_{oc} + I_k R_0 + V_{1,K} + U_{2,K} \end{cases} \tag{3.2}$$

where Δt represents the sampling time. $\tau_1 = R_1 C_1$ is the time constant of the first RC network, $\tau_2 = R_2 C_2$ is the time constant of the second RC network. It should be noted that the parameters, such as V_{OC}, R_0, R_1, R_2, τ_1 and τ_2 are dependent on both of battery SOC and temperature, and these parameters need to be identified via a series of designed tests.

3.2 Experiment setup

In order to comprehensively investigate the dependence of the DP model parameters on battery operating temperature, a series of tests, including the capacity tests, Hybrid Pulse Power Characterisation (HPPC) tests were performed at different temperature levels to identify the model parameters. To verify the accuracy and reliability of the developed model, Dynamic Stress Tests (DSTs) were performed at different temperatures for model validation.

3.2.1 Battery test bench

The battery employed in this study is a commercial NCR-18650 lithium-ion battery, which is commonly used in mobile devices and EVs. The specification of the tested battery is given in Table 3.1. A NEWARE BTS-4000 battery tester was employed to control the current and voltage during the tests and acquire the battery data such as terminal voltage, current and temperature. The sampling frequency was set to 1 Hz for all the tests performed in this study. In order to maintain and adjust the ambient temperature, all the tests in this study were performed inside a BINDER thermal chamber. The host computer with the installed software BTS-7.5 was used to program the test procedure and store the test data. The architecture of the battery test system is shown in Fig. 3.2.

Table 3.1: Specification of the tested battery

Rated Capacity	Nominal voltage	Upper cut-off voltage	Lower cut-off voltage
3.2 Ah	3.6V	4.2V	2.5V

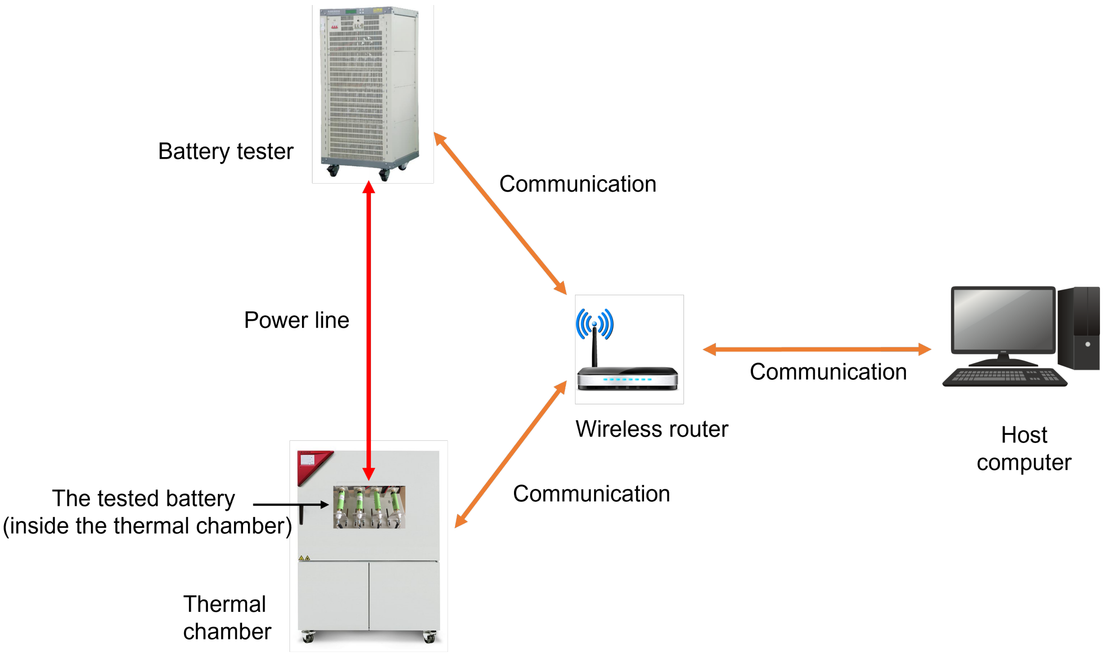

Figure 3.2: Battery test system

3.2.2 Capacity test

In this study, the battery capacity is defined as the total amount of electrical charge a battery can store. Therefore, the battery capacity can be measured by the following steps:

- Step 1: Adjust the thermal chamber to the preset temperature, and rest the battery inside the thermal chamber for 5 hours.
- Step 2: Charge the battery at a constant current (CC) rate of 0.5C until its terminal voltage reaches 4.2V.
- Step 3: Transfer the charging process into the constant voltage (CV) charging mode, which remains the battery terminal voltage at 4.2V and charges the battery under a decreasing current until the charging current falls to 65 mA. Then rest the battery for 1 hour.

- Step 4: Discharge the battery at a constant current rate of 0.5C until the terminal voltage reaches 2.5V, and then rest the battery for 1 hour.
- Step 5: Repeat Step 2 to 4 three times, then take the average value of the the discharge capacities as the measured battery capacity.

In order to obtain the battery capacity at different temperatures, the above battery capacity test is repeated at 0 °C to 50 °C with 10 °C intervals.

3.2.3 HPPC test

In order to identify the battery parameters such as OCV, internal resistances and capacitances, a series of HPPC tests at different temperature levels were conducted. Before the HPPC test, the battery is first fully charged to 100% SOC and rest for 2 hours. Then the battery is discharged to 0% SOC with 20 HPPC segments (each segment discharges the battery by 5% SOC), such as shown in Fig. 3.3.

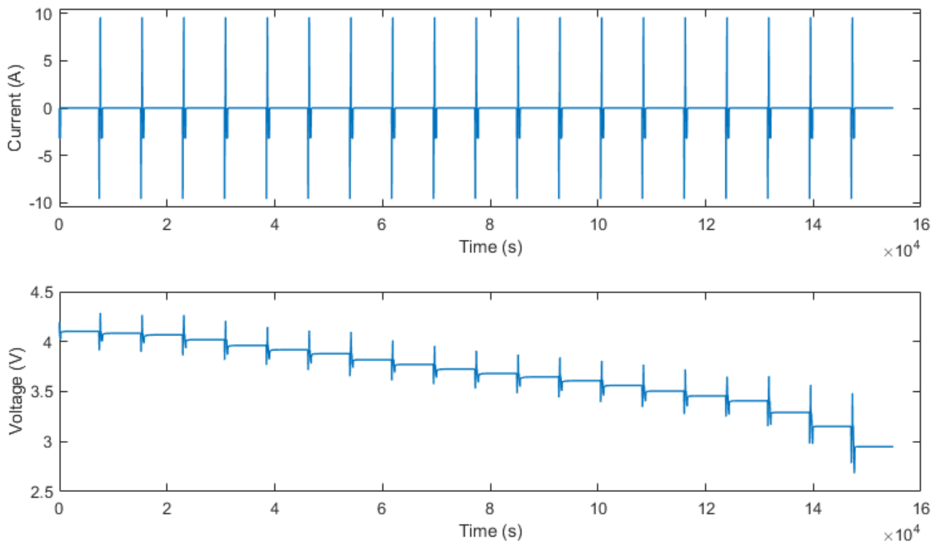

Figure 3.3: The HPPC test

In a single HPPC segment, the battery is firstly discharged under a 3C constant current for 10 seconds and rest for 3 minutes, then the battery is charged under a 3C constant current for 10 seconds and rest for 3 minutes. Then the battery is discharged under a 1C constant current until 5% SOC is discharged and rest the battery for 2 hours. The test profile of a single HPPC segment is presented in Fig. 3.4. It worth noting that the battery SOC equals to 100% at the beginning of the first segment. Therefore, in order to protect the battery from overcharging, there is no pulse load applied to this segment. The HPPC test mentioned above was performed from 0 °C to 50 °C with 10 °C intervals.

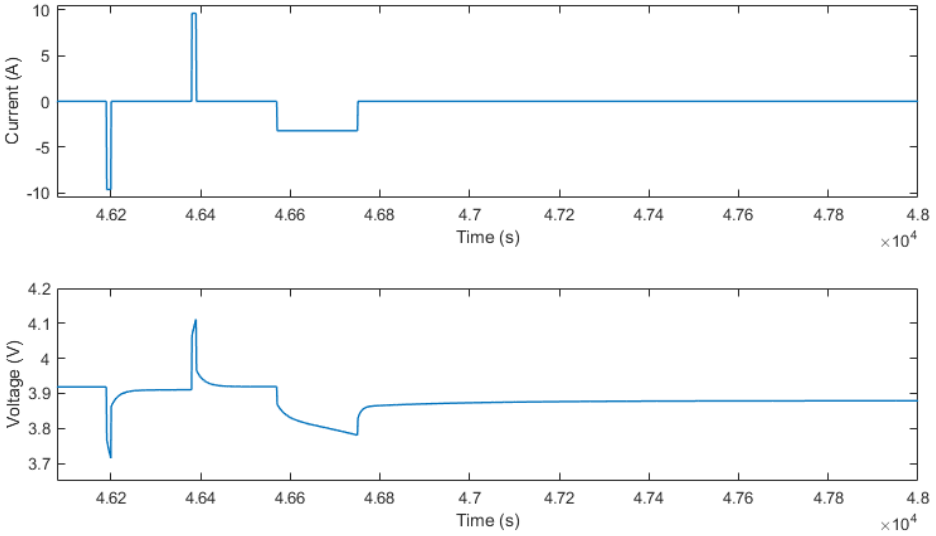

Figure 3.4: One segment of the HPPC test

3.2.4 Dynamic stress test

In order to verify the accuracy and reliability of the developed model, the dynamic stress test (DST) has been used for model validation. DST is a variable power discharge regime which can be used to simulate the dynamic performance of the

EVs [155]. In the standard DST, the battery was first charged to 100% SOC under a 0.5C charging current. Then the battery was discharged to 0% SOC through several DST segments, such as the profile shown in Fig. 3.5. The DST was also performed from 0 °C to 50 °C with 10 °C intervals.

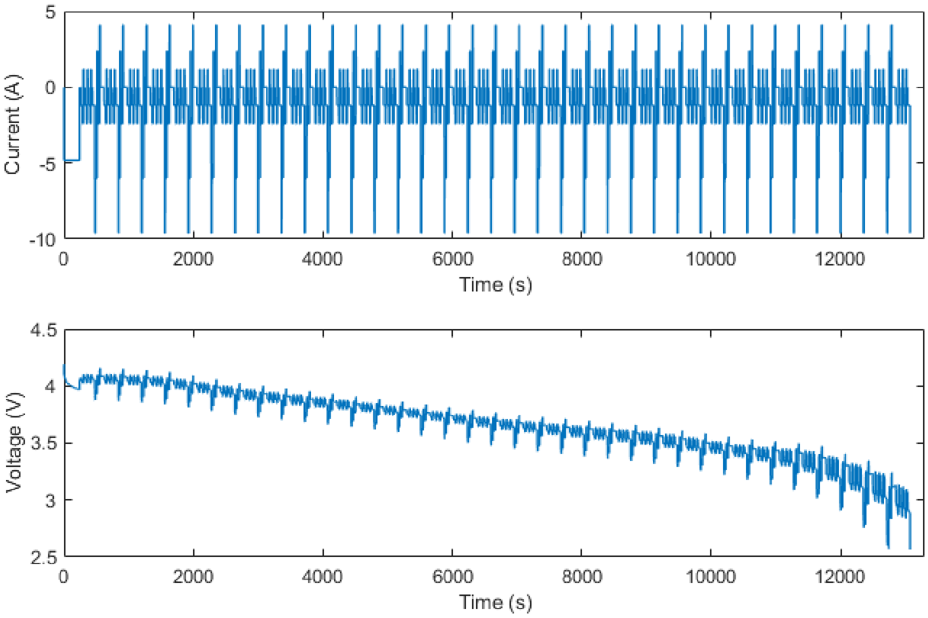

Figure 3.5: DST profile

3.3 Modelling of temperature effects

The temperature of a battery cell can greatly affect the electrochemical reactions occurring in the battery. The relationship between the rate of electrochemical reactions and reaction temperature follows the Arrhenius equation, which means the variation of battery temperature can lead to the change of electrochemical reaction rate in the battery and affects the battery performance. Therefore, the battery parameters such as capacity, OCV, polarisation resistance, and capacitances in ECMs should be modelled as functions of the battery temperature. Compared with battery surface temperature, the internal temperature of the battery is generally more suitable to be used to describe the electrochemical reaction temperature inside the battery. However, it is difficult to directly measure the internal temperature of a battery. Although some studies have tried to insert the temperature sensors inside the battery to achieve battery internal temperature measurement, this approach will not only destroy the integrity of the battery cell but may also cause battery performance degradation. Under the condition of ensuring battery integrity and not affecting battery performance, it is an optimal way to utilise battery surface temperature to represent the overall temperature condition of a battery cell. The model accuracy will only be slightly affected if the battery operates under normal conditions and the difference between internal temperature and surface temperature is insignificant. On the other hand, compared with the conventional battery ECMs that without the consideration of temperature effect, the measurement of battery surface temperature can provide sufficient information about the battery temperature condition, hence the accuracy and reliability of the model can thus be improved. Therefore, the battery surface temperature is utilised in this work to represent the overall temperature condition of a battery cell.

3.3.1 Temperature effect on battery capacity

According to the test results obtained in Section 3.2, it can be found that the battery capacity has significant changes at different temperature levels, such as shown in Fig. 3.6. It is evident that the battery capacity increases with the increase of temperature. Therefore, a look-up table, namely T - Capacity can be established to describe the relationship between the battery capacity and temperature. The battery capacity at any temperature (within the testing temperature range) can be calculated by interpolation.

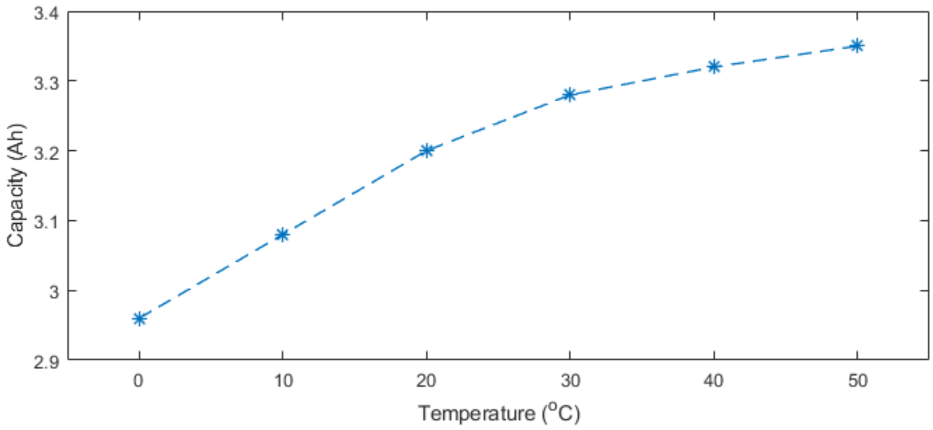

Figure 3.6: Measured battery capacity at different temperature levels

3.3.2 Temperature effect on the OCV-SOC relationship

According to the test results obtained in Section 3.2, it can be found that the battery terminal voltage relaxes to a stable value gradually when the current load is removed. The terminal voltage at the end of the rest period can be treated as the battery OCV at the corresponding SOC level. The OCV-SOC relationship obtained at different temperature levels are presented in Fig. 3.7. Based on the test results, a OCV-SOC-T lookup table can be established to describe the relationship between the battery OCV, SOC and temperature. Once the battery SOC and temperature T are determined, the battery OCV can be calculated via the OCV-SOC-T lookup table.

3.3.3 Temperature effect on battery internal resistances and capacitances

In order to determine the battery parameters, such as the internal resistances and capacitances, the Recursive Least Squares (RLS) method with forgetting factor [156] is used in study to identify the parameters in the DP model. According to

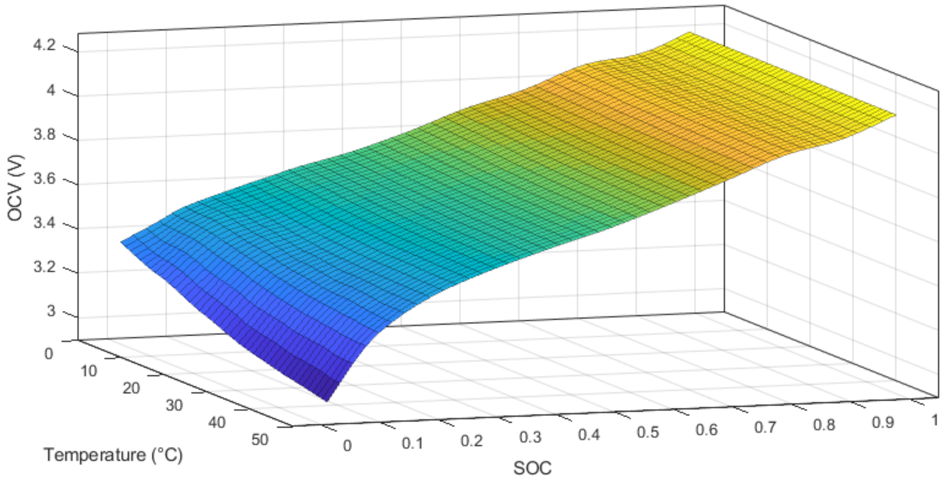

Figure 3.7: The relationship between OCV, SOC and temperature

Equation. (3.1), the transfer function of the DP model can be written as:

$$G(s) = \frac{E(s)}{I(s)} = R_0 + \frac{R_1}{1+\tau_1(s)} + \frac{R_2}{1+\tau_2(s)} \tag{3.3}$$

where $E(s)$ represents the difference between battery terminal voltage and OCV in S domain, $E(s) = V_t(s) - V_{OC}(s)$. $\tau_1 = R_1C_1$, $\tau_2 = R_2C_2$. Equation. (3.3) can be rewritten as

$$G(s) = \frac{R_0 s^2 + \frac{R_0\tau_1 + R_0\tau_2 + R_1\tau_2 + R_2\tau_1}{\tau_1\tau_2} s + \frac{R_0+R_1+R_2}{\tau_1\tau_2}}{s^2 + \frac{\tau_1+\tau_2}{\tau_1\tau_2} s + \frac{1}{\tau_1\tau_2}} \tag{3.4}$$

Based on the Bilinear transformation $s = \frac{2}{T_s}\frac{z-1}{z+1}$, the transfer function can be transformed from S domain to Z domain.

$$G(z^{-1}) = \frac{E(k)}{I(k)} = \frac{\theta_3 + \theta_4 z^{-1} + \theta_5 z^{-2}}{1 - \theta_1 z^{-1} - \theta_2 z^{-2}} \tag{3.5}$$

where

$$\begin{cases} \theta_1 = -\dfrac{2T_s^2 - 8\tau_1\tau_2}{T_s^2 + 2T_s(\tau_1 + \tau 2) + 4\tau_1\tau_2} \\ \theta_2 = -\dfrac{T_s^2 - 2T_s(\tau_1 + \tau 2) + 4\tau_1\tau_2}{T_s^2 + 2T_s(\tau_1 + \tau_2) + 4\tau_1\tau_2} \\ \theta_3 = \dfrac{T_s^2(R_0 + R_1 + R_2) + 2T_s(R_0\tau_1 + R_0\tau_2 + R_1\tau_2 + R_2\tau_1) + 4R_0\tau_1\tau_2}{T_s^2 + 2T_s(\tau_1 + \tau_2) + 4\tau_1\tau_2} \\ \theta_4 = \dfrac{2T_s^2(R_0 + R_1 + R_2) - 8R_0\tau_1\tau_2}{T_s^2 + 2T_s(\tau_1 + \tau_2) + 4\tau_1\tau_2} \\ \theta_5 = \dfrac{T_s^2(R_0 + R_1 + R_2) - 2T_s(R_0\tau_1 + R_0\tau_2 + R_1\tau_2 + R_2\tau_1) + 4R_0\tau_1\tau_2}{T_s^2 + 2T_s(\tau_1 + \tau_2) + 4\tau_1\tau_2} \end{cases} \tag{3.6}$$

where T_s is the sampling period.

Define

$$\begin{cases} \Phi(k) = [E(k-1)\; E(k-2)\; I(k)\; I(k-1)\; I(k-2)] \\ \Theta(k) = [\theta_1\; \theta_2\; \theta_3\; \theta_4\; \theta_5]^T & (3.7) \\ y(k) = \Phi(k)\Theta(k) + e(k) & (3.8) \end{cases}$$

where e(k) is the prediction error of $E(k)$.

To identify the parameter vector $\Theta(k)$, RLS algorithm with forgetting factor is utilised in this work. The parameter identification is implemented as follows.

$$e(k) = E(k) - \Phi(k)\hat{\Theta}(k) \tag{3.9}$$

$$K(k) = \frac{P(k-1)\Phi^T(k)}{\lambda + \Phi^T(k)P(k-1)\Phi(k)} \tag{3.10}$$

$$P(k) = \frac{P(k-1) - K(k)Phi^T(k)P(k-1)}{\lambda} \tag{3.11}$$

$$\hat{\Theta}(k) = \hat{\Theta}(k-1) + K(k)e(k) \tag{3.12}$$

where $K(k)$ is the algorithm gain. $P(k)$ is the covariance matrix. λ is the forgetting factor which is typically set between 0.95 to 1. In this work, λ is maintained as 0.98.

Therefore, the corresponding model parameters R_0, R_1, R_2, C_1 and C_2 can be calculated as follows.

Suppose

$$\begin{cases} \alpha_1 = R_0 \\ \alpha_2 = \tau_1\tau_2 \\ \alpha_3 = \tau_1 + \tau_2 \\ \alpha_4 = R_0 + R_1 + R_2 \\ \alpha_5 = R_0\tau_1 + R_0\tau_2 + R_1\tau_2 + R_2\tau_1 \end{cases} \tag{3.13}$$

Equation. (3.6) can thus be simplified as

$$\begin{cases} \theta_1 = \dfrac{8\alpha_2 - 2T_s^2}{4\alpha_2 + 2\alpha_3 T_s + T_s^2} \\ \theta_2 = \dfrac{4\alpha_3 T_s}{4\alpha_2 + 2\alpha_3 T_s + T_s^2} - 1 \\ \theta_3 = \dfrac{4\alpha_1\alpha_2 + 2\alpha_5 T_s + \alpha_4 T_s^2}{4\alpha_2 + 2\alpha_3 T_s + T_s^2} \\ \theta_4 = -\dfrac{8\alpha_1\alpha_2 - 2\alpha_4 T_s^2}{4\alpha_2 + 2\alpha_3 T_s + T_s^2} \\ \theta_5 = \dfrac{4\alpha_1\alpha_2 - 2\alpha_5 T_s + \alpha_4 T_s^2}{4\alpha_2 + 2\alpha_3 T_s + T_s^2} \end{cases} \tag{3.14}$$

Therefore, Equation. (3.15) can be obtained by Equation. (3.14).

$$\begin{cases} \alpha_1 = \dfrac{\theta_3 - \theta_4 + \theta_5}{1 + \theta_1 - \theta_2} \\ \alpha_2 = \dfrac{T_s^2(1 + \theta_1 - \theta_2)}{4(1 - \theta_1 - \theta_2)} \\ \alpha_3 = \dfrac{T_s^2(1 + \theta_2)}{1 - \theta_1 - \theta_2} \\ \alpha_4 = \dfrac{\theta_3 + \theta_4 + \theta_5}{1 - \theta_1 - \theta_2} \\ \alpha_5 = \dfrac{T_s(\theta_3 - \theta_5)}{1 - \theta_1 - \theta_2} \end{cases} \tag{3.15}$$

Suppose $\tau_1 = (\alpha_3 + \sqrt{\alpha_3^2 - 4\alpha_4})/2$ and $\tau_2 = (\alpha_3 - \sqrt{\alpha_3^2 - 4\alpha_4})/2$, the model parameters R_0, R_1, R_2, C_1 and C_2 thus can be calculated by Equation. (3.16).

$$\begin{cases} R_0 = \alpha_1 \\ R_1 = [\tau_1(\alpha_4 - \alpha_1) + \alpha_1\alpha_3 - \alpha_5]/(\tau_1 - \tau_2) \\ R_2 = \alpha_4 - \alpha_1 - R_1 \\ C_1 = \tau_1/R_1 \\ C_2 = \tau_2/R_2 \end{cases} \tag{3.16}$$

Therefore, once the parameter vector $\Theta(k)$ is determined, the corresponding model parameters can be calculated via (3.15) and (3.16).

The identified parameters in terms of battery internal resistances and capacitances are shown in Fig. 3.8 and Fig. 3.9, respectively. It can be seen that the battery internal resistance increases as the temperature decreases, and the battery internal capacitance increases as the temperature increases. To map the relationship between the model parameters, SOC and temperature, five look-up tables, namely R_0-*SOC*-*T*, R_1-*SOC*-*T*, R_2-*SOC*-*T*, C_1-*SOC*-*T* and C_2-*SOC*-*T* have been established.

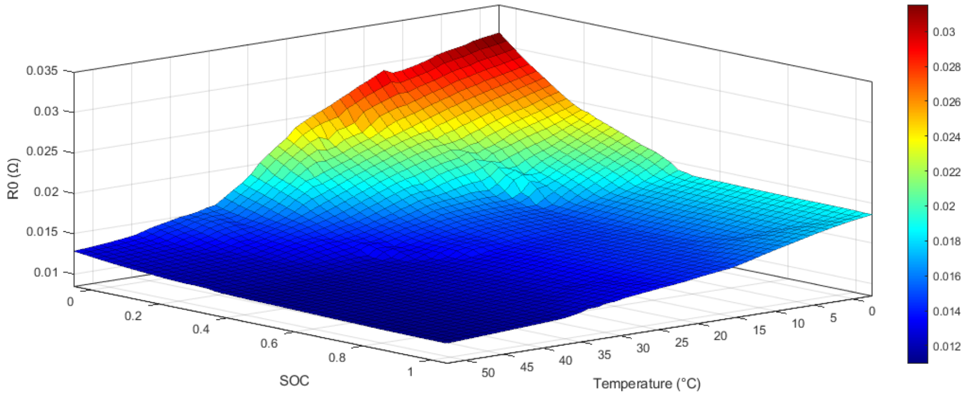

(a) The relationship between R_0, SOC and temperature

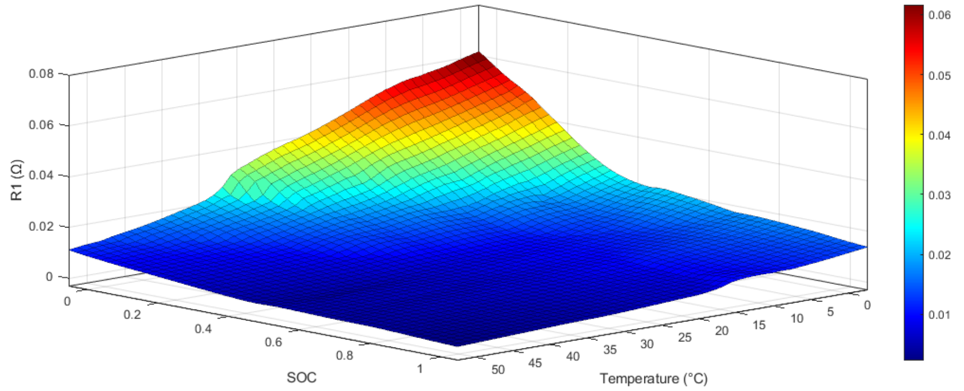

(b) The relationship between R_1, SOC and temperature

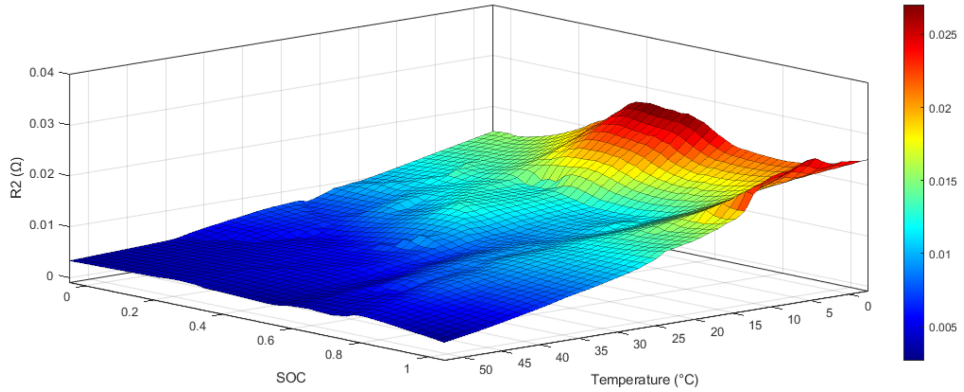

(c) The relationship between R_2, SOC and temperature

Figure 3.8: The relationship between resistances, SOC and temperature

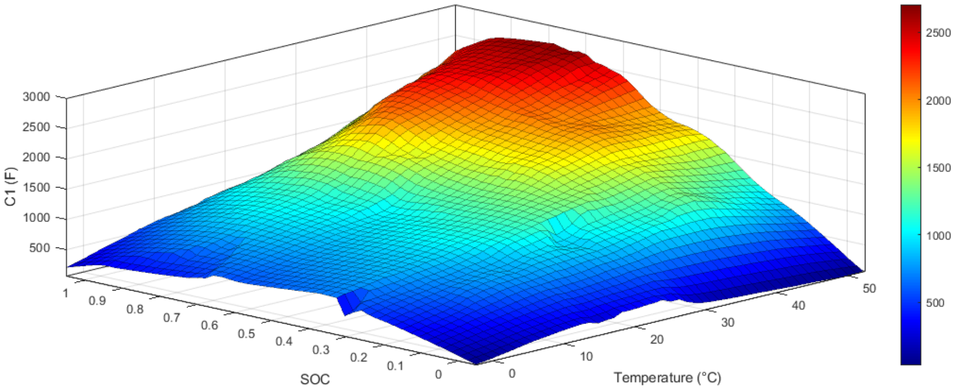

(a) The relationship between C_1, SOC and temperature

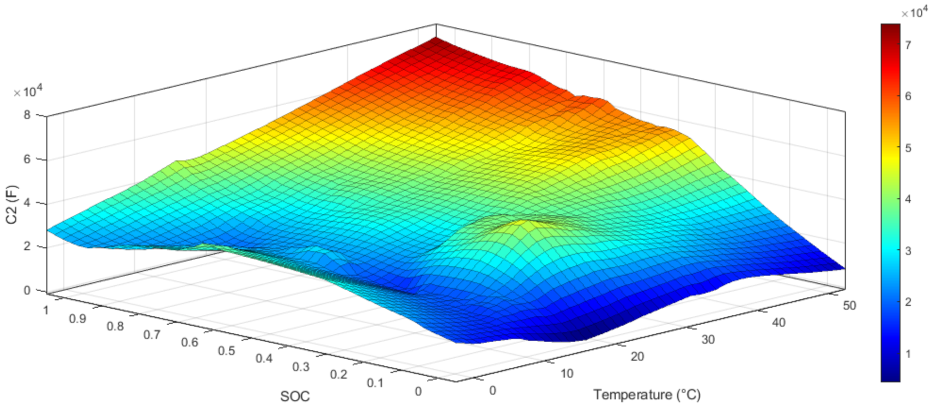

(b) The relationship between C_2, SOC and temperature

Figure 3.9: The relationship between capacitances, SOC and temperature

3.3.4 Temperature effect on battery energy efficiency

Since the reaction temperature affects the rate of electrochemical reactions inside the cell, the operating temperature also influences the energy efficiency of the battery. The electrochemical reaction rate increases with increasing battery operating temperature and vice versa. Low operating temperature causes the increase of internal impedance, which leads to the decrease of battery energy. The battery energy efficiency at different operating temperatures is shown in Fig. 3.10. It can be seen that when the operating temperature reduces to 0 °C, the energy efficiency of the battery will drop to about 71%. Therefore, an appropriate operating temperature range not only prevents the battery from safety risks but also help to achieve better energy efficiency.

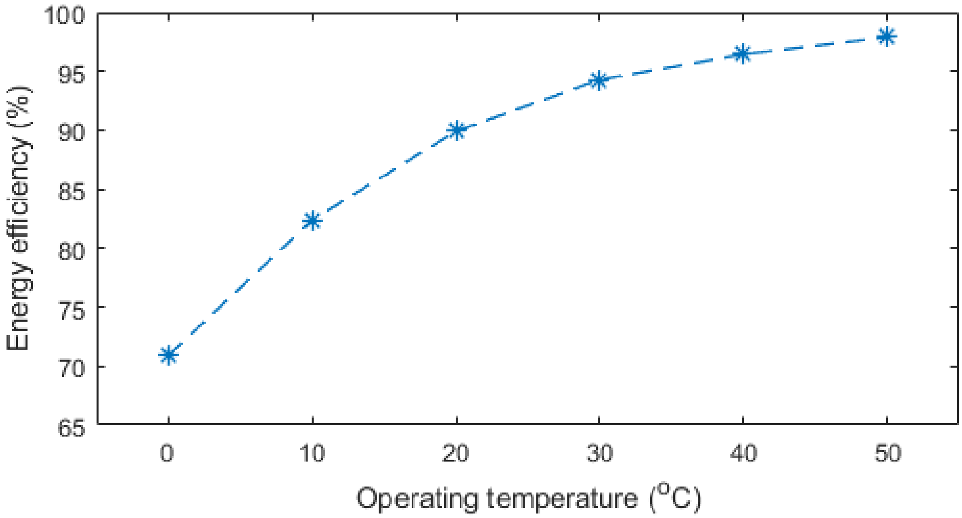

Figure 3.10: Battery energy efficiency at different temperatures

3.4 Model validation

The model validation tests were performed under the DST profiles to verify the accuracy and reliability of the developed temperature-compensated DP model. The battery terminal voltage is predicted via Equation. (3.2). Taking the ambient temperature at 30 °C as an example, the measured voltage and the predicted voltage under the DST profile are compared in Fig. 3.11. It can be seen that the developed model can accurately capture the dynamic voltage response.

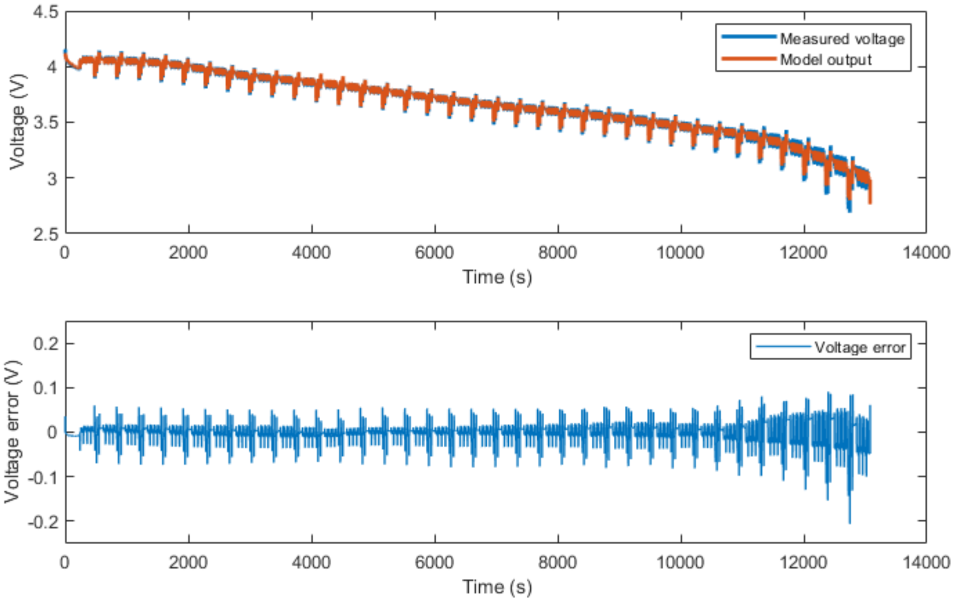

Figure 3.11: Voltage prediction results under the DST profile at 30 °C

The DST validations have been performed at 0 °C, 10 °C, 20 °C, 30 °C, 40 °C and 50 °C, respectively. The voltage prediction results in terms of mean absolute error (MAE) and root mean square error (RMSE) at different temperature are shown in Table 3.2. It can be seen that the results of MAE are always within 0.5% at different temperatures and the results of RMSE are always within 1%. Therefore, it can be concluded that the developed model can accurately capture the battery dynamics at different temperatures.

Table 3.2: Voltage prediction results at different temperatures

Temperature	0 °C	10 °C	20 °C	30 °C	40 °C	50 °C
MAE	0.3319%	0.2797%	0.2520%	0.3358%	0.3704%	0.3946%
RMSE	0.4934%	0.4597%	0.3988%	0.5076%	0.5619%	0.6030%

3.5 SOC estimation with the developed model

To further analyse the importance of the temperature compensation, the developed temperature-compensated DP model is also utilised for SOC estimation at different temperatures.The operating temperature of the tested cell ranges from 0 °C to 50 °C. Exceeding the temperature range may cause a sharp drop in battery performance, irreversible damages, and even cause an internal short circuit, fire, and explosion. Therefore, two test temperature conditions (5 °C and 45 °C) that are close to the lower and upper bounds of the specified operating temperature range are utilised for model verification.

According to [157], the SOC expression can be determined as

$$SOC_k = SOC_{k-1} + \frac{\eta \Delta t I_k}{3600 \times C_T} \tag{3.17}$$

where η represents the battery charge-discharge efficiency, which is assumed as 1 in this study. Δt is the sampling time, which is set as 1s in this study. I_k represents the battery current at time k. I_k is defined as positive in charging and negative in discharging. C_T is the battery capacity at temperature T, which can be determined via the Capacity-T look-up table.Therefore, the discrete space state of the DP model can be expressed as

$$\begin{cases} SOC_k = SOC_{k-1} + \dfrac{\eta \Delta t I_k}{3600 \times C_T} \\ V_{1,k} = e^{-\frac{\Delta t}{R_1 C_1}} V_{1,k-1} + (1 - e^{-\frac{\Delta t}{R_1 C_1}}) R_1 I_k \\ V_{2,k} = e^{-\frac{\Delta t}{R_2 C_2}} V_{2,k-1} + (1 - e^{-\frac{\Delta t}{R_2 C_2}}) R_2 I_k \end{cases} \tag{3.18}$$

The system observation equation is expressed as:

$$V_{t,k} = V_{OC,k} + I_k R_0 + V_{1,k} + V_{2,k} \tag{3.19}$$

where $V_{t,k}$ and $V_{OC,k}$ represent the battery terminal voltage and OCV at time k, respectively.

Therefore, the system state variable can be defined as

$$x_k = [SOC_k, V_{1,k}, V_{2,k}]^T \tag{3.20}$$

and the observation variable can be defined as

$$y_k = V_{t,k} \tag{3.21}$$

As discussed in Chapter 2, an ECM typically works with a filter or observer to realise the real-time estimation of the battery SOC. Among the various filters and observers, the extended Kalman filter (EKF) is one of the most popular techniques for battery states estimation. Therefore, the EKF algorithm is utilised in this work for battery SOC estimation.

3.5.1 Implementation of EKF

As a classic algorithm in state estimation, Kalman filter has been widely utilised in various applications. In Kalman filter, the system state is firstly predicted using the state equation, and then the system output can be predicted using the measurement equation. Once a new measurement becomes available, the prediction error can be calculated and used to correct the prediction of the state. In such a prediction-correction approach, Kalman filter can effectively estimate the sates in linear systems. To extend the Kalman filter to non-linear systems, extended Kalman filter (EKF) is proposed which using first-order Taylor series to linearise the system at the current operating point.

Considering a nonlinear dynamic system model which the state equation and the measurement equation are defined as:

$$\begin{cases} x_{k+1} = f_k(x_k, u_k, w_k) & (3.22) \\ y_k = h_k(x_k, v_k) & (3.23) \end{cases}$$

where k is the time index, u_k is the system input. x_k and y_k represent the state and measurement of the system, respectively. The functions $f_k(.)$ and $h_k(.)$ are the nonlinear process equation and the measurement equation, respectively. w_k and v_k represent the system process noise and the measurement noise, respectively. w_k and v_k are assumed to be independent zero-mean white Gaussian noise, and $E(w_k w_k^T) = Q_k$, $E(v_k v_k^T) = R_k$.

Suppose the system process equation and the measurement equation are differentiable at all time, the state transition matrix then can be calculated as

$$\begin{cases} A_k = \frac{\partial f(x_k)}{\partial x_k}|_{x_k=\hat{x}_k^-} & (3.24) \\ C_k = \frac{\partial h(x_k)}{\partial x_k}|_{x_k=\hat{x}_k^-} & (3.25) \end{cases}$$

Suppose $\hat{x}_k^-$ and $\hat{x}_k$ are the priori sate estimation and posterior state update, respectively. P_k^- and P_k are the priori sate covariance update and posterior state covariance update, respectively. The implementation procedure of the EKF is given below.

For $k = 0$:

- Initialise $\hat{x}_0$, $P_0 = E\{(x_0 - \hat{x}_0)(x_0 - \hat{x}_0)^T\}$

For $k =$ 1,2,3,...

- State estimate:

$$\hat{x}_k^- = f(\hat{x}_{k-1}, u_{k-1}) \tag{3.26}$$

- State covariance prediction:

$$P_k^- = A_k P_{k-1} A_k^T + Q_{k-1} \tag{3.27}$$

- Gain calculation:

$$K_k = P_k^- C_k^T (C_k P_k^- C_k^T + R_k)^{-1} \tag{3.28}$$

- State update:

$$\hat{x}_k = \hat{x}_k^- + K_k(y_k - h(\hat{x}_k^-)) \tag{3.29}$$

- State covariance update:

$$P_k = (I - K_k C_k) P_k^- \tag{3.30}$$

3.5.2 Results and discussion

In order to verify the effectiveness of the developed method in low and high temperature environments, the SOC estimation tests were performed at 5 °C and 45 °C, respectively. The EKF algorithm based on the DP model with temperature compensation is denoted as T-EKF, and the T-EKF algorithm implementation is shown in Fig. 3.12. The EKF algorithm based on the DP model without temperature compensation (the DP model is established at room temperature) is denoted as EKF. To test the robustness of the developed SOC estimation method, the initial SOC in the T-EKF and EKF is set 0.5, and the actual initial SOC of the battery is 0.8.

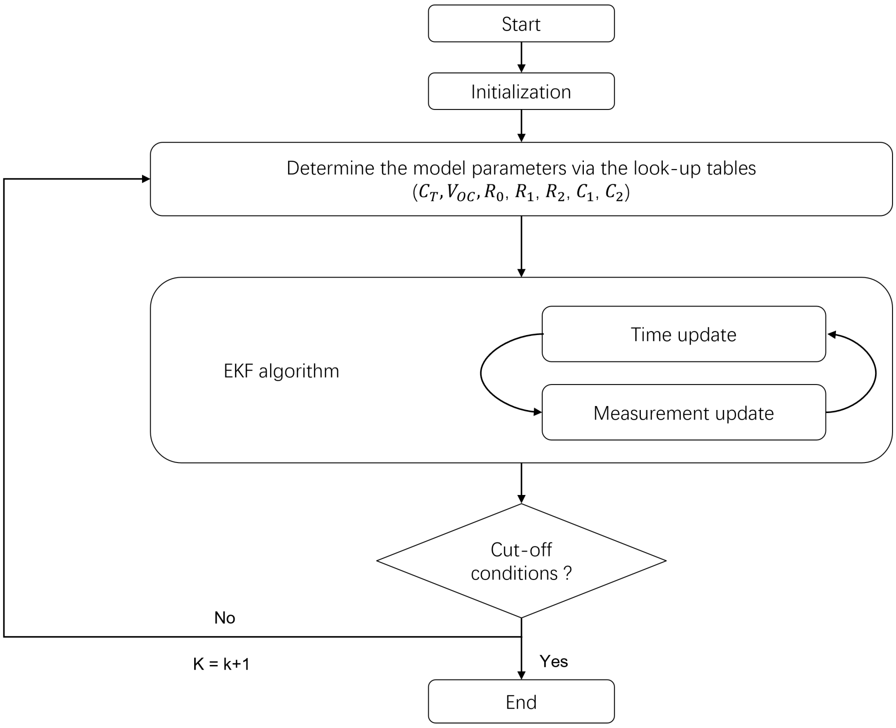

Figure 3.12: The flow chart of SOC estimation using EKF

The SOC estimation results at 5 °C are shown in Fig. 3.13. It is evident that the SOC estimated by the EKF algorithm has large errors in low temperature environment regardless of the temperature compensation. The numerical SOC estimation results are shown in Table 3.3. It can be seen that T-EKF can achieve better SOC estimation results in terms of RMSE, MAE and maximum absolute error (MaxAE).

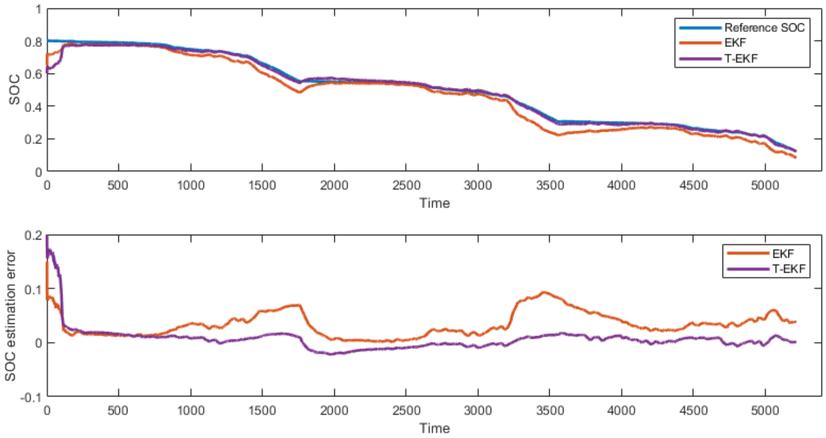

Figure 3.13: Results of SOC estimation at 5 °C

Table 3.3: SOC estimation results at 5 °C

	RMSE (%)	MAE (%)	MaxAE (%)
EKF	4.0488	3.3631	9.3962
T-EKF	2.3756	1.2301	2.7153

The SOC estimation results at 45 °C are shown in Fig. 3.14. Again, it can be seen that the SOC estimated by EKF algorithm has large errors in low temperature environment regardless of the temperature compensation. The numerical SOC estimation results are shown in Table 3.4. It can be seen that T-EKF can achieve better SOC estimation results in terms of RMSE, MAE and maximum absolute error (MaxAE).

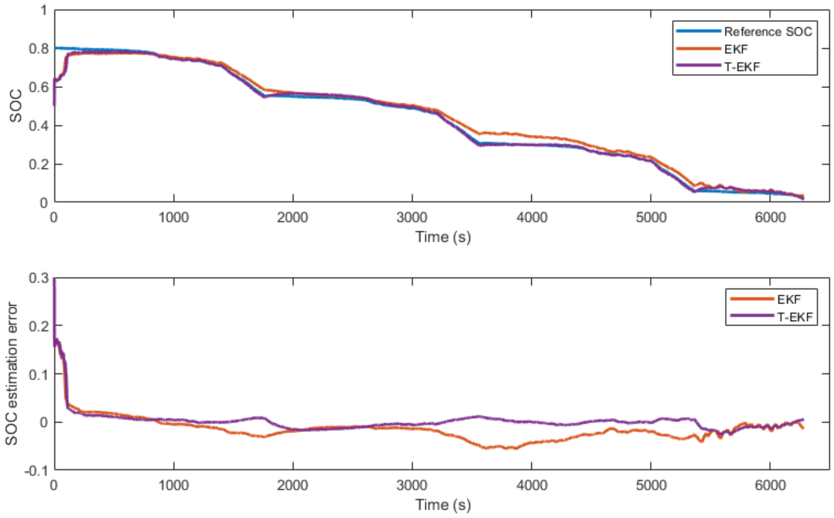

Figure 3.14: Results of SOC estimation at 45 °C

Table 3.4: SOC estimation results at 45 °C

	RMSE (%)	MAE (%)	MaxAE (%)
EKF	3.0952	2.3301	5.5340
T-EKF	2.1333	0.9493	2.5865

3.6 Chapter summary

In order to develop an accurate battery model that can be utilised over a wide range of temperature, a DP model with temperature compensation is developed in this chapter. The parameters in the DP model are identified at various battery SOC and temperature levels. The test results reveal that the DP model with temperature compensation can accurately capture the battery dynamic response at different temperatures.

The developed DP model with temperature compensation is also applied to estimate battery SOC at different temperatures.Two estimation methods, namely T-EKF and EKF are applied on the FUDS test data. The test result shows that the battery SOC estimation error caused by the temperature effect can be effectively reduced with the utilisation of T-EKF. Compared with the conventional EKF method, the T-EKF method can achieve more accurate SOC estimation in terms of RMSE, MAE and MaxAE.

Chapter 4

Battery temperature monitoring

Temperature monitoring is one of the key functions in a battery management system (BMS) since inappropriate operating temperature may seriously affect the lithium-ion batteries, such as performance degradation, reduced service life, and even causing fire or explosion. Among the various temperature measurement techniques, Fiber Bragg-grating (FBG) sensing is gaining more attention due to its advantages of small size, resistance to corrosion and immunity to electromagnetic radiation. However, the conventional temperature calibration method for FBG sensors needs to be completed under the laboratory conditions. This not only requires a high-standard test environment, but also causes the sensors to fail to work properly during the calibration or re-calibration processes. In order to overcome the shortcomings of the conventional temperature calibration methods, a data-driven based FBG temperature calibration method is developed in this chapter. Firstly, Fuzzy C-means algorithm is used to extract the linear relationship between the measured wavelength shift and temperature variation. Empirical mode decomposition (EMD) technique is then applied to decompose the remaining wavelength information. The intrinsic mode functions (IMFs) and the residual achieved by EMD are classified according to their frequency characteristics. The rest wavelength information is further modelled as a system compensation depends on cell SOC and cycle number. Finally, the linear relationship and system compensation are combined to form the developed temperature calibration method. The validation results show that the developed method has good accuracy and reliability. Compared with the conventional temperature calibration method, the developed method can be used online without affecting the normal operation of the energy storage system (ESS). Moreover, the developed method does not require a high-standard laboratory environment and is more friendly in engineering applications.

4.1 Monitoring of battery temperature

In recent years, the public has paid more attention to lithium-ion batteries due to its high energy density and power density, which can meet the demands of various applications [158]. How to guarantee the operational safety of lithium-ion battery is always a concern in both battery design and utilisation. It is widely recognised that inappropriate operation temperature can cause lithium-ion battery performance degradation and failure [58; 159]. Therefore, thermal management plays an essential role in battery management system (BMS) to control battery operation temperature. In order to development a reliable battery thermal management strategy, battery temperature monitoring is indispensable.

Regarding the battery temperature monitoring, the internal temperature of the cell can accurately describe the temperature of the electrochemical reaction that occurs inside the battery. However, it is difficult to directly measure the internal temperature of a battery. The battery surface temperature and internal temperature are positively correlated, and the battery surface temperature is generally lower than the internal temperature. Therefore, battery surface temperature monitoring can also effectively prevent the occurrence of thermal runaway and ensure that the battery works in a safe temperature range. Furthermore, accurate battery surface temperature monitoring can also help to develop advanced algorithms for battery internal temperature estimation.

Among the various temperature measurement techniques in BMS, thermocouple and thermistor are the most widely used ones in current BMS for battery temperature monitoring. They can be attached to the strategic locations on the battery shell to monitor the battery surface temperature [160], or insert inside the battery to measurement its internal temperature [161]. The advantages of these temperature sensing techniques can be summarised as low cost, small size, wide temperature measurement range and moderate measurement accuracy in commercial applications [162]. However, whether thermocouples or thermistors, the long-term reliability are difficult to maintain due to they are sensitivity to corrosion and electromagnetic radiation. On the other hand, for a large energy storage system, a large number of local temperatures at different locations need to be measured to generate the temperature distribution profile of batteries in real time. This will significantly increase the number of sensors, cables, and other supporting facilities of the BMS, which makes the limited space more insufficient. Therefore, Fiber Bragg-grating (FBG) sensors have attracted substantial interests in battery thermal management due to the advantages of smaller size, mechanical robustness, resistance to corrosion and immune to electromagnetic radiation [143]. Moreover, multiplex measurement is another advantage of FBG sensor. A single optical fiber can be inscribed with multiple FBGs to perform temperature measurements at multiple locations along the fiber, which can save a lot of cost and space in multi-point measurements [162].

FBG sensors measure temperature according to the effective refractive index of the core and the grating period, which results a shift of the reflected spectrum [163]. It is worth noting that the external load will also contribute to a peak shift in the reflected wavelength. When using a FBG sensor to measure the temperature of a battery during the operation, the resonant wavelength peak shift is generally created by the variations of both temperature and strain. Temperature independent measurement cannot be achieved unless the strain variation effects on wavelength peak shift are eliminated. Various decoupling method of temperature and strain have reported in [164; 165; 166], temperature calibration is a prerequisite for all of these methods. Generally, temperature calibration procedure needs to be performed in a laboratory environment without external load impact.

For example, specific constant external temperature environments controlled by a thermal chamber should be applied for both of the specimen (battery cell) and the FBG sensor. The external temperature should be kept for a long enough period to ensure the temperature homogenisation in the specimen and FBG sensor is achieved. The thermo-optic coefficient and the host material thermal expansion coefficient can be calibrated consequently [164]. Although this temperature calibration method can accurately identify relevant parameters, it still faces the following drawbacks. Firstly, the calibration method can only be performed offline, which means that it cannot be applied to the FBG sensors that have already been mounted on the ESS in temperature monitoring operation. Secondly, this method requires a high-precision thermal chamber to ensure the reliability of the calibration results. Last but not least, if a large number of FBG sensors are utilised for large energy storage system (ESS) temperature monitoring, this calibration method leads to tremendous workload for the regular re-calibration procedure.

To overcome the shortcomings of conventional temperature calibration method for FBG sensors, a novel data driven based temperature calibration method is developed in this chapter. The developed method can operate online without the requirement of high standard laboratory environment and it is more user friendly in engineering applications.

4.2 Experimental setup

Four commercial 18650 $LiFePO_4$ lithium-ion battery cells have been utilised in this study. The nominal voltage and capacity of each cell are 3.2 V and 1.6 Ah respectively. For each cell, three FBG sensors, namely FBG 1, FBG 2 and FBG 3 are mounted on the pre-designed locations of the cell shell, as shown in Fig. 5.1. The FBG sensors were manufactured using the phase mask method and inscribed in photosensitive fibre. A Micron-Optics SM-130 interrogator is used for FBG based measurements. The characteristic wavelengths of FBG 1, FBG 2 and FBG 3 are set as 1534 nm, 1539 nm and 1544 nm, respectively. For each cell, a thermocouple is attached to the location close to the FBG sensors to measure the battery surface temperature as a reference. The base temperature (T_0) is set as 25 $°C$ in this study. A NEWARE BTS-4000 battery test system is utilised to cycle the cells in the room temperature environment and acquires the current and voltage signals of the cells. The sampling frequency for all the measurement equipment in this experiment is set as 1 Hz.

Figure 4.1: The layout of the FBG sensors

Standard cycle profile was employed to the examined cells which includes a Constant-Current Constant-Voltage (CC-CV) charging process and a Constant-

Current (CC) discharging process. For the CC-CV charging process, the cell is charged under a 1.6 A constant current until the terminal voltage reaches the upper cutoff voltage (3.6 V), the cell then is charged under the constant voltage until the charing current decreases to 75 mA. For the CC discharging process, a 1.6 A constant current was employed to discharge the cell to the lower cutoff voltage of 2.0 V. The rest time between each charging and discharging process is set to 10 minutes. During the battery operation, heat will be generated inside the cell and transfers to the surface of the battery. Therefore, the measured temperature at battery shell has an upward trend during the charging and discharging processes and a downward trend during the rest period, as shown in Fig. 4.2 (a). Since the FBG sensors are placed very close to each other, the peak wavelength measurement via FBG 1, FBG 2 and FBG 3 can be assumed to have the same influence by the temperature variation. Therefore, the similar upward and downward trends during battery operation can also be obtained in the measured peak wavelength via FBG 1, FBG 2 and FBG 3, as shown in Fig. 4.2 (b) - (d). It can be seen that the measured peak wavelength data via the FBG sensors are highly correlated with the temperature data measured via the thermocouple, which implies that the peak wavelength information can be utilised to predict the battery shell temperature. The obtained peak wavelength data also implies that during the battery operation, the temperature variation causes grater influence than the variation of strain.

In this study, the peak wavelength data collected from FBG 1 of Cell 1 is used to illustrate the battery shell temperature monitoring. The data obtained in Cycle 1 to 11 is utilised for modelling and the data in Cycle 12 to 22 is applied for model validation.

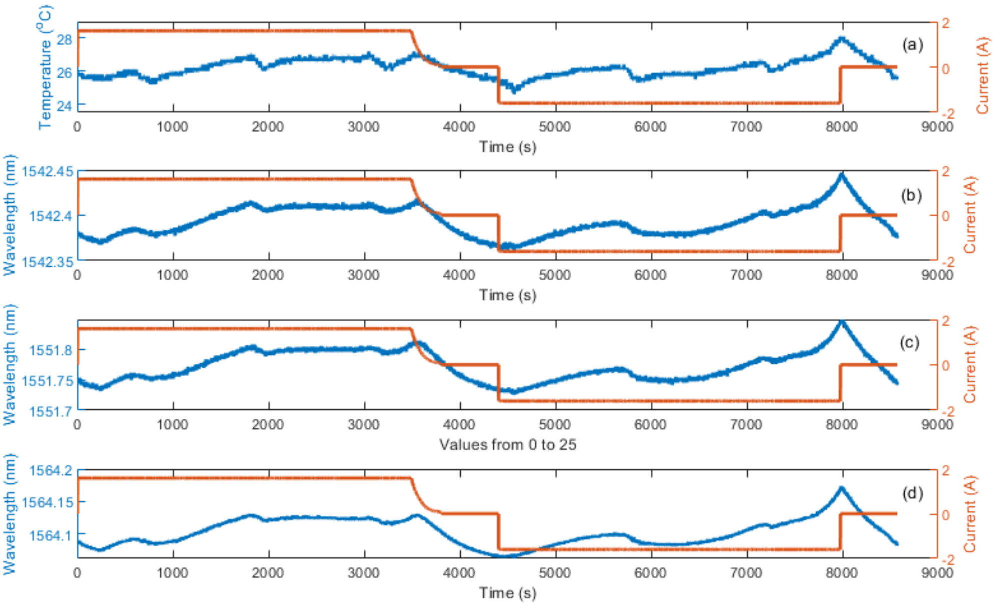

Figure 4.2: The temperature and peak wavelengths measured during the charging and discharging process: (a) Thermocouple. (b) FBG 1. (c) FBG 2. (d) FBG 3.

4.3 Data driven based temperature calibration

4.3.1 FBG working principle

A FBG sensor reflects a certain narrow slice of spectrum and the centred peak wavelength is selected as known as the Bragg wavelength [146]. The thermal or mechanical behaviours, such as the change of temperature and strain will lead to a shift of the reflected wavelength, which is expressed as:

$$\lambda = 2n_{eff}\Lambda \tag{4.1}$$

where n_{eff} is the effective refractive index at grating location and Λ is the constant refractive index modulation [164]. The wavelength shift ($\Delta\lambda$) caused by temperature variation (ΔT) and strain variation ($\Delta\varepsilon$) can be expressed as:

$$\frac{\Delta\lambda}{\lambda} = (\alpha + \xi)\Delta T + (1 + P_e)\Delta\varepsilon \tag{4.2}$$

where P_e is the photo-elastic coefficient, α represents the thermal expansion coefficient and ξ represents the thermo-optic coefficient [146].

Since the thermal expansion coefficient α, thermo-optic coefficient ξ of the fiber material are the constant in this case, Eq. (4.2) can be thus simplified as follows.

$$\Delta\lambda = f(\Delta T) + Z \tag{4.3}$$

where $f(\Delta T)$ represents the temperature variation effect on wavelength shift, Z represents the residual wavelength shift information which cannot be described by $f(\Delta T)$. In other words, Z reflects the influence of strain and other unknown factors on $\Delta\lambda$. Therefore, it yields

$$\Delta T = f^{-1}(\Delta\lambda - Z) \tag{4.4}$$

4.3.2 Modelling of the temperature influence

The relationship between temperature variation and wavelength shift have been studied in [140; 166; 167], the results indicate that the variation of temperature is a linear function of wavelength shift. However, it should be noted that the wavelength shift measured in the experiments are the results of temperature variation, strain change and other unknown factors. The measured cell surface temperature variation ΔT and the measured wavelength shift $\Delta\lambda$ are shown as the blue points in Fig. 4.3. In order to extract the temperature effect from the other factors, clustering methods can be employed to extract the relationship between the temperature variation ΔT and the wavelength shift $\Delta\lambda$. Among various clustering methods, the Fuzzy C-means (FCM) is one of the most widely used clustering method due to the advantages of robustness for ambiguity and maintains much more information than the hard clustering methods [168]. FCM is an iterative process which partition the input data into a certain number of clusters with the respect to the membership value and the distance. For a dataset of points, namely x, $x = (x_1, x_2, ...x_N)$, the FCM objective function can be expressed as

$$J_m(U,P) = \sum_{j=1}^{N}\sum_{i=1}^{c}(\mu_{ij})^m(d_{ij})^2 \tag{4.5}$$

where N is the number of input data, P is the cluster center matrix, U is the membership function matrix. μ_{ij} is the likelihood value which presents the degree of the i^{th} input data belonging to the j^{th} cluster, which satisfies the constraints in Eq. (4.6). m is a parameter used to set the fuzziness of the cluster. d_{ij} is the distance between the i^{th} input data and the j^{th} cluster center. In this paper, the distance refers to Euclid distance.

$$\begin{cases} \sum_{i=1}^{c}\mu_{ij} = 1, j = 1, 2, ..., N \\ 0 \leq \mu_{ij} \leq 1, i = 1, 2, ..., c, j = 1, 2, ..., N \\ 0 < \sum_{j=1}^{N}\mu_{ij} < N, i = 1, 2, ..., c \end{cases} \tag{4.6}$$

With the application of Lagrangian multiplier technique, the membership function can be calculated as follows.

$$\mu_{ij}^{t} = \frac{1}{\sum_{k=1}^{c}(\frac{d_{ij}}{d_{kj}})^{\frac{2}{m-1}}} \tag{4.7}$$

where t presents the number of iteration. The new cluster center can be calculated as

$$P_i^{(t+1)} = \frac{\sum_{j=1}^{N}(\mu_{ij}^{(t)})^m x_j}{\sum_{j=1}^{N}(\mu_{ij}^{(t)})^m} \tag{4.8}$$

The centres of each cluster can be considered as the representatives of the measurement samples of each cluster. Therefore, the relationship between the temperature variation and wavelength shift can be extracted via modelling the relationship between the cluster centres. Various number of clustering centres were applied in this study, the results show that the minimum residual can be obtained when the number of cluster centres is 5. The clustering centres obtained by FCM are illustrated as the red triangles in Fig. 4.3, and the best fit line is presented as the solid line in red. For each cluster center, its projection on the y-axis represents the wavelength shift $\Delta\lambda_B$ caused by the corresponding temperature variation ΔT on the x-axis. Therefore, the relationship between ΔT and $\Delta\lambda_B$ can be modelled as

$$f(\Delta T) = 0.0243\Delta T + 8.357 \tag{4.9}$$

Since $f(\Delta T)$ only considers the temperature effect on the wavelength shift which is also affected by the other factors, such as strain and some unknown factors, which can be lumped as the model residual, Z. Therefore, the term Z needs to be modelled for the system compensation.

4.3.3 Modelling of Z

Since the dimensional change of the cell is the main reason causing the shell strain variation, it can be speculated that Z is associated to the factors which lead to cell dimensional change. In addition to temperature effects, the dimensional change of a lithium-ion battery may be caused by the following factors, such as the electrode expansion and contraction due to lithium intercalation and deintercalation, electrode volume change due to the irreversible reaction deposits, and the dead volume and pressure changes depending on the cell structure and construction [169].

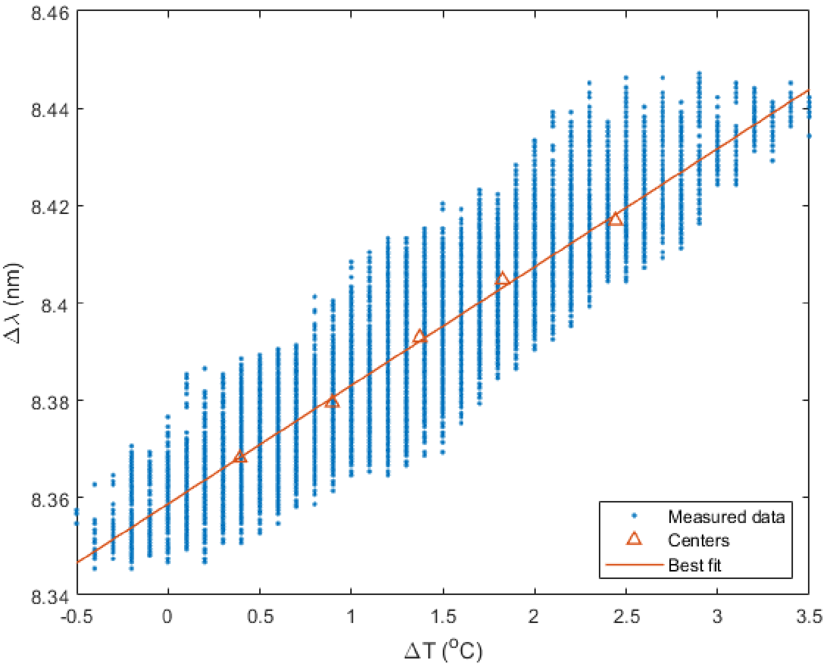

Figure 4.3: Relationship between ΔT and $\Delta\lambda_B$

In this study, the cell structure and construction are fixed, only the reversible electrode expansion and contraction due to lithium intercalation/deintercalation and irreversible electrode volume change are considered as the main reasons of the dimensional change of the cell. Therefore, Z can be considered as the combination of the short time scale effect and the long time scale effect. From the short time scale point of view, the structure and volume of the electrode change in each cycle due to the intercalation/deintercalation of lithium ions into/from the active materials of the electrode [145]. The expansion and contraction of the electrodes lead to the strain variation of the cell shell. The research in [145; 146; 147; 149] also confirmed that the change of SOC contributes to the strain variation of the electrodes of the lithium-ion batteries.

From the long time scale point of view, the intercalation and deintercalation of lithium ions induces mechanical stress to the graphite lattice, this causes the crack and expansion of the electrode [170]. The irreversible volume change of the electrode due to the cycle ageing leads to the strain change of cell shell. The experiment results in [149] also indicated that the maximum strain of the electrode decreases with the increasing of the cycle number.

Moreover, since Z is obtained by extracting $f(\Delta T)$ from $\Delta\lambda_B$, the measurement noise of ΔT from the thermocouple and the measurement noise of $\Delta\lambda_B$ from the FBG sensor are introduced. Therefore, in order to further analyse Z, it should be decomposed into three groups, named Z_n, Z_s and Z_c, i.e. $Z = Z_n + Z_s + Z_c$. Z_n implies the measurement noise in Z, Z_s and Z_c imply the influence due to the change of cell SOC and the influence related to the cycle number respectively. Empirical mode decomposition (EMD) technique is used in this study to decompose Z. EMD is an adaptive time-space analysis method proposed by Huang et al. [171] for non-stationary and non-linear signals. EMD breaks down the data Z into a number of n components, namely intrinsic mode functions (IMFs) and a residuum, namely r without leaving the time domain. The decomposed IMFs need to obey the following two properties:

- An IMF has only one extremum between two subsequent zero crossings, which means that the difference between the number of local maxima and minima is less than or equal to 1.
- The mean value of an IMF is zero.

Therefore, the data Z can be expressed as

$$Z = \sum_{i=1}^{n} h_i + r \tag{4.10}$$

where h_i represents the i^{th} IMF and r is the residuum of the decomposition. The implementation of the EMD algorithm can be summarised into following steps [172]:

- Step 0: Initialisation: Set i =1, n =1, $r_0 = Z$.
- Step 1: Set $k = 1$, $h_{i,0} = r_{n-1}$.
- Step 2: Identify all local maxima and minima of $h_{i,k-1}$.
- Step 3: Construct the upper envelope, namely $U_{i,k-1}$ and the lower envelope, namely $L_{i,k-1}$ via the cubic splines interpolation.
- Step 4: Determine the mean, namely $m_{i,k-1}$ of $U_{i,k-1}$ and $L_{i,k-1}$. $m_{i,k-1} = \frac{1}{2}(U_{i,k-1}$ - $L_{i,k-1})$.
- Step 5: Calculate the i^{th} IMF after k^{th} iteration: $h_{i,k} = h_{i,k-1}$ - $m_{i,k-1}$.
    1. if $h_{i,k}$ not satisfies the IMF criteria, increase k as $k = k + 1$ and repeat Step 2 to 5.
    2. if $h_{i,k}$ satisfies the IMF criteria, then set $h_i = h_{i,k}$ and $r_i = r_{i-1}$ - h_i.
- Step 6: If r_i represents a residuum, set $r = r_i$ and stop the process. If not, increase i as $i = i + 1$ and repeat Step 1 to 6.

The flow chart of EMD algorithm is shown in Fig. 4.4, and the extracted IMFs from Z are shown in Fig. 4.5.

4.3.3.1 Modelling of Z_n

Among the decomposed modes, the irrelevant modes are used to represent Z_n and the relevant modes are utilised to represent Z_s and the residuum is used to represent Z_c. The correlation coefficient (CORR) based EMD de-noising method [173] is applied to select the irrelevant modes in this study for the calculation of Z_n. Defines m is the indicator when the correlation coefficient between Z and $(Z - Z_n)$ starts to decrease sharply, Z_n is thus can be expressed as

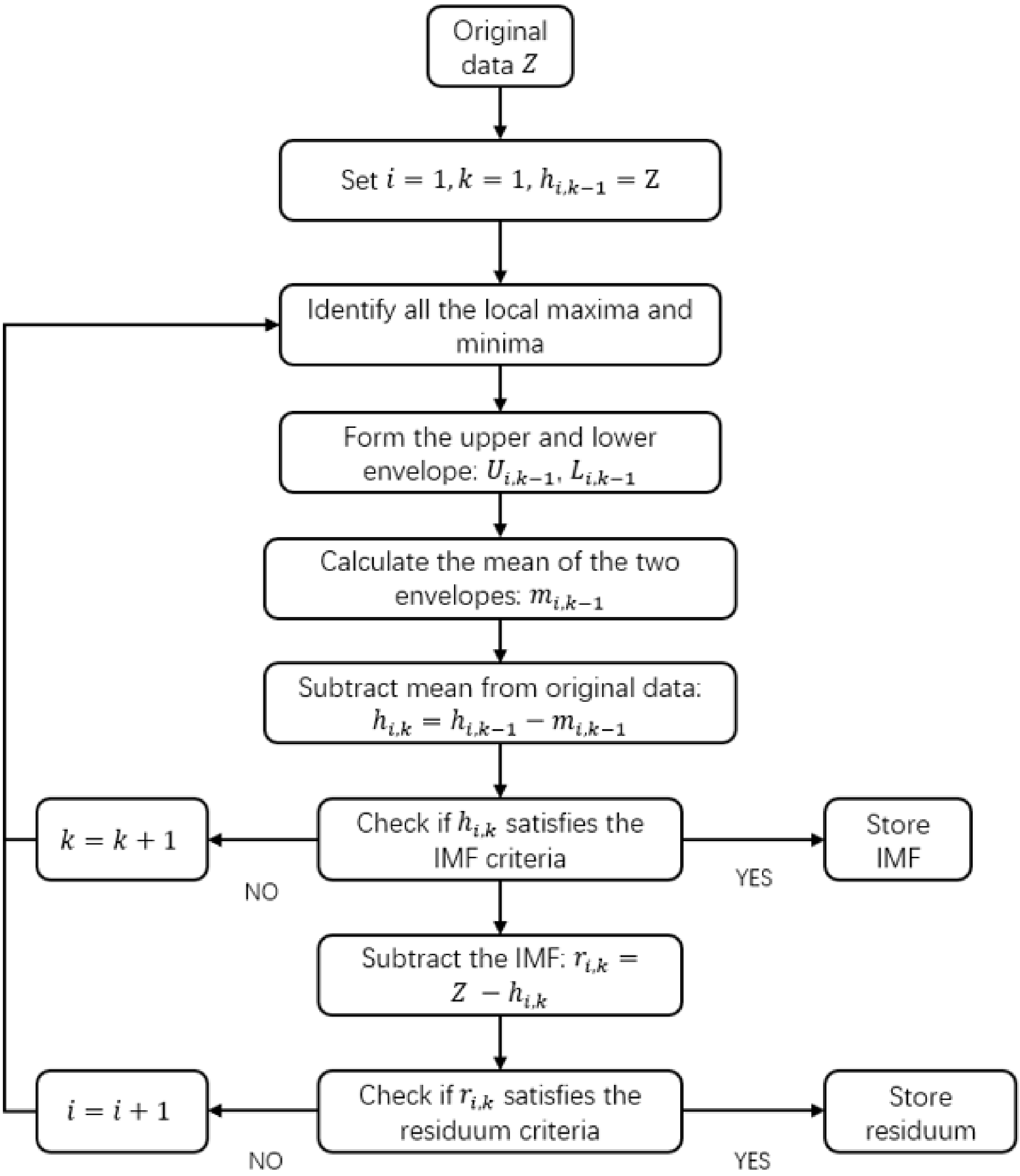

Figure 4.4: The flow chart of EMD algorithm

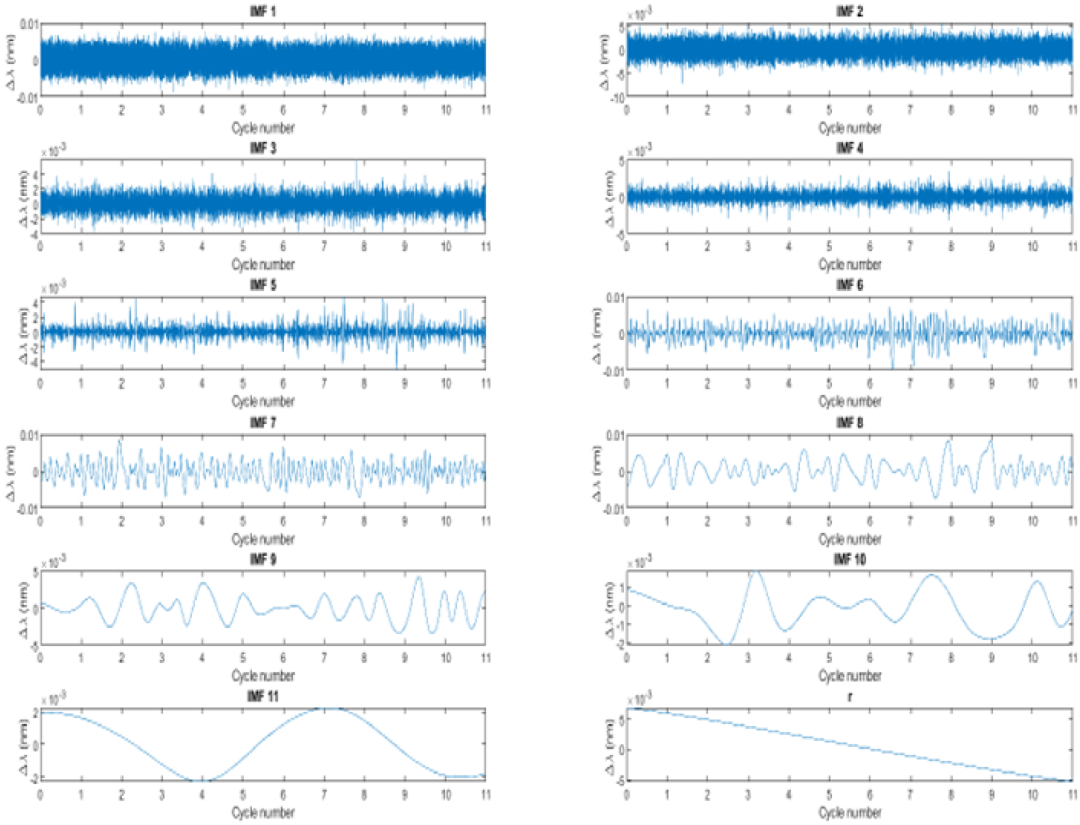

Figure 4.5: The decomposed modes and residual

$$Z_n = \sum_{i=1}^{m} h_i \tag{4.11}$$

The correlation coefficients between Z and $(Z - Z_n)$ obtained with different values of m is presented in Fig. 4.6. It can be seen that when m is greater than 5, the correlation coefficient between Z and $(Z - Z_n)$ decreases significantly. Therefore, m is set to 5 in this study.

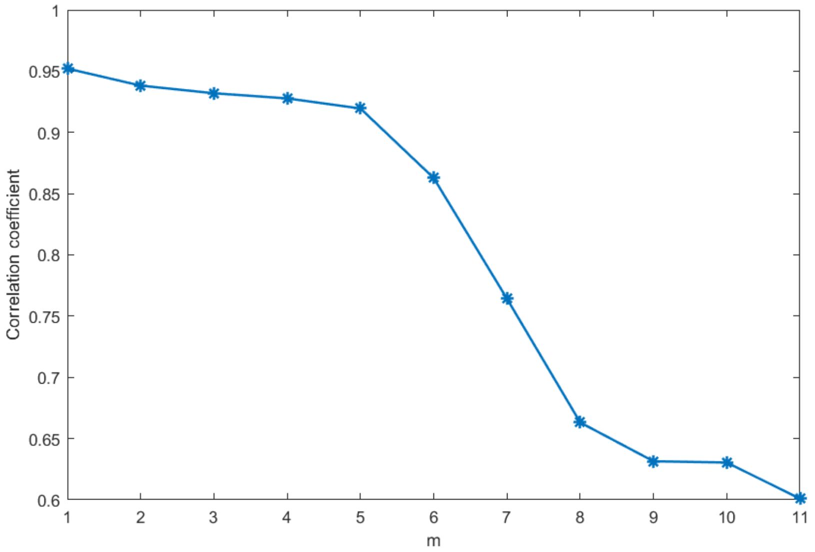

Figure 4.6: Correlation curve versus various the selection of m

4.3.3.2 Modelling of Z_s

In order to obtain the relationship between cell SOC and Z_s, coulomb counting method is applied in this study to calculate the SOC value of the cell in both charging and discharging processes. The distribution of Z_s on each SOC point is presented in Fig. 4.7. There is a clear difference between the distributions of Z_s in the charging and discharging processes. Polynomial fitting technique is then applied to fit the relationships between the cell SOC and Z_s in the charging and discharging processes, named Z_{ch} and Z_{dis} respectively. Therefore, Z_s can be expressed as

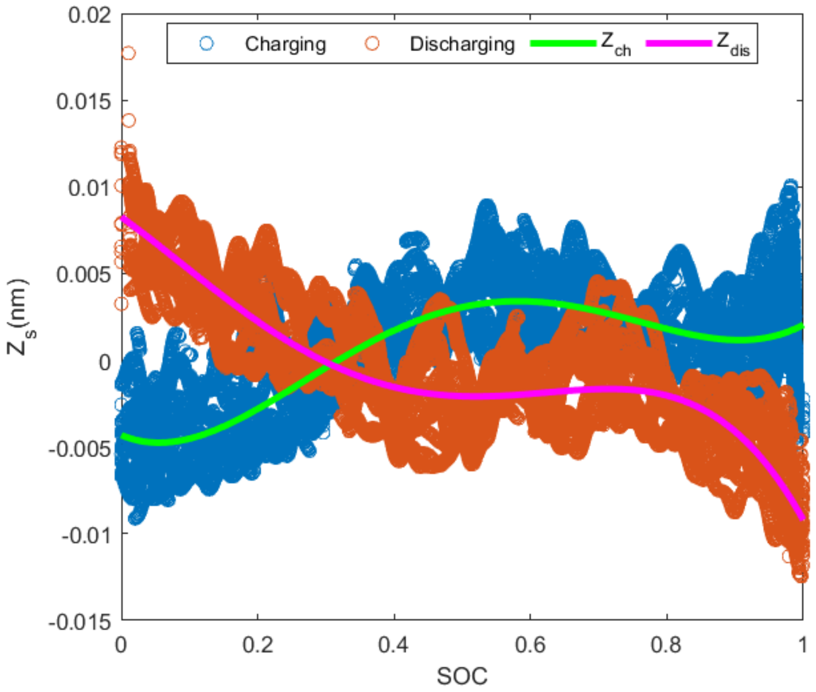

Figure 4.7: The distribution of Z_s on SOC

$$Z_s(t) = \begin{cases} Z_{ch}(t), & I \geq 0 \\ Z_{dis}(t), & I < 0 \end{cases} \tag{4.12}$$

where I represents the current through the cell at time t. $Z_{ch}(t)$ and $Z_{dis}(t)$ can be expressed as

$$\begin{cases} Z_{ch}(t) = p_1 s^4 + p_2 s^3 + p_3 s^2 + p_4 s + p_5 \\ Z_{dis}(t) = q_1 s^4 + q_2 s^3 + q_3 s^2 + q_4 s + q_5 \end{cases} \tag{4.13}$$

where s represents the SOC value of the cell at time t, p_1 to p_5, and q_1 to q_5 are the fitting coefficients of Z_{ch} and Z_{dis} respectively. The fitting coefficients can be identified by using the least squares (LS) method and the identification results are represent in Table 4.1.

Table 4.1: The identified fitting coefficients for Z_{ch} and Z_{dis}

Coefficient	p_1	p_2	p_3	p_4	p_5
Value	0.1425	-0.2932	0.1737	-0.0166	-0.0043
Coefficient	q_1	q_2	q_3	q_4	q_5
Value	-0.1110	0.1573	-0.0353	-0.0285	0.0083

4.3.3.3 Modelling of Z_c

Since the residual of EMD is the trend of the original signal, Z_c thus can be used to describe the relationship between Z and the cell cycle number c. The distribution of the EMD residual r is shown in Fig. 4.8, it can be seen that r presents an almost linear downward trend with the increase of the cycle number. Therefore, Z_c can be expressed as a linear function of cycle number c.

$$Z_c = -0.0011c + 0.007 \tag{4.14}$$

Finally, the temperature estimated via the FBG sensor, namely T_{FBG} can be expressed as

$$T_{FBG} = T_0 + f^{-1}((\lambda - \lambda_0) - (Z_s + Z_c)) \tag{4.15}$$

where T_0 is the base temperature which is set as 25 $^\circ C$ in this study. λ and λ_0 represent the measured peak wavelength and the characteristic wavelength of the FBG sensor.

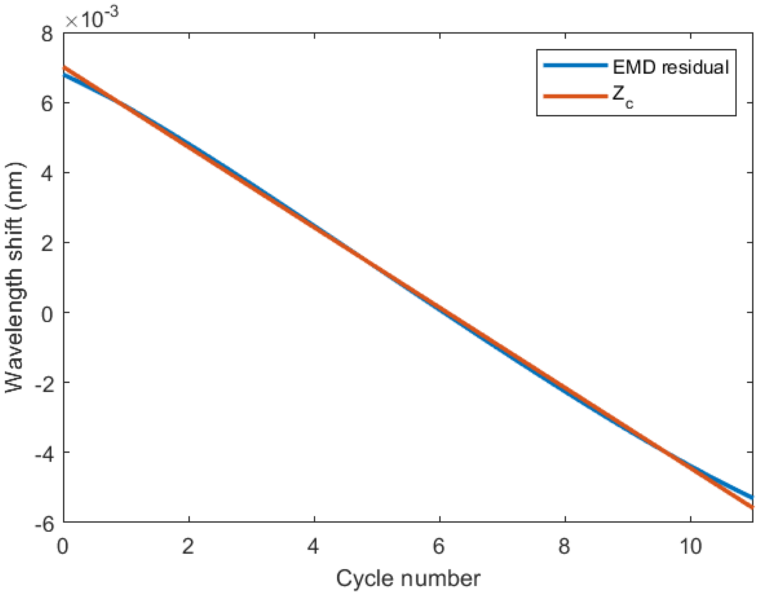

Figure 4.8: The distribution of EMD residual verses cycle number

4.4 Results and discussions

In order to verify the accuracy and reliability of the proposed temperature calibration method, the data of another 11 cycles (the 12^{th} to the 22^{nd} cycle) is used for the validation. The reference temperature value is measured by the thermocouple. Coulomb counting method is used to calculate the SOC of the cell. Therefore, Z_s and Z_c can be obtained according to Eq. (4.13) and (4.14). The temperature estimated via the FBG sensor can be calculated according to Eq. (4.15)

The temperature estimated via FBG 1 is presented in Fig. 4.9 (a). It is clear that the estimated temperature has a good agreement with the temperature measured by the thermocouple. The validation error of the estimated temperature is shown in Fig. 4.9 (b). It can be seen that most of the errors are distributed within $\pm$ 1 $°C$. The validation result also shows that the larger errors occur at high and low SOC levels in each cycle. This is due to the fact the electrochemical reactions inside the cell becomes unstable in very high and low SOC levels, the influence of the strain variations in these SOC levels are difficult to capture.

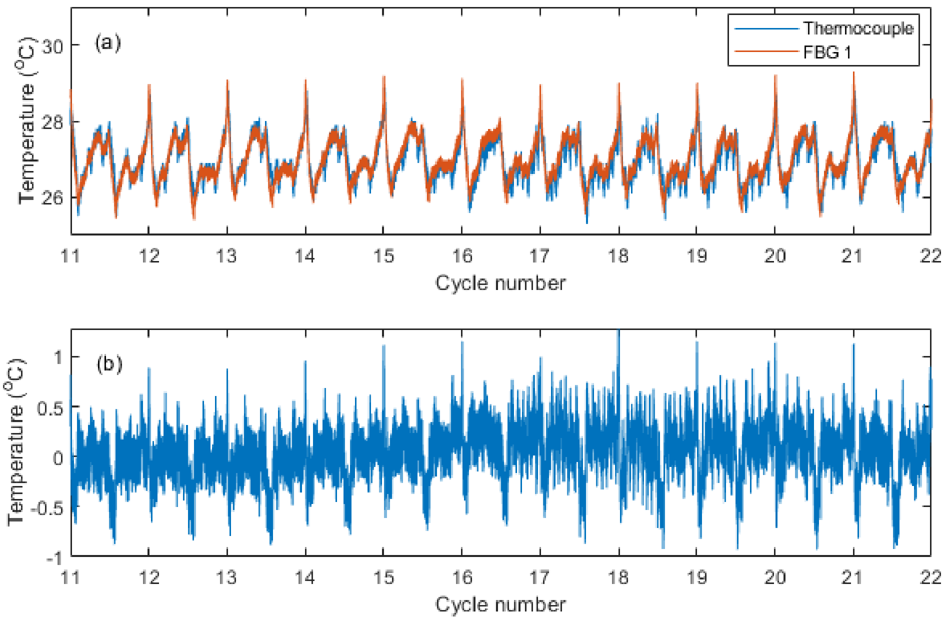

Figure 4.9: Temperature validation result of FBG 1

The temperature estimation results via FBG 2 and FBG 3 are also performed in this study using the same approach developed in Section 3. The data collected in Cycles 1 to 11 is used for modelling and the data obtained in Cycles 12 to 22 is used for validation. The temperature validation results of FBG 2 and FBG 3 are shown in Fig. 4.10 and Fig. 4.11, respectively. It can be seen that the temperature estimations obtained via FBG 1, FBG 2 and FBG 3 are highly consistent with the temperature data measured via the thermocouple. The numerical validation results in terms of mean error (ME), mean absolute error (MAE), maximum absolute error (MaXAE) and root mean square error (RMSE) are summarised in Table 4.2. The validation result shows that the developed method can accurately estimate the battery shell temperature via the peak wavelength data obtained from the FBG sensors.

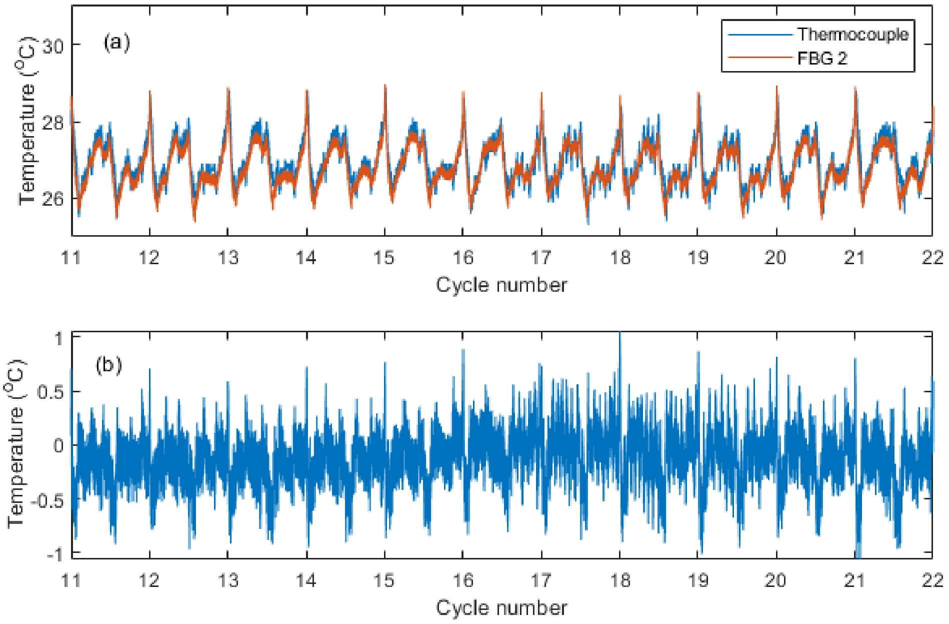

Figure 4.10: Temperature validation result of FBG 2

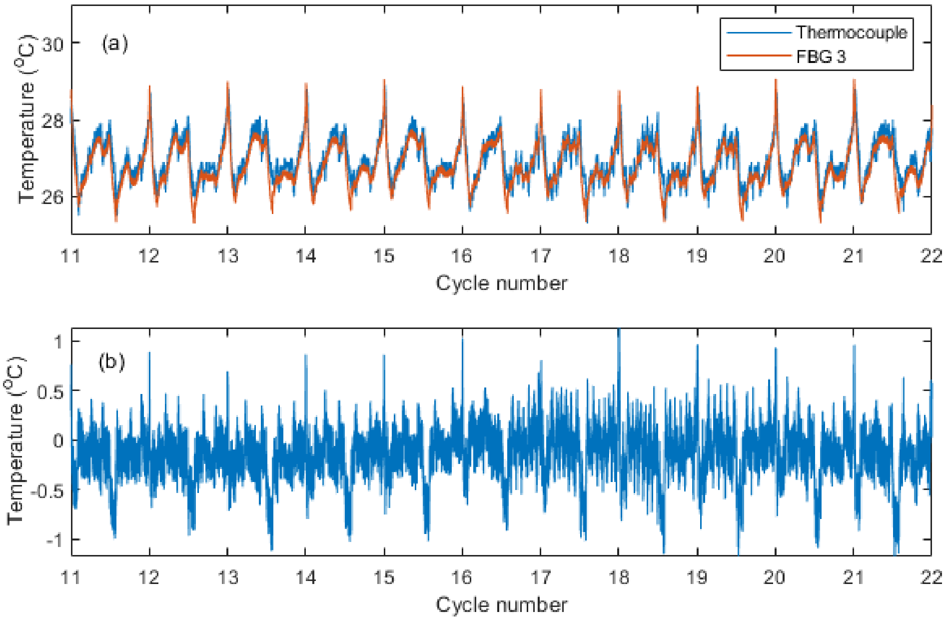

Figure 4.11: Temperature validation result of FBG 3

Table 4.2: The results of temperature validation

	ME ($^{\circ}C$)	MAE ($^{\circ}C$)	MaxAE ($^{\circ}C$)	RMSE ($^{\circ}C$)
FBG 1	-0.0401	0.2000	1.2790	0.2595
FBG 2	0.0516	0.1907	1.1465	0.2476
FBG 3	-0.0717	0.1950	1.2167	0.2645
Average	-0.0201	0.1952	1.2141	0.2572

4.5 Chapter summary

As ESSs are increasingly utilised in different fields, how to effectively and economically monitor the temperature of the ESSs has become a concern. Due to the merits of small size, mechanical robustness, resistance to corrosion and immunity to electromagnetic interference, FBG sensing technique has received more attention for temperature monitoring. Conventional FBG sensor calibration methods require high-standard experimental facilities and the whole process consumes a lot of time. Moreover, the conventional calibration process of the FBG sensors can only be performed offline, which means that it is not suitable for the FBG sensors that are already in use. In order to overcome the shortcomings of the conventional calibration method, a data-driven based FBG sensor temperature calibration method is developed in this chapter. The developed method can perform FBG temperature calibration online, which will not interrupt the normal operation of the ESSs. Moreover, the proposed method does not require high-standard experimental equipment or laboratory environment, which makes it more friendly for engineering applications. According to the validation results obtained from the tested three FBG sensors, the average results in terms of ME, MAE, MaxAE and RMSE are -0.0201 $^{\circ}C$, 0.1952 $^{\circ}C$, 1.2141 $^{\circ}C$ and 0.2572 $^{\circ}C$, respectively. The validation result confirms that the developed method has accurate and reliable performance in temperature monitoring for the ESS applications.

Chapter 5

Battery SOC Estimation

As a crucial function of the BMS, the battery SOC estimation needs to be accurate and reliable to ensure that batteries can be operated safely and efficiently. Accurate SOC estimation also helps with balancing, charging/discharging control and the remaining life prediction. Despite its importance, accurate SOC estimation is difficult to acquire in real-time since it is an implicit state of battery which cannot be measured directly and accurately. Therefore, many approaches have been developed for battery SOC estimation and almost all of them are based on the measurable electrical signals, such as the battery terminal voltage and current. However, the measurements of current and voltage are usually corrupted by noise. As one of the main sources of SOC estimation errors, sensor noise significantly affects the accuracy and reliability of SOC estimation [174; 175]. Moreover, the practicality of electrical measurements is also limited, such as the issues of insulation, corrosion and electromagnetic compatibility, etc. To address these problems, one of the cutting-edge solutions is to use fiber optical strain sensors to replace all or part of the traditional electrical sensors, the battery SOC therefore can be estimated based on the measurement of the strain information.

5.1 SOC estimation based on fiber sensors

Fiber optic sensing techniques have attracted a lot of attention in recent years due to the merits of lightweight, mechanical robustness, insulation in nature, resistance to corrosion, immune to electromagnetic radiation and easy to multiplex [143]. As one of the most popular type of fiber optic sensors, Fiber Bragg gratings (FBGs) have been utilised for internal and external temperature monitoring of batteries [140; 144; 166; 176], leading to more accurate thermal modeling for early prevention of thermal runaway. It is widely recognised that the lithiation/delithiation processes inside a lithium-ion battery are associated with structural and volume changes of the electrode, which consequently causes strain variation of the battery. Therefore, FBGs are also proposed for strain monitoring [146; 147; 177] in order to evaluate the stability and safety of the batteries.

The utilisation of optical fiber sensing technology in BMS is still in the preliminary research stage, a few techniques have been developed for SOC estimation based on FBG sensors. In [149], the FBG sensors are embedded inside the battery to monitor the strain variations of the electrode during charging and discharging process. Extended Kalman filter (EKF) is implemented for SOC estimation based on an empirically developed strain prediction model. However, embedding the sensors inside the battery may cause the degradation of battery capacity and cycle life [148]. It is also difficult to flexibly install or uninstall the FBG sensors into or from the batteries that have been in use. Moreover, as the most basic extension of the Kalman filter, EKF linearises the system under investigation around the current system state as a first-order approximating estimator. Consequentially, if the system is highly nonlinear, the EKF may diverge.

Recently, a machine learning based SOC estimation approach is reported in [150]. The strain data were obtained from a FBG based sensor network which is mounted on the surface of the batteries. The dynamic time warping (DTW) approach is employed to determine the ‘distance’ between the measured strain curve and the reference strain curve. K-nearest neighbours (KNN) algorithm is then applied as a classifier to estimate the battery SOC. However, when establishing the sample set, the number of cycles chosen is a crucial parameter that needs to be set carefully. If the number of cycles chosen is too large, this approach will not able to deal with random fluctuations. If it is too high, the computational cost will increase considerably, making this approach impractical. Furthermore, due to the limitations of the DTW algorithm, this approach may generate large estimation errors at the regions where the strain curves are less identifiable.

In order to overcome the drawbacks of the above approaches, a strain based SOC estimator is developed in this chapter. Firstly, the FBG strain sensors are implemented on the surface of the batteries to collect the strain data during the charging and discharging processes. Three FBG sensors are mounted on the cell, and three sets of strain data, namely S1, S2 and S3 can be measured. Compared with the embedded sensing layout, this non-embedded layout will not cause any damage to the cells, and can be flexibly installed or uninstalled when necessary. Secondly, a back-propagation (BP) neural network (NN) model is developed to predict the difference between S1 and S3. Finally, a strain based SOC estimator is developed with the utilisation of Unscented Kalman Filter (UKF). The developed BP model is used to predict the strain information and the system state (SOC) is updated by Coulomb counting method. The developed strain based SOC estimator can estimate battery SOC accurately without any battery voltage measurement. To enhance the accuracy of the strain based SOC estimator, an enhanced strain based SOC estimator is then developed with the adoption of both strain and voltage information. The test results indicate that the enhanced strain based SOC estimator achieves more accurate SOC estimation than the strain based SOC estimator and the voltage based SOC estimator.

5.2 Sensor design and experimental setup

Four cylindrical $LiFePO_4$ cells were used in this work, the nominal voltage and capacity of these cells are 3.2 V and 1.6 Ah, respectively. For each cell, three FBG sensors were glued onto the cell surface with a slightly different orientation to each other. In order to minimise the changes to the original packaging of the cells, the sensors were attached to the original package of the cells. Therefore, the inclusion of the sensor system will not cause any damage to the battery. The layout of the FBG-based sensors is shown in Fig. 5.1. The FBGs were manufactured using the phase mask method. For each cell, all the sensors were pre-strained before they were attached, the characteristic wavelengths of the sensors were 1534 nm, 1539 nm and 1544 nm, respectively. Micron-Optics SM-130 interrogator was used to measure the wavelength shifts of the FBGs at 1 kHz during the experiment.

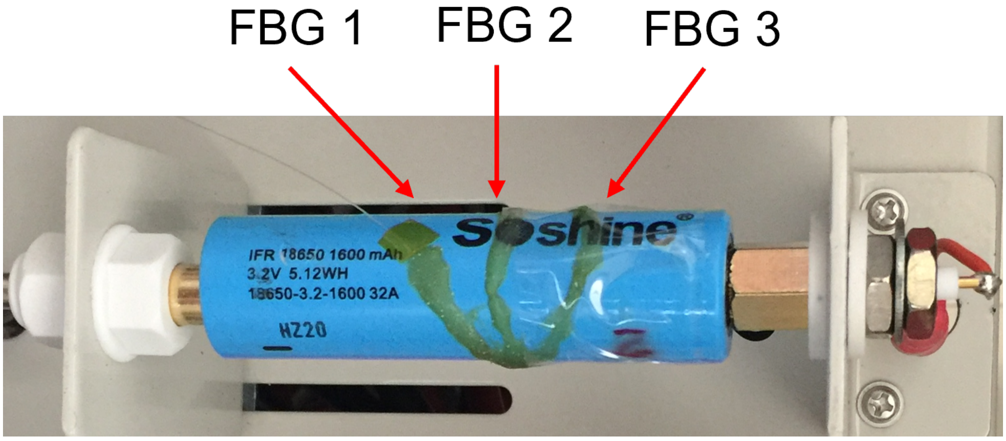

Figure 5.1: The layout of the FBG-based strain sensors

Since the FBG sensors are installed at a known angle to each other, the method described in [164] is used in this work for temperature discrimination. The radial strain ($\epsilon_{i,j}$) can be calculated as:

$$\epsilon_{i,j} = \frac{\Delta\lambda_i/\lambda_i - \Delta\lambda_j/\lambda_j}{(1-p_e) - (1-cos(\theta)^2)} \tag{5.1}$$

where p_e is the photo-elastic coefficient of silica, λ_i and λ_j are the Bragg wavelengths for each sensor and θ the angle between them. Therefore, three sets of strain measurements, namely S1, S2 and S3 can be obtained for each cell. The resulting calibrations were performed in a stable chamber, co-located thermocouples and strain gauges are utilised to provide a reference.

In order to provide an effective comparison of the performance of the developed system for SOC estimation, a CCCV profile was applied for the charging processes and a CC profile was applied to the discharging processes. NEWARE BTS4000 battery tester was employed to control the current and voltage during the charging/discharging processes. The upper and lower cut-off voltages during the cycling were set as 3.6 V and 2 V respectively, and the current rate in both charging and discharging processes was set as 1C. A thermal couple was mounted on each cell for the temperature measurement. The SOC value is calculated by the Coulombic counting method as a reference and then is associated with the corresponding strain data.

The correlation between the measured strain (S1) and the current profile is presented in Fig. 5.2. It can be seen that the patterns of the strain data were very reproducible in each cycle although their magnitudes are different in some regions due to the random fluctuations.

5.3 Modelling

In this section, a strain information based neural network (NN) model is developed to describe the relationship between the SOC and the measured strain information. To evaluate the performance of the developed NN model in SOC estimation, a

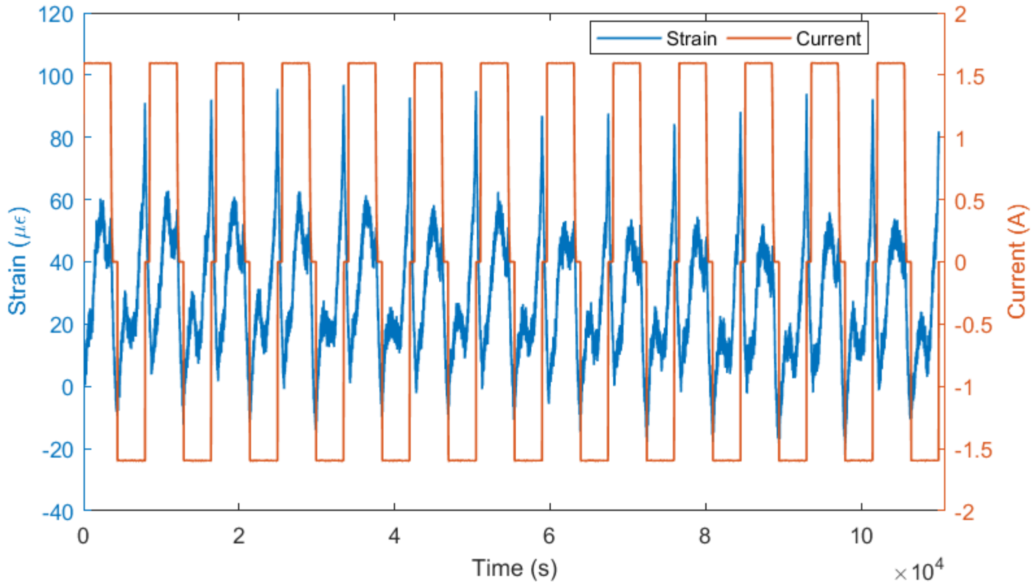

Figure 5.2: Illustration of the current profile along with the strain response

voltage information based empirical model is also established in this section. Both of the strain based NN model and the voltage based empirical model will be used for SOC estimation as a comparison.

5.3.1 The strain based NN model

The NN based battery models can describe the battery behaviour without priori knowledge about the underlying electrochemical process occurring inside the battery. Regarding SOC estimation, the NN based battery model is generally used to describe the relationship between the SOC and other measurable signals, such as the battery terminal voltage, current and temperature [178; 179; 180; 181]. As mentioned before, the practicality of electrical measurements is limited by the environment. In order to overcome this problem, a Backpropagation (BP) based NN model is developed to describe the relationship between the SOC and the measured strain information.

5.3.1.1 Back-propagation neural network

BP is a widely used supervised learning algorithm due to the advantages in terms of fast, simple and easy to program. The schematic diagram of a BP-NN structure is shown in Fig. 5.3. Assume that there are n inputs (u_1, u_2, ... u_n) and m outputs (y_1, y_2, ... y_m) in the network, and network consists of an input layer, one or more hidden layers (only one shown in the figure) and an output layer. The number of neurons in the input layer, hidden layer and output layer are n, L and m, respectively.

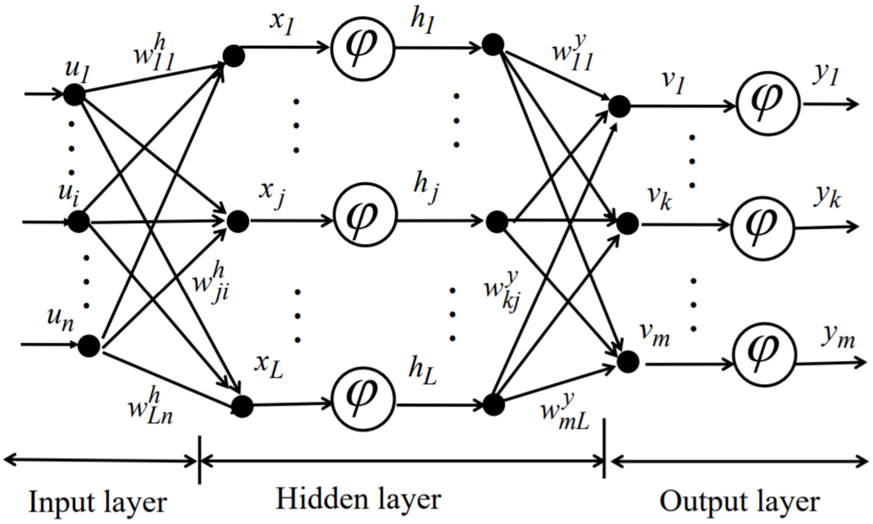

Figure 5.3: The schematic diagram of BPNN structure

There are two phases in a BPNN, the forward pass phase and backward pass phase. In the forward pass phase, feedforward propagation of input pattern signals through the network and the 'functional signal' is computed. The weights in the network are initialised and fixed during forward pass at time t. Thus, the input and output of the hidden node can be computed as

$$\begin{cases} x_j(t) = \sum \omega_{ji}^h(t)u_i(t)), \quad i = 1, 2, ...n, j = 1, 2, ...L. & (5.2) \\ h_j(t) = \varphi(x_j(t)) \quad j = 1, 2, ..L. & (5.3) \end{cases}$$

where $x_j(t)$ and $h_j(t)$ are the input and output of the hidden node at time t, respectively. The input and output of the output node can be computed as

$$\begin{cases} v_k(t) = \sum \omega_{kj}^y(t)h_j(t)), \quad j = 1, 2, ...L, k = 1, 2, ...m. & (5.4) \\ y_k(t) = \varphi(v_k(t)) \quad k = 1, 2, ..m. & (5.5) \end{cases}$$

In the backward pass, the propagation error backwards through network starting at output units. The propagation error at time t can be computed as

$$E(t) = \frac{1}{2}(d(t) - y(t))^2 \tag{5.6}$$

where $E(t)$ denotes the propagation error at time t, $d(t)$ and $y(t)$ denote the desired and actual values of the output, respectively. In order to decrease E, the weights could be modified according to the Delta rule. Therefore, to achieve gradient descent in E, the weights should be modified as:

$$\begin{cases} \omega_{ij}^y(t+l) = \omega_{ij}^y(t) + \eta(t)\Delta_i(t)h_j(t) & (5.7) \\ \omega_{ij}^h(t+l) = \omega_{ij}^h(t) + \eta(t)\delta_i(t)u_j(t) & (5.8) \end{cases}$$

where

$$\begin{cases} \Delta_i(t) = -\dfrac{\partial E(t)}{\partial y_i(t)}\dfrac{\partial y_i(t)}{\partial v_i(t)} & (5.9) \\ \delta_i(t) = -\displaystyle\sum_{k=1}^{m}(\dfrac{\partial E(t)}{\partial y_k(t)}\dfrac{\partial y_k(t)}{\partial v_k(t)}\dfrac{\partial v_k(t)}{\partial h_i(t)})\dfrac{\partial h_i(t)}{\partial x_i(t)} & (5.10) \end{cases}$$

The forward pass phase and backward pass phase will be repeated to update the weights continuously until the training process is completed.

5.3.1.2 Selection of the model input and output

It is widely recognised that the intercalation of lithium-ions will cause the battery anode graphite structure to swell, which will affect the strain of the battery anode. Therefore, it can be inferred that SOC is a major factor which influences the value of strain. Due to the associated electrochemical complexity, the strain and SOC exhibit a highly non-linear relationship. The trajectories of measured S1, S2 and S3 on SOC dimension in the charging and discharging processes are shown in Fig. 5.4. It can be seen that in both of the charging and discharging processes, the main trajectory trends of S1, S2 and S3 are highly similar, and their corresponding peaks and valleys also appear in the same SOC regions. It is worth noting that for the same FBG sensors, the trajectories of the measured strain are significantly different during the charging process and discharging process, similar experimental results can also be found in [146]. The reason for this phenomenon is that the electrochemical reactions inside the battery during the charging and discharging are different, and the heat and tension generated inside the battery to be inconsistent in the charging and discharging. As a consequence, the relationships between the SOC and the measured strain are different in the charging and discharging processes. Therefore, it is more reasonable to model the relationship between the SOC and the measured strain in the charging process and the discharging processes respectively.

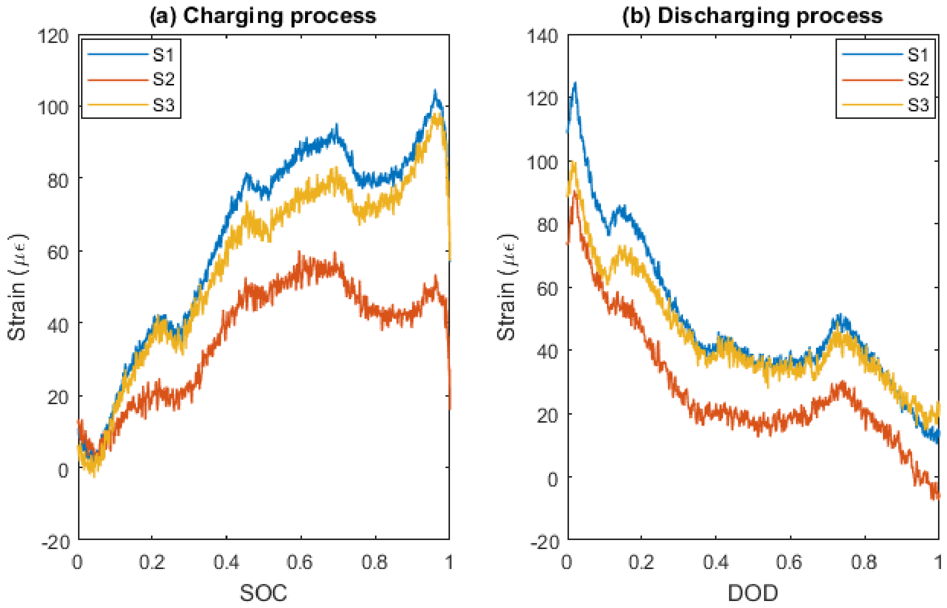

Figure 5.4: The relationship between SOC and the measured strain

Since a lithium-ion battery undergoes a series of electrochemical reactions during the operation, including both endothermic and exothermic reactions. The endothermic and exothermic reactions will cause the variations of battery internal and external temperature. The heat generated inside the battery will cause the internal materials of the battery to expand and resulting in pressure changes on the battery surface. In addition to the strain variation caused by SOC change, the strain variation may also be caused by the expansion and shrinking of internal materials. Therefore, in addition to SOC, the temperature is another factor that should be considered as an input of the model.

It also should be noted that the strain measurement values are also affected by some uncertainties, such as sudden changes in temperature, the interference from internal/external forces and random fluctuations, etc. For the same FBG strain sensors, the measured strain trajectories in different cycles may not overlap with each other, as shown in Fig. 5.5 (a) to (f). This means that the strain values measured at the same SOC levels but in different cycles may vary due to the influence of the uncertainties. Therefore, it will be difficult to guarantee the accuracy and reliability of the model if the measured strain data are used for modelling directly.

Since these uncertain factors usually act on all FBG sensors simultaneously, this implies that the three sets of measured strain data are affected by the same uncertain factors simultaneously. By analysing the data, it can be found that the difference between any two sets of strain information shows a nonlinear relationship in the SOC dimension, and this relationship remains almost the same in different cycles. Further analysis of the data shows that whether in the charging or discharging process, the difference between S1 and S3 maintains a very stable relationship with the SOC in different cycles, as shown in Fig. 5.5 (g) and (h). When the difference between S1 and S3, namely (S1 - S3), is used as the observation, the interference caused by the uncertainties will be cancelled and exhibit a more stable relationship with SOC.

Since SOC is an internal state of the battery which cannot be measured directly, it is not suitable to use its values as the observations of a estimator. On the other hand side, since both S1 and S3 can be measured in real time, the difference between S1 and S3 can be used as the observation in the estimation model to form a closed loop system. The real-time system feedback can be obtained by comparing the measurements and the predictions of the estimator. Therefore, SOC and temperature are selected as the BP-NN model inputs and (S1-S3) is selected as the BP-NN model output.

The flowchart of the strain based SOC estimator is present in Fig. 5.6, and its workflow can be summarised as the following steps:

- Step 0: System state (SOC) initialisation.

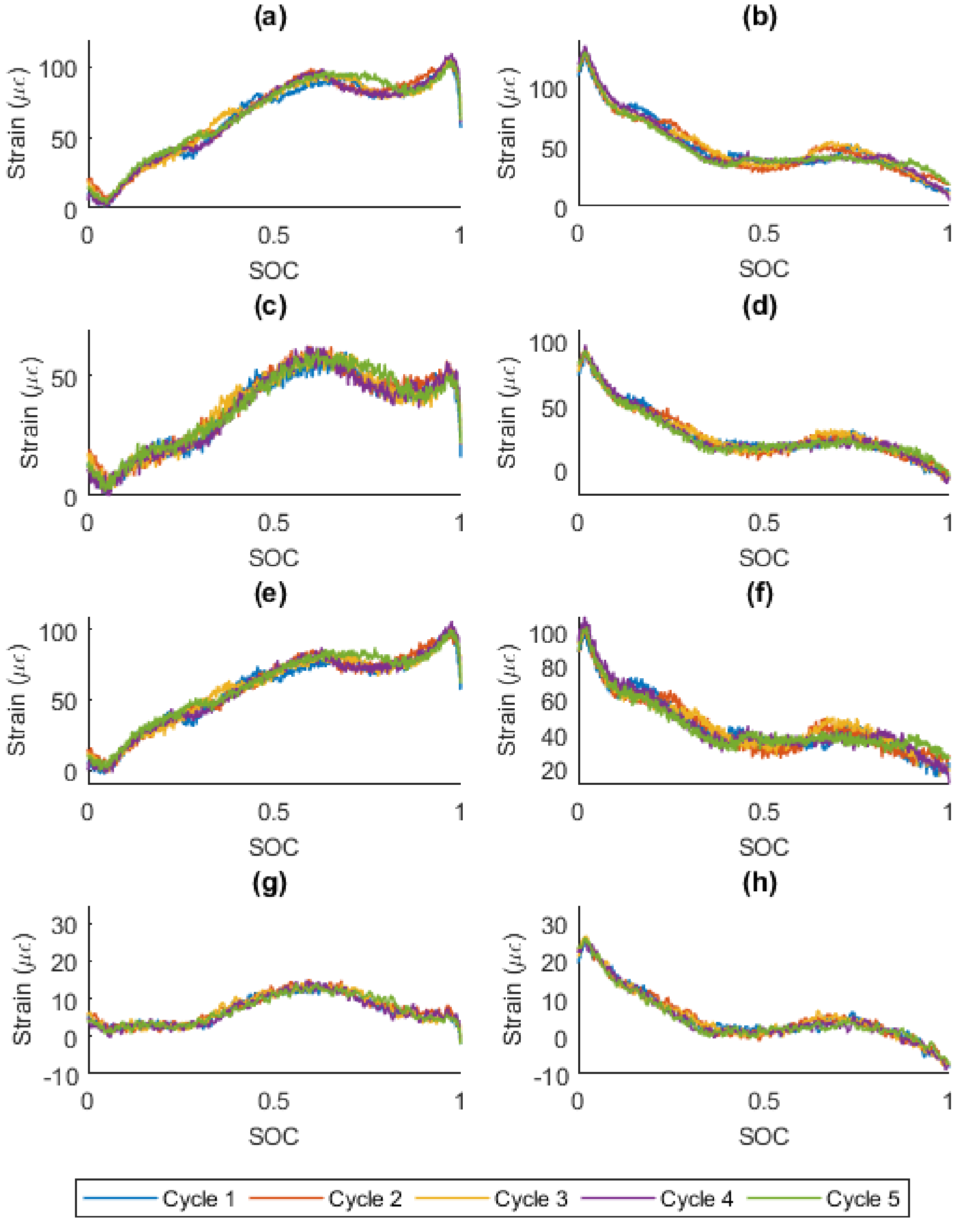

Figure 5.5: The measured strain trajectories in different cycles

- Step 1: Calculate the priori estimated SOC ($\hat{x}_k^-$) via the Ah model.
- Step 2: Predict the system output $\hat{y}_k$ via the BP-NN model.
- Step 3: Calculate the system residual e_k.
- Step 4: Calculate the system feedback gain via the Unscented Kalman filter (UKF).
- Step 5: Calculate the posteriori estimated SOC ($\hat{x}_k$) to update the system state.
- 6: Repeat Step 1 to 5 for the next time step.

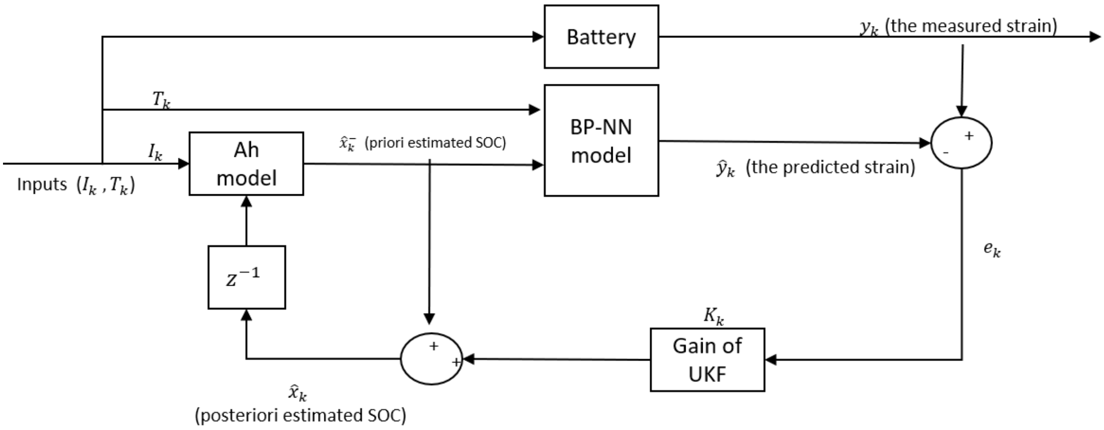

Figure 5.6: The flowchart of the developed strain based SOC estimator

5.3.1.3 Selection of model structure

The number of neurons and hidden layers are the two key factors to determine the structure of a BP-NN model. In order to minimise the complexity of the model, a single hidden layer structure is firstly used in this work. Only if a single hidden layer structure is incompetent, a multi hidden layer structure will be adopted.

Regarding the selection of neuron numbers, if too few neurons are used, the model may not able to detect the signals in a complicated data set, which is known as underfitting. On the other hand, if too many neurons are used, the limited amount of information contained in the training set will not be enough to train all of the neurons, which is known as overfitting. Even when the training data is sufficient, the time of training will be increased if too many neurons are used. However, there is no universal method to directly determine the most suitable number of neurons in the hidden layer yet. Cross-validation method is one of the most effective approaches used for verification of models in machine learning, especially for the cases that are difficult to create a large training data set. Therefore, a cross-validation method namely Leave One Cycle Out (LOCO) is used to determine the model structure in this work.

Firstly, the model structure is defined according to the number of neurons used in the hidden layer, and a model set M can be created. Since the relationship between model input and output in this work is relatively obvious, the optimal number of neurons is empirically assumed as a number that is less than 10. Therefore, it has $M = \{M_1,M_2,...,M_{10}\}$. The weights in M_i (i = 1,2 ..., 10) then can be obtained in the training process.

In the training process, the training data set D ($D = \{D_1$, D_2 ..., $D_5\}$) consists of a total of five cycles (Cycle 1 to 5) of data. For each training, the data set D will be divided into subsets, namely D_T and D_V. D_T consists of any four cycles of data and it is used to train the model M_i (i = 1, 2, ..., 10). D_V consists of the data of the rest cycles, D_j, j = 1, 2 ..., 5), which is used to validate the performance of model structure M_i. The validation result calculated in Mean Square Error (MSE) is recorded as R_{ji} for Model M_i. The average performance of model structure M_i, namely R_i can be calculated as the average value of the five validation results R_{ji}, j = 1, 2, ...5.

The average performance of different model structures are compared in Fig. 5.7. It can be seen that in the charging process, the model structure with 5 neurons in the hidden layer has the best average performance. When the number of neurons is greater than 5, increasing the number of neurons only has a slight impact on the evaluation performance. On the other hand side, the model structure with 6 neurons in the hidden layer has the best average performance for the discharging process.

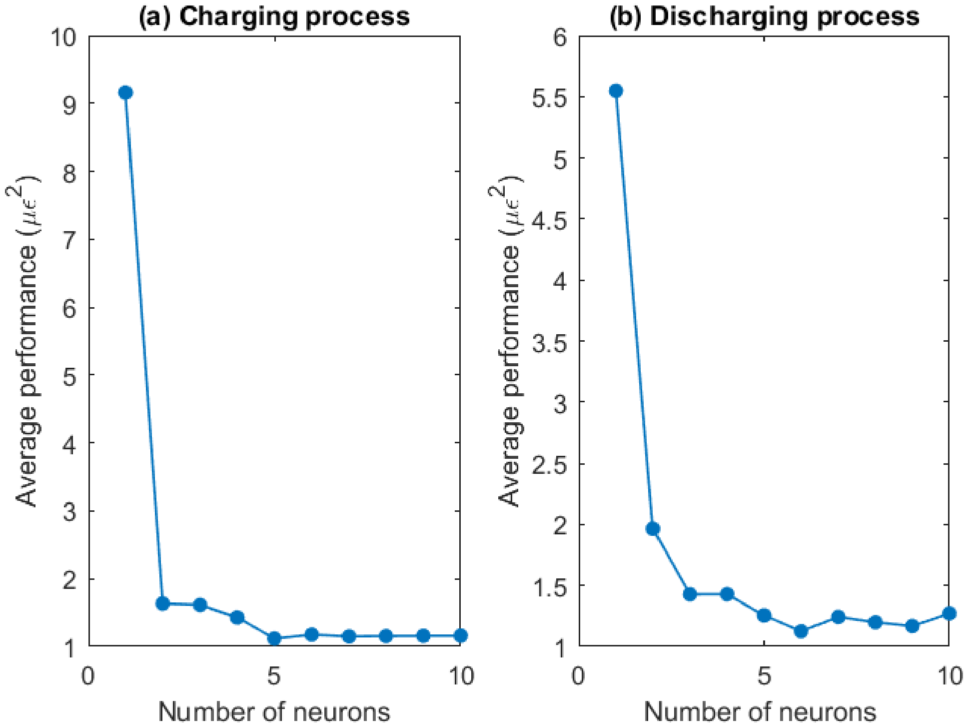

Figure 5.7: The average performance of different model structures

The same LOCO cross-validation method is also applied to multiple hidden layers cases. Since the increase in the number of hidden layers has not greatly improved the average validation performance, the model structures are therefore determined as a single hidden layer with 5 neurons for the charging process, and a single hidden layer with 6 neurons for the discharging process.

5.3.2 The voltage based empirical model

5.3.2.1 The combined model

With respect to battery modelling, empirical models utilise empirical equations to describe specific features of the battery electrical behaviour. Unlike the equivalent circuit models, empirical models usually do not require to take any specific tests, e.g. the OCV test and HPPC test, etc. Shepherd model [90], Unnewehr model [91] and Nernst model [92] are the most typical empirical models for lithium-ion batteries, the mathematical equations of the three empirical models are presented in Table 5.1, where V_t represents the battery terminal voltage, I represents the current, R_0 represents the battery internal resistance, K_0, K_1, K_2, K_3 and K_4 are constant coefficients to make the model fit the data. The accuracy of these three empirical models is compared in [182] and the results indicate that Nernst model achieves the best performance for terminal voltage prediction.

Table 5.1: Typical empirical models

Models	Mathematical equations
Shepherd model	$V_t = k_0 + R_0 I + k_1/SOC$
Unnewehr model	$V_t = k_0 + R_0 I + k_2\ SOC$
Nernst model	$V_t = k_0 + R_0 I + k_3\ ln(SOC) + k_4\ ln(1 - SOC)$

The shepherd model, Unnewehr model and Nernst model can also be combined in order to achieve more accurate performance [93; 94; 95], the mathematical equation of the combined model can be expressed as:

$$V_t = k_0 + R_0 I + k_1 SOC + k_2/SOC + k_3 ln(SOC) + k_4 ln(1 - SOC) \qquad (5.11)$$

In this section, the combined model is therefore selected as a typical example of the voltage information based empirical models.

5.3.2.2 Model parameter identification

The regression equation of the combined model can be expressed as:

$$\begin{cases} Y = \phi\theta & (5.12) \\ \phi = [1 \quad I \quad SOC \quad 1/SOC \quad ln(SOC) \quad ln(1 - SOC)] & (5.13) \\ \theta = [k_0 \quad R_0 \quad k_1 \quad k_2 \quad k_3 \quad k_4]^T & (5.14) \end{cases}$$

where Y presents the battery terminal voltage, ϕ and θ are the matrix of inputs and parameters, respectively. R_0 represents the battery internal resistance, I is the current through the battery. k_0, k_1, k_2, k_3 and k_4 are the coefficients to make the model fit the data. The same cross validation method used in Section 5.3.1.3 is also applied to choose the optimal parameters in the combined model. The model parameter identification results are shown in Table 5.2.

Table 5.2: Parameter identification results

k_0	R_0	k_1	k_2	k_3	k_4
3.7492	0.2267	-0.2747	-0.0002	0.1602	-0.0276

5.3.3 Model validation

In order to evaluate the accuracy of the model, both of the strain based NN model and the voltage based empirical model are tested with a new set of data obtained from Cycle 6. The validation results of the strain based NN model are presented in Fig. 5.8, and the prediction errors are shown in Fig. 5.9. In the charging process, the root mean square error (RMSE) and the maximum absolute error (MaxAE) are $0.9997\mu\epsilon$ and $3.8173\mu\epsilon$ respectively. In the discharging process, the RMSE and the MaxAE are $1.1457\mu\epsilon$ and $3.7713\mu\epsilon$, respectively.

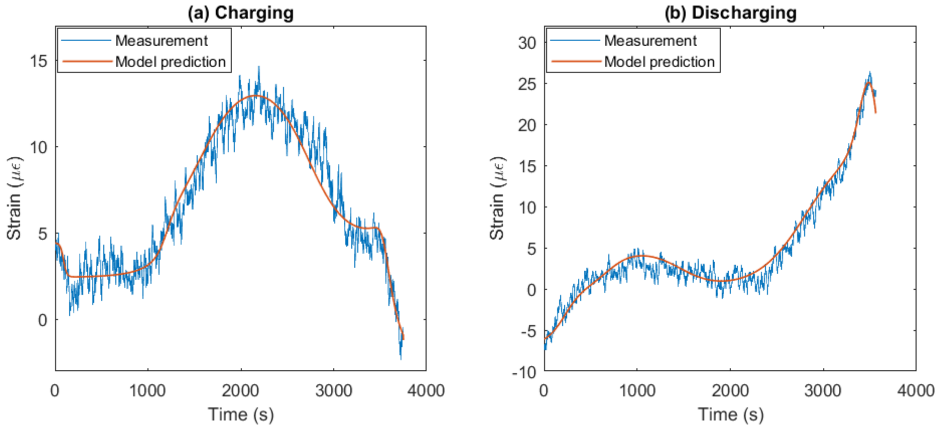

Figure 5.8: The validation results of the strain based NN model

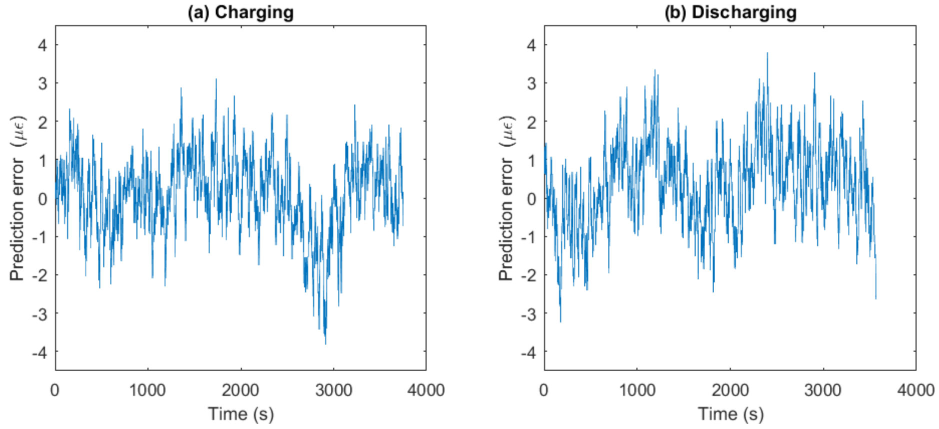

Figure 5.9: The prediction error of the strain based NN mode

The validation results of the voltage based empirical model are presented in Fig. 5.10 and the prediction errors are shown in Fig. 5.11. In the charging process, the RMSE and the MaxAE are $0.0099V$ and $0.0391V$ respectively. In the discharging process, the RMSE and MaxAE are $0.0125V$ and $0.043V$, respectively.

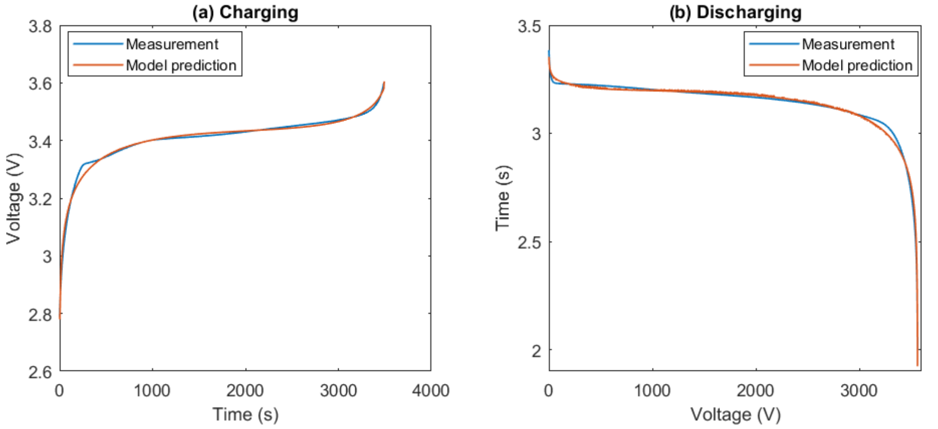

Figure 5.10: The validation results of the voltage based empirical model

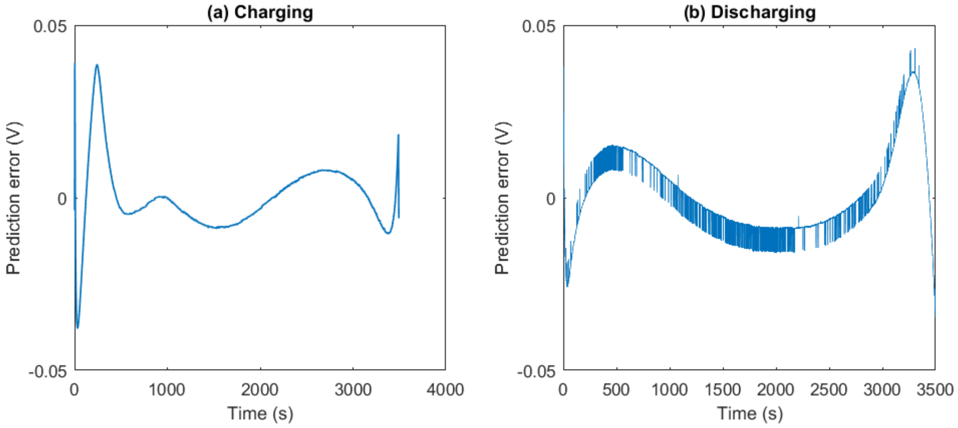

Figure 5.11: The prediction error of the voltage based empirical model

5.4 SOC estimation based on UKF

Although EKF is straightforward and easy to program, it has the following main drawbacks: firstly, EKF suffers from divergence issues due to the linearisation using first-order Taylor series. Secondly, costly calculations of Jacobian matrices are required in EKF. Last but not least, EKF requires the derivatives information of the state and measurement functions, which makes it difficult to be used for certain types of models. In order to overcome these drawbacks, Unscented Kalman filter (UKF) is proposed as an advanced method to solve the state estimation problems for non-linear systems. Compared with EKF, UKF shows better performance in terms of accuracy and stability [183; 184; 185]. Moreover, the derivatives of the state and measurement functions are not required in UKF, which is more suitable for the NN based models. Therefore, both of the strain based NN model and the voltage based empirical model can be easily merged into UKF for real-time SOC estimation.

5.4.1 Implementation of the UKF

The UKF belongs to the family of sigma-point filters and approximates the system using an unscented transformation (UT), which is a sampling technique to capture the mean and variance a minimal set of sigma points. The schematic diagram of the UT is shown in Fig. 5.12.

Considering a system represented by a nonlinear function $y = g(x)$, the mean and covariance of a set of Gaussian random variable x (dimension L) are defined as $\bar{x}$ and P_x, respectively. In order to capture the true mean and covariance of the prior random variable x, a set of sigma points, namely $\{\chi_i\}$ $(i = 0,\ 1,\ ...\ 2L)$ can be deterministically chosen via the following equation:

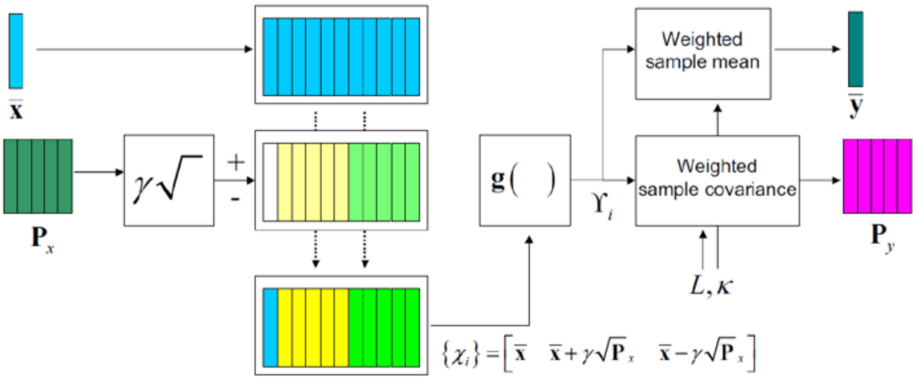

Figure 5.12: The schematic diagram of the UT [3]

$$\begin{cases} \chi^{[0]} = \bar{x} \\ \chi^{[i]} = \bar{x} + [\gamma\sqrt{P_x}]_i, i = 1, ..., n \\ \chi^{[i]} = \bar{x} - [\gamma\sqrt{P_x}]_i, i = n+1, ..., 2n \end{cases} \tag{5.15}$$

where $[...]_i$ represent the i^{th} column of $[...]$, γ is a composite scaling parameter which can be calculated as follows:

$$\begin{cases} \gamma = \sqrt{L + \lambda} \\ \lambda = \alpha^2(L + \epsilon) - L \end{cases} \tag{5.16}$$

where α is the scaling parameter that determines the distribution of the sigma points and ϵ is the parameter to adjust the spread of the sigma points. The smaller the α and ϵ are, the further the sigma points are close to the mean value.

The corresponding weights of the sigma points and the covariance can be determined by the following equations:

$$\begin{cases} \omega_x^{[0]} = \dfrac{\lambda}{L+\lambda} \\ \omega_x^{[i]} = \dfrac{1}{2(L+\lambda)}, i = 1, ..., 2n \\ \omega_p^{[0]} = \dfrac{\lambda}{L+\lambda} + (1 - \alpha^2 + \beta) \\ \omega_p^{[i]} = \dfrac{1}{2(L+\lambda)}, i = 1, ..., 2n \end{cases} \tag{5.17}$$

Finally, the mean and covariance of y, namely $\bar{y}$ and P_y can be calculated via the weighted and transformed points follows:

$$\begin{cases} \bar{y} = \sum_{i=0}^{2L} \omega_x^{[i]} g(\chi^i) & (5.18) \\ P_y = \sum_{i=0}^{2L} \omega_p^{[i]} (g(\chi^i) - \bar{y})(g(\chi^i) - \bar{y})^T & (5.19) \end{cases}$$

Considering a nonlinear system follows

$$\begin{cases} x_{k+1} = f(x_k, u_k, w_k) & (5.20) \\ y_k = g(x_k, v_k) & (5.21) \end{cases}$$

where k is the time index, u_k, x_k and y_k refer to the system input, state and measurement, respectively. w_k and v_k represent the system process noise and measurement noise, respectively.

According to [106], the implementation of the UKF can be summarised into the following steps:

- Step 0: Initialisation

$$\hat{x_0} = E[x_0], \quad P_{x_0} = E[(x_0 - \hat{x_0})(x_0 - \hat{x_0})^T] \tag{5.22}$$

- Step 1: Calculate the sigma-points at time step $k-1$.

$$\chi_{k-1} = [\hat{x}_{k-1} \quad \hat{x}_{k-1} + \gamma\sqrt{P_{k-1}} \quad \hat{x}_{k-1} - \gamma\sqrt{P_{k-1}}] \tag{5.23}$$

- Step 2: Predict the state and error covariance from time $k-1$ to k.

$$\begin{cases} \chi_{k|k-1}^{[i]} = f(\chi_{k-1}^{[i]}, u_{k-1}) & (5.24) \\ \hat{x}_k^- = \sum_{i=0}^{2L} \omega_x^{[i]} \chi_{k|k-1}^{[i]} & (5.25) \\ P_{x,k}^- = \sum_{i=0}^{2L} \omega_p^{[i]} (\chi_{k|k-1}^{[i]} - \hat{x}_k^-)(\chi_{k|k-1}^{[i]} - \hat{x}_k^-)^T & (5.26) \end{cases}$$

- Step 3: Predict the system measurement y_k^-, the measurement error covariance $P_{y,k}$ and the cross-covariance $P_{xy,k}$ at time k.

$$\begin{cases} Y_{k|k-1}^{[i]} = g(\chi_{k-1}^{[i]}, u_k) & (5.27) \\ \hat{y}_k^- = \sum_{i=0}^{2L} \omega_x^i Y_{k|k-1}^{[i]} & (5.28) \end{cases}$$

$$P_{y,k} = \sum_{i=0}^{2L} \omega_p^{[i]} (Y_{k|k-1}^{[i]} - \hat{y}_k^-)(Y_{k|k-1}^{[i]} - \hat{y}_k^-)^T \tag{5.29}$$

$$P_{xy,k} = \sum_{i=0}^{2L} \omega_p^{[i]} (\chi_{k|k-1}^{[i]} - \hat{x}_k^-)(Y_{k|k-1}^{[i]} - \hat{y}_k^-)^T \tag{5.30}$$

- Step 4: Calculate the Kalman gain.

$$K_k = P_{xy,k} P_{y,k}^{-1} \tag{5.31}$$

- Step 5: Update the mean and covariance of the state.

$$\begin{cases} \hat{x}_k = \hat{x}_k^- + K_k(y_k - \hat{y}_k^-) & (5.32) \\ P_{x,k} = P_{x,k}^- - K_k P_{y,k} K_k^T & (5.33) \end{cases}$$

- Step 6: Repeat Step 1 to 5 for the next time step.

5.4.2 UKF for SOC estimation

In this work, the battery SOC is defined as the available capacity to the nominal capacity of the battery as

$$x_k = x_{k-1} + \eta I_k \Delta / Q \tag{5.34}$$

where x_k and x_{k-1} represent the SOC at time k and $k-1$, respectively. I_k represents the current at time k, Δt represents the sampling period, Q is the maximum available capacity of the battery, and η represents the coulombic efficiency.

The established strain based NN model, namely M_s and the voltage based empirical model, namely M_v, can both be used to estimate SOC with the utilisation of UKF. Both of these systems have the same state update equation as presented in Eq. (5.34).

5.4.2.1 Strain based SOC estimator

For the SOC estimator that uses M_s for SOC estimation, the observation of the estimator is the strain information (S1 - S3). Therefore, the measurement equation of the strain based SOC estimator can be presented as

$$y_{s,k} = h_s(x_k, T_k) \tag{5.35}$$

where $y_{s,k}$ presents the prediction of the strain information at time k, h_s can be obtained via the BP-NN model.

5.4.2.2 Voltage based SOC estimator

For the SOC estimator that uses M_v for SOC estimation, the observation of the estimator is the battery terminal voltage. Therefore, the output prediction equation of the voltage based SOC estimator can be represented as

$$y_{v,k} = k_0 + R_0 I_k + k_1 x_k + k_2/x_k + k_3 ln(x_k) + k_4 ln(1 - x_k) \tag{5.36}$$

where $y_{s,k}$ is the prediction of the voltage information at time k, k_0, k_1, k_2, k_3, k_4 and R_0 are the model parameters.

5.4.2.3 Enhanced strain based SOC estimator

It should be noted that both the strain based SOC estimator and the voltage based SOC estimator use a single physical quantity (strain or voltage) as the system observation, which means that if there is a large error in the measurement, the system performance will be greatly affected. When both strain and voltage are adopted as the system observations, this will reduce the impact on the system caused by the measurement error of a single physical quantity (strain or voltage), thereby improving the accuracy of SOC estimation. Moreover, since M_s and M_v are independent of each other, which means that when M_s has a relatively large model error, M_v can be used to correct the large SOC estimation error caused by the model error of M_s, thereby enhancing the performance of the strain based SOC estimator. Therefore, an enhanced strain based SOC estimator is developed, which uses both the strain information ($S1$ - $S3$) and the battery terminal voltage as the observations. The output prediction of the enhanced strain based SOC estimator can be represented as

$$y_{sv,k} = [y_{s,k} \quad y_{v,k}]^T \tag{5.37}$$

where $y_{s,k}$ and $y_{v,k}$ can be determined from Eq. (5.35) and Eq. (5.36), respectively. In this case, the system observation contains two elements at time k, $y_{s,k}$ and $y_{v,k}$. Therefore, the dimensions of the measurement error covariance and the cross-covariance are (2 × 2) and (1 × 2), respectively. Then, the corresponding Kalman filter gain (dimension = 1 × 2) can be calculated to update the system state $\hat{x_k}$. In this approach, the estimated state is the optimal value to meet both the strain prediction and the voltage prediction.

5.5 Results and discussions

In order to validate the accuracy and reliability of the developed SOC estimators, the SOC estimation results by using Ampere-hour (Ah) method, the voltage based SOC estimator, the KNN-DTW based SOC estimator [150], the developed strain based SOC estimator and the enhanced strain based SOC estimator are compared in this section. For fair comparison, the data obtained from Cycle 1 to 5 is used for modelling and the data obtained from Cycle 6 is utilised for validation. As a trade-off of accuracy and computational cost, the SOC resolution of the KNN-DTW SOC estimator is set as 1% in this study.

5.5.1 The charging test

In the charging test, the initial SOC value x_0 is set as 0.05, the SOC estimation results by using Ah method, the strain based SOC estimator and the voltage based SOC estimator are presented in Fig. 5.13 and estimation errors are shown in Fig. 5.14. It is clear that the SOC estimation results obtained by Ah method has a bias due to the initial SOC error. Since Ah method is an open loop method, the bias error cannot be eliminated. Therefore, the Mean Absolute Error (MAE), Root Mean Square Error (RMSE) and Maximum Absolute Error (MaxAE) of the Ah method are all 5%. Due to the utilisation of UKF, the SOC estimation obtained by the strain based SOC estimator and the voltage based SOC estimator can converge towards the true SOC value. The MAEs of the SOC estimated by the strain based SOC estimator and the voltage based SOC estimator are 0.97% and 1.08%, respectively. The SOC estimation performance in RMSE of the strain based SOC estimator and the voltage based SOC estimator are 1.22% and 1.35%, respectively. The MaxAE of the strain based SOC estimator is 3.09% . The MaxAE of the voltage based SOC estimator is 2.55% . It can be found that the overall SOC estimation accuracy of the strain based SOC estimator is better than the voltage based SOC estimation in terms of MAE and RMSE. For the local maximum error, the voltage based SOC estimator has a better performance in the charging test. Moreover, since the voltage change is more obvious when the SOC is extremely low, the voltage-based estimator also has a faster convergence.

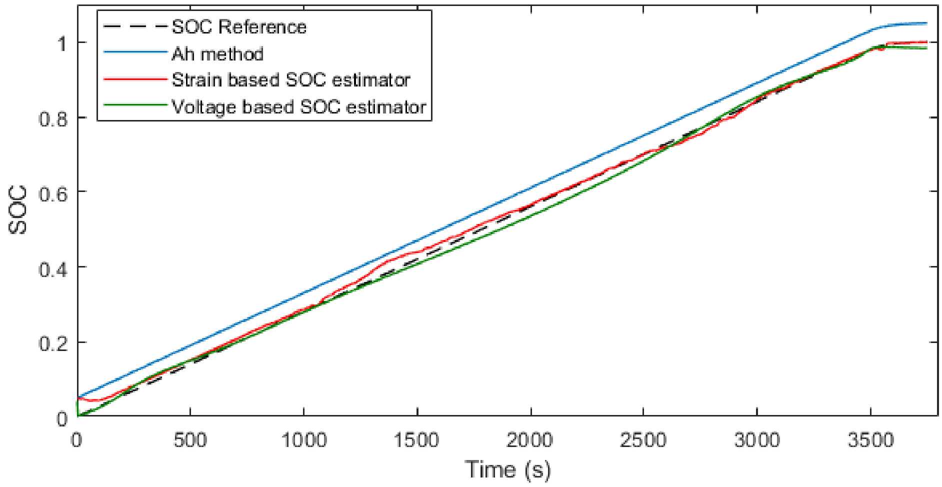

Figure 5.13: SOC estimation results in the charging test

The SOC estimation results in the charging test of the developed strain based

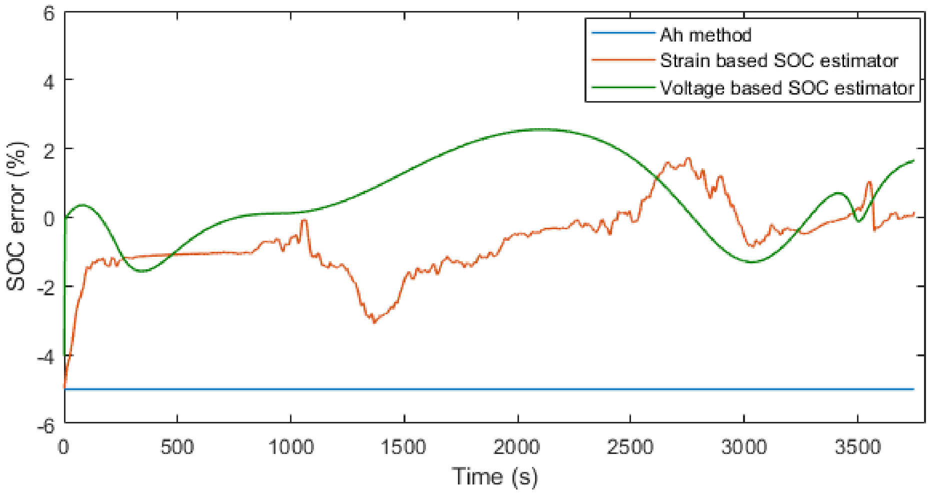

Figure 5.14: SOC estimation errors in the charging test

SOC estimator and the KNN-DTW based SOC estimator are compared in Fig. 5.15 and the estimation errors are shown in Fig. 5.16. It is clear that the SOC estimation results obtained by the developed strain based SOC estimator has better accuracy in than ones obtained by the KNN-DTW based SOC estimator. The numerical estimation results in terms of MAE, RMSE and MaxAE are compared in Table 5.3. It should be noted that the estimation accuracy of the KNN-DTW based SOC estimator is not affected by the initial setting of the SOC value. The SOC estimation at each moment is completely independent, which means that the historical information of SOC is not adopted in the KNN-DTW based SOC estimator. However, since the Ah method is not adopted in the KNN-DTW based SOC estimator, large estimation errors will be generated in the SOC regions where the strain curves are lees identifiable. Moreover, the simulation results also imply that the KNN-DTW based SOC estimator cannot deal with the random fluctuations with relatively few training cycles.

The SOC estimation results of the strain based SOC estimator and the enhanced strain based SOC estimator in the charging test are compared in Fig. 5.17

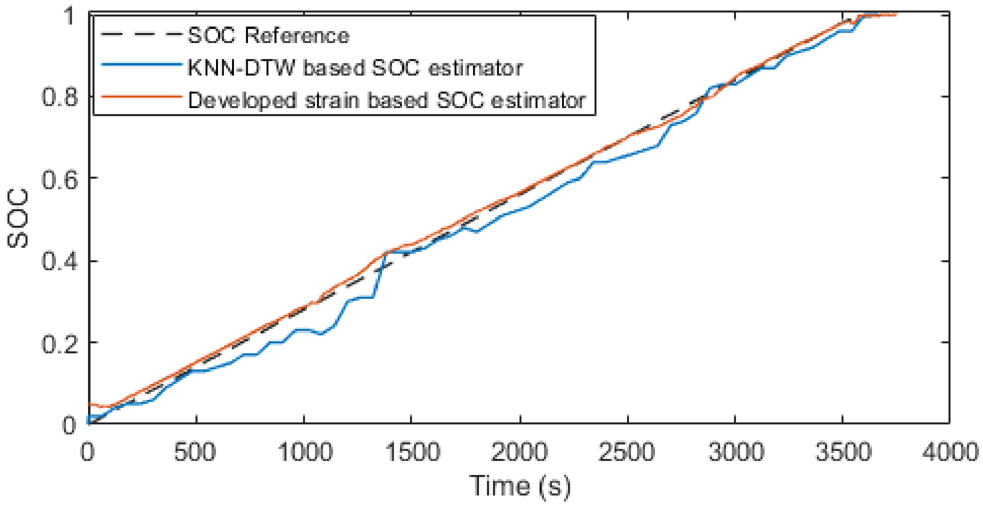

Figure 5.15: SOC estimation errors in the charging test

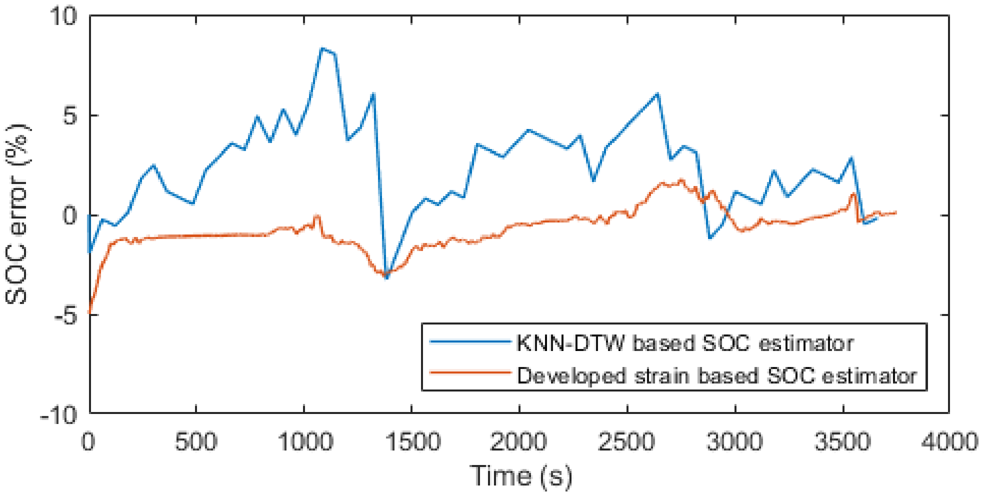

Figure 5.16: SOC estimation errors in the charging test

and the estimation errors are compared in Fig. 5.18. Compared with the strain based SOC estimator, the MAE of the enhanced strain based SOC estimator is improved from 0.97% to 0.64%, the RMSE of the enhanced strain based SOC estimator is enhanced from 1.22% to 0.94%. The MaxAE of the enhanced strain based SOC estimator is also reduced from 3.09% to 2.39%. The numerical SOC estimation results by different methods are also summarised in Table 5.3. It can be seen that for the charging test, the enhanced strain based SOC estimator has the best performance in terms of MAE, RMSE and MaxAE.

Table 5.3: SOC estimation results in the charging test

	MAE	RMSE	MaxAE
Ah method	5%	5%	5%
Voltage based SOC estimator	1.08%	1.35%	2.55%
KNN-DTW based SOC estimator	2.67%	3.28%	8.33%
Strain based SOC estimator	0.97%	1.22%	3.09%
Enhanced strain based SOC estimator	**0.64%**	**0.94%**	**2.39%**

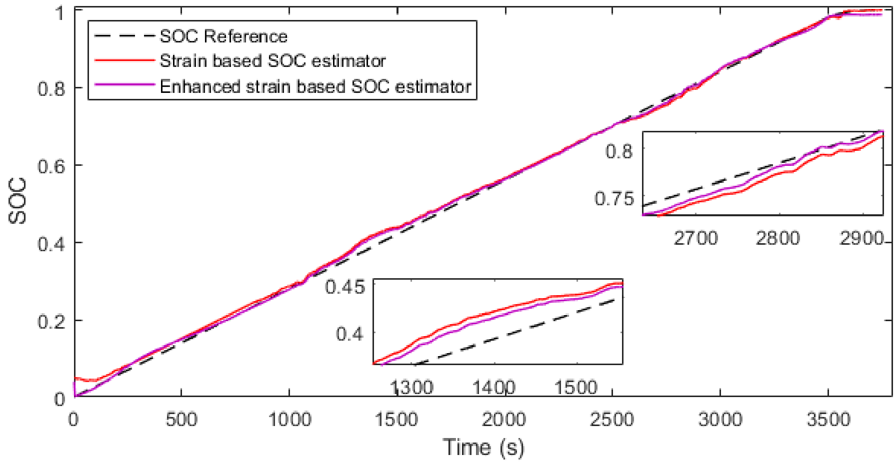

Figure 5.17: SOC estimation results in the charging test

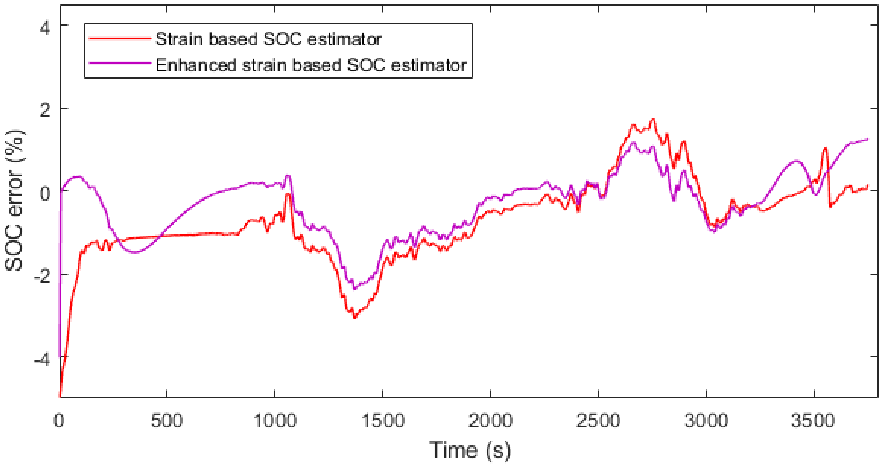

Figure 5.18: SOC estimation errors in the charging test

5.5.2 The discharging test

In the discharge test, the initial value of SOC x_0 is set to 0.8 to test the performance of each estimator when a huge initial error of SOC occurs. The estimation results of Ah method, the strain based SOC estimator and the voltage based SOC estimator are shown in Fig. 5.19, and the estimation errors are illustrated in Fig. 5.20. As discussed previously, Ah method cannot eliminate the initial SOC error, the estimation result obtained by Ah method has a bias of 0.2 to the true SOC value. The MAE, RMSE and MaxAE of the estimation of Ah method are all 20%. Both of the strain based SOC estimator and the voltage based SOC estimator can converge to the true SOC value within 30 seconds. Since the voltage change is more obvious in the high SOC region, the voltage based SOC estimator has a faster convergence than the strain based SOC estimator. The MAEs of the strain based SOC estimator and the voltage based SOC estimator are 1.45% and 1.54%. respectively. The RMSEs of the strain based SOC estimator and the voltage based SOC estimator are 1.78% and 1.99%, respectively. The MaxAEs of the strain based SOC estimator and the voltage based SOC estimator are 3.36% and

3.88%, respectively. It can be seen that for the discharging test, the strain based SOC estimator yields more accurate estimation results than the voltage based SOC estimator in terms of MAE, RMSE and MaxAE.

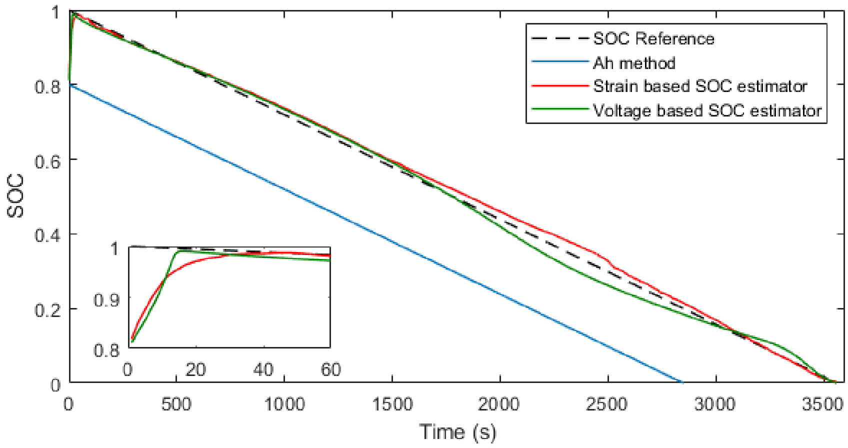

Figure 5.19: SOC estimation results in the discharging test

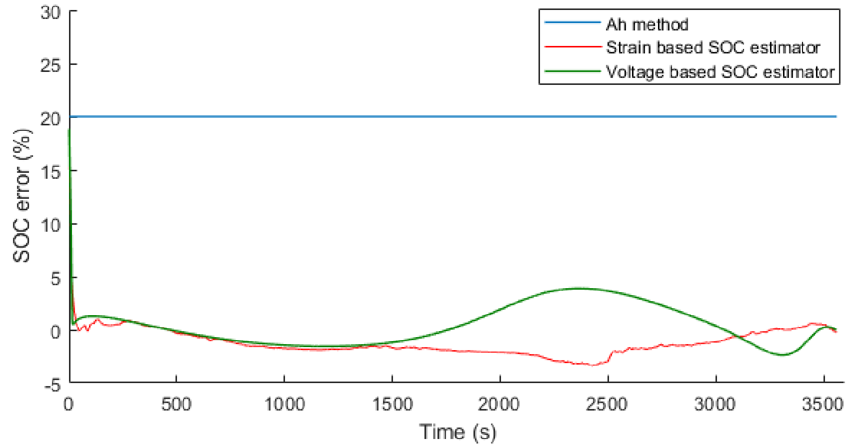

Figure 5.20: SOC estimation errors in the discharging test

The SOC estimation results of the developed strain based SOC estimator and the KNN-DTW based SOC estimator are compared in Fig. 5.21 and the estimation errors are shown in Fig. 5.22. As discussed previously, the KNN-DTW based SOC estimator cannot deal with the random fluctuations if few training cycles are adopted. Moreover, large estimation errors are observed from the KNN-DTW based SOC estimator in the SOC regions where the strain curves are less identifiable. The numerical estimation results in terms of MAE, RMSE and MaxAE are compared in Table 5.4. It can be seen that the developed strain based SOC estimator has better SOC estimation accuracy than the KNN-DTW based SOC estimator in terms of MAE, RMSE and MaxAE, respectively.

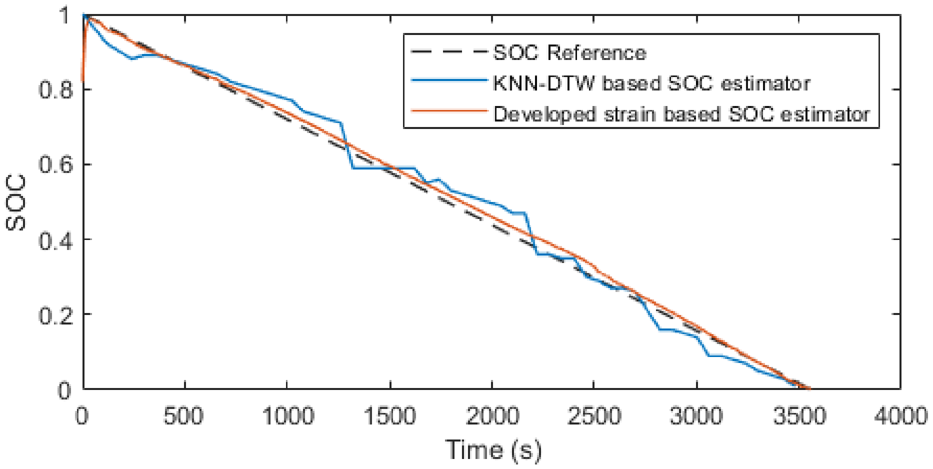

Figure 5.21: SOC estimation errors in the discharging test

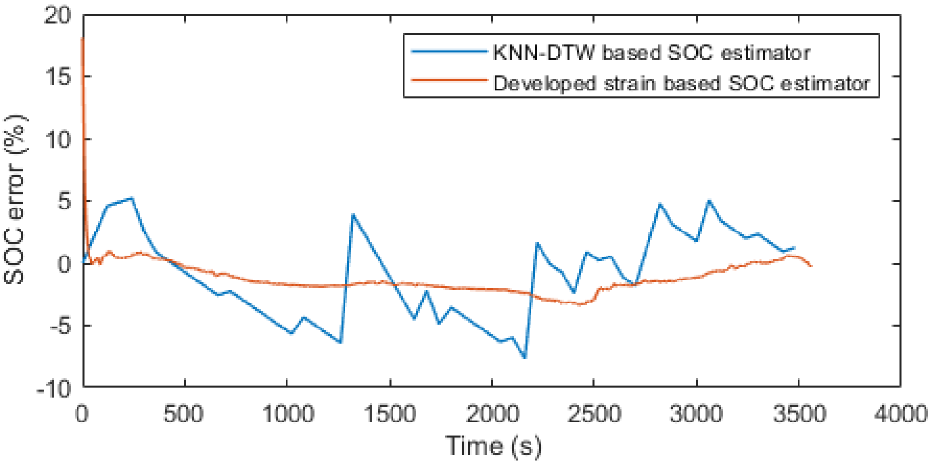

Figure 5.22: SOC estimation errors in the discharging test

The SOC estimation results of the strain based SOC estimator and the enhanced strain based SOC estimator in the discharging test are compared in Fig. 5.23 and the estimation errors are compared in Fig. 5.24. Compared with the strain based SOC estimator, the MAE of the enhanced strain based SOC estimator is improved from 1.45% to 1.21%, the RMSE of the enhanced strain based SOC estimator is improved from 1.78% to 1.43%. The MaxAE of the enhanced strain based SOC estimator is also reduced from 3.36% to 1.91%. The numerical SOC estimation results by different methods are presented in Table 5.4. It can be seen that for the discharging test, the enhanced strain based SOC estimator has the best performance in terms of MAE, RMSE and MaxAE.

Table 5.4: SOC estimation results in the discharging test

	MAE	RMSE	MaxAE
Ah method	20%	20%	20%
Voltage based SOC estimator	1.54%	1.99%	3.88%
KNN-DTW based SOC estimator	2.98%	3.55%	7.67%
Strain based SOC estimator	1.45%	1.78%	3.36%
Enhanced strain based SOC estimator	**1.21%**	**1.43%**	**1.91%**

5.6 Chapter summary

In this chapter, a strain based SOC estimator is firstly developed. Unlike insert FBG sensors inside the cell, the FBG sensors are mounted on the surface of the cell in this work to collect the strain data during the charging and discharging processes. The non-embedded layout will not cause any damage to the battery, and thus it will not affect the performance of the battery in terms of lifespan and maximum usable capacity, etc. Moreover, the non-embedded layout also can be flexibly installed or uninstalled based on application needs, which means that it is more friendly in engineering applications. Since the difference between the

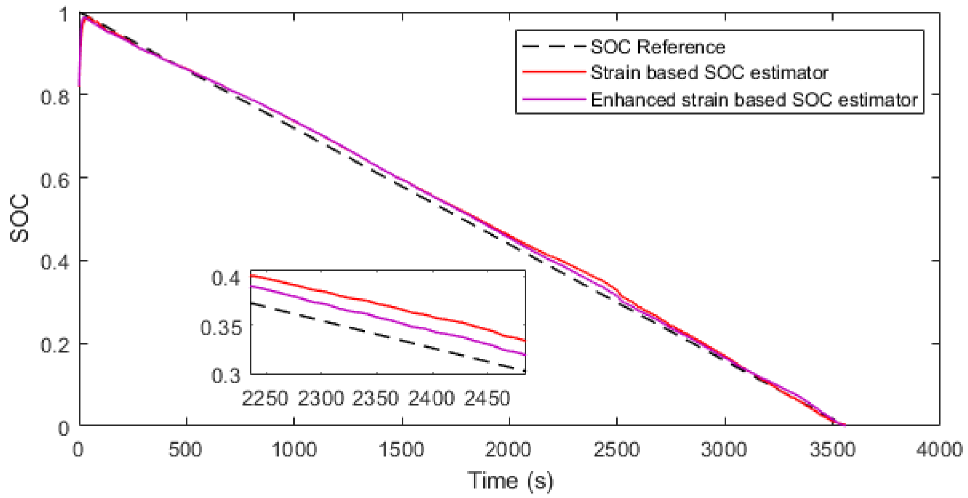

Figure 5.23: SOC estimation results in the discharging test

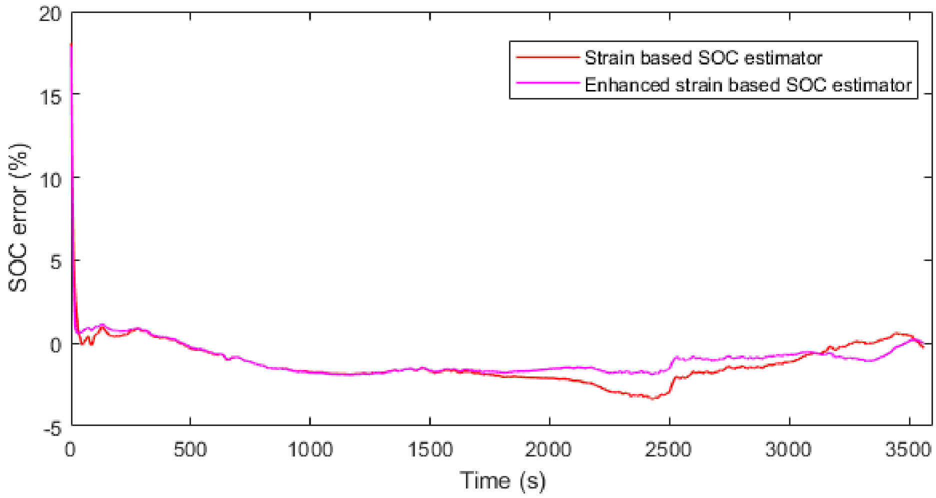

Figure 5.24: SOC estimation errors in the discharging test

measured strain S1 and S3 is very repeatable in every cycle, A BP based model is then developed to predict the difference between S1 and S3. The model structure is determined by using the LOCO method for the charging and discharging processes. For comparison, a combined model is built for battery terminal voltage prediction. Both the strain based model and the voltage based model are used for SOC estimation combined with the utilisation of UKF. The test results indicate that the strain based SOC estimator can accurately estimate the battery SOC in both charging and discharging processes. The estimation accuracy in terms of MAE and RMSE obtained by the strain based SOC estimator are better than the ones obtained by the voltage based SOC estimator in both of the charging and discharging tests. The simulation results also indicate that the developed strain based SOC estimator also has better estimation accuracy than the KNN-DTW based SOC estimator in terms of MAE, RMSE and MaxAE. In order to further enhance the estimation accuracy of the strain based SOC estimator, an enhanced strain based SOC estimator is then developed by combining the strain based model and the voltage based model. Compared with the strain based SOC estimator, the enhanced strain based SOC estimator achieves better results in terms of MAE, RMSE and MaxAE in both of the charging and discharging tests.

Chapter 6

Battery SOH Estimation

As one of the key functions of the battery management system (BMS), accurate battery state of health (SOH) estimation can effectively ensure battery operation safety, avoid potential failures and minimise the maintenance costs. However, accurate SOH estimation is difficult to achieve because the complex physical and chemical characteristics of battery degradation cannot be obtained directly. For this reason, researchers and related practitioners have developed various SOH estimation methods to meet different application requirements. In this chapter, two popular types of SOH estimation methods, namely the capacity regression model based method and the charging curve analysis based method have been firstly established. The capacity regression model based method adopts the battery historical capacity information to estimate the current capacity in a recursive manner. When the historical capacity information of the battery can be calibrated or accurately estimated, such method can usually provide an accurate SOH estimation. However, to accurately obtain battery historical battery capacity information is a challenge in practical applications. Inaccurate historical capacity information will greatly affect the accuracy of the capacity regression model, and even lead to failure. The charging curve analysis based method estimates battery SOH only adopts the data collected in the present cycle, which means no historical battery information is required. However, such method is usually very sensitive to the measurement noise, and it is vulnerable to uncertainties. Moreover, under certain SOH levels, the characteristics of the charging curve are less recognisable, which leads this method to a decrease in the accuracy of the SOH estimation. To tackle the drawbacks of the capacity regression model based method and the charging curve analysis based method, a closed-loop SOH estimation method based on the UKF algorithm is developed in this chapter. The developed SOH estimation method combines the advantages of the capacity regression model based method and the charging curve analysis based method to offer more accurate SOH estimation results.

6.1 Experimental setup

Four commercial 18650 lithium-ion batteries have been used in this work for the ageing tests. The cathode material of the tested lithium-ion batteries is lithium iron phosphate (LFP) and the anode material is graphite. The key details of the batteries used in this work are shown in Table 6.1.

Table 6.1: Specifications of the batteries

Manufacturer	Nominal capacity	Nominal voltage	Upper/lower cut-off voltage	Standard charing current
Soshine	1.6Ah	3.2V	3.6V / 2V	1A (0.625C)

As the ageing of lithium-ion batteries is a complicated and slow process, accelerated ageing tests have been taken to accelerate the ageing process. All the four cells (namely Cell 1 to Cell 4) were used in the accelerated ageing tests. The accelerated ageing tests were carried out at room temperature, NEWARE BTS4000 battery tester was employed to control the current and voltage during the charging/discharging processes. The sampling frequency is set as 1 Hz in this experiment.

The accelerated ageing test consists of two parts, namely the accelerated ageing procedure and reference test procedure. In the accelerated ageing procedure, the cells were cycled under the 1C current rate follow a CCCV charing and CC discharging profile for 30 cycles to accelerate the ageing process. In the reference test procedure, a standard battery capacity test was performed according to the specifications provided by the manufacturer. The number of reference tests experienced is recorded as p. For both the accelerated ageing test and reference test, a period of 10 minutes was set between each cycle to rest the cells. The accelerated ageing procedure (every 30 accelerated ageing cycles) and the reference test procedure were performed alternately until the end of the accelerated ageing test, and data in terms of current, voltage and capacity obtained in every reference test were recorded.

The flowchart of the accelerated ageing test is shown in Fig. 6.1, where n_a represents the number of accelerated ageing cycle and n represents the total number of cycle.

In the accelerated ageing tests, each cell performed a total of 900 accelerated ageing cycles and 30 reference tests. The experimental data obtained from Cell 1 is used for modelling and algorithm design, the data obtained from Cell 2 to Cell 4 is used for validation.

6.2 SOH estimation based on the capacity regression model

In order to model the battery capacity regression model into a recursive manner, the battery capacity data measured in each reference test is utilised in this work.

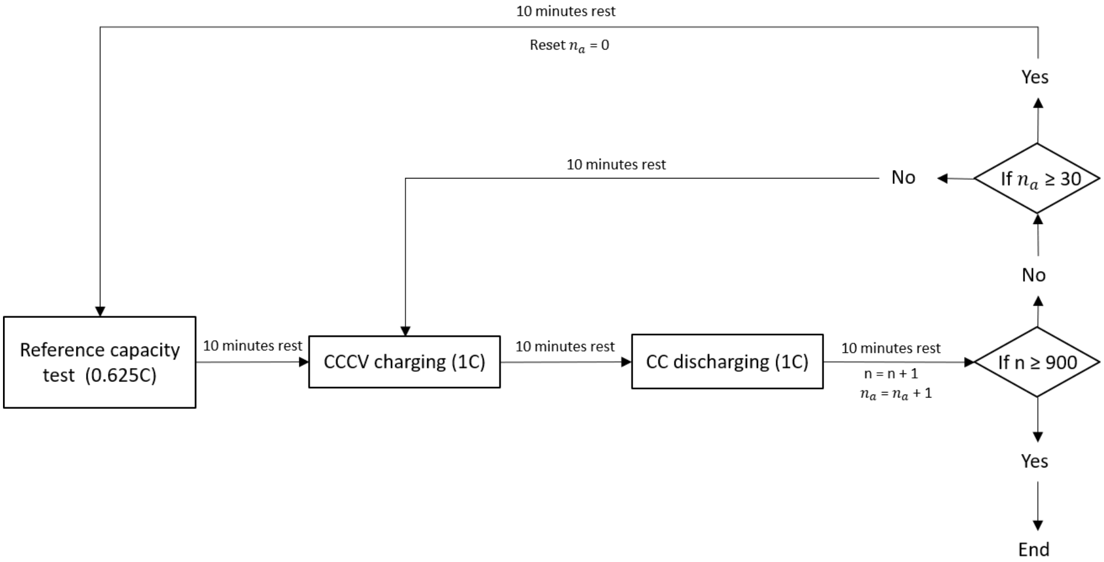

Figure 6.1: The flowchart of the accelerated ageing test

Define the measured battery capacity in the pth (p = 1, 2, 3, ... 30) reference test as C_p, and the measured capacity in the previous reference test as C_{p-1}, then the relationship between C_p and C_{p-1} can be obtained as shown in Fig. 6.2. It can be seen that C_p and C_{p-1} show a linear relationship. Therefore, the battery C_p is modelled as a linear function of C_{p-1}, as shown in Eq. (6.1).

$$C_p = a_1 C_{p-1} + a_2 \tag{6.1}$$

where a_1 and a_2 are the parameters to fit the model which can be identified by least squares method. In this work, a_1 and a_2 are identified as a_1 = 0.9511 and a_2 = 0.0691 with the coefficient of determination R^2 = 0.9949.

Once the initial capacity value is given, the corresponding capacity and SOH of the cell in each reference cycle can be calculated recursively.

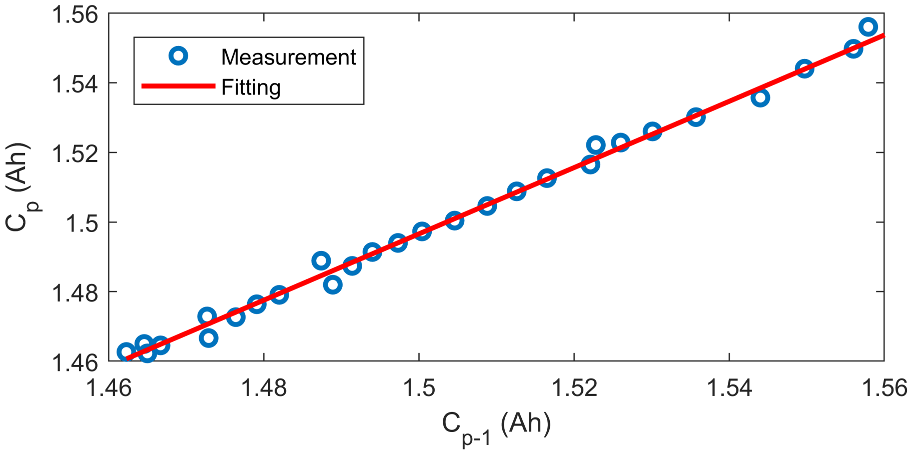

Figure 6.2: The relationship between C_p and C_{p-1} obtained from Cell 1

6.3 SOH estimation based on the charging curve analysis

Unlike the capacity regression model, the charging curve analysis based methods can perform estimations without the utilisation of the battery previous capacity. The battery capacity in each cycle can be estimated independently using the current and voltage data obtained from the corresponding cycles, such as the ICA approach. In order to circumvent the dV calculation problems mentioned in Section 2.5.2.2, the probability density function (PDF) based curve analysis method is used in this work. The PDF method was fist discussed in [135] to determine battery capacity and SOH. The rationale of the PDF method is equivalent to the ICA method in essence.

To perform the PDF method, the CC phase voltage curve is firstly divided into several segments with the same voltage interval. It should be noted that if the voltage interval is set too large, some small changes in the voltage curve will not be able to be captured, resulting in the loss of some peaks and valleys. If the interval is set too small, the voltage measurement noise will seriously affect PDF results, making it difficult to find the accurate positions of the peaks and valleys. For this reason, the voltage interval is set as 1 mV in this work. Therefore, the charging voltage PDF curve of each reference cycle can be determined, as shown in Fig. 6.3. It can be seen that the positions of the peaks and valleys move in the direction of the arrows as the cycle number increases. For each peak or valley, the obtained probability magnitude displays a consistent regularity during the ageing process. Therefore, the frequency of voltage samples within a certain voltage threshold can be integrated to achieve similar trends [135]. To be specific, the voltage threshold in this work is set as 3.37V - 3.45V, the frequency of voltage samples within the voltage threshold is defined as N. The relationship between the battery capacity and the corresponding values of N is shown in Fig. 6.4. It can be seen that the values of N decreases as the battery capacity fades, this relationship can be modelled as a power function, as shown in Eq. (6.2).

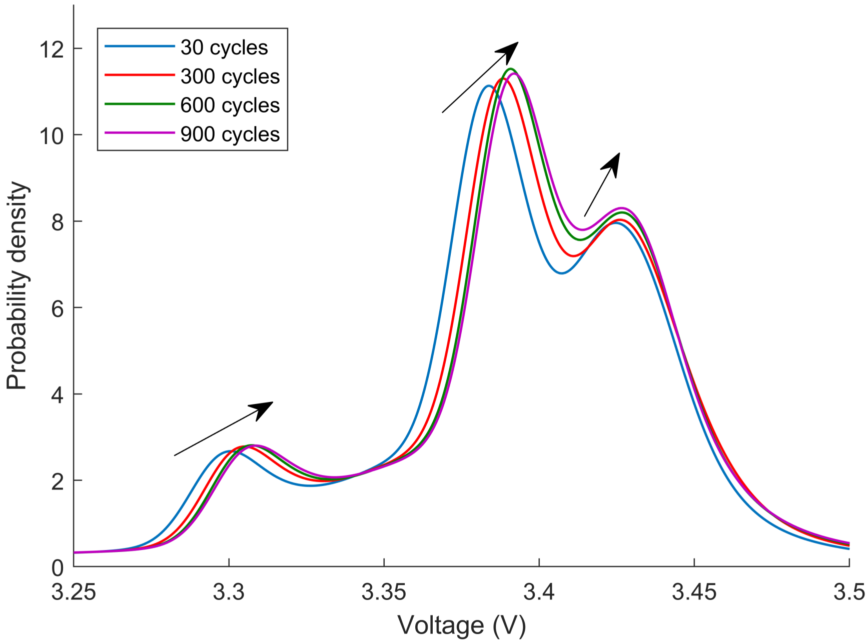

Figure 6.3: PDF results of Cell 1

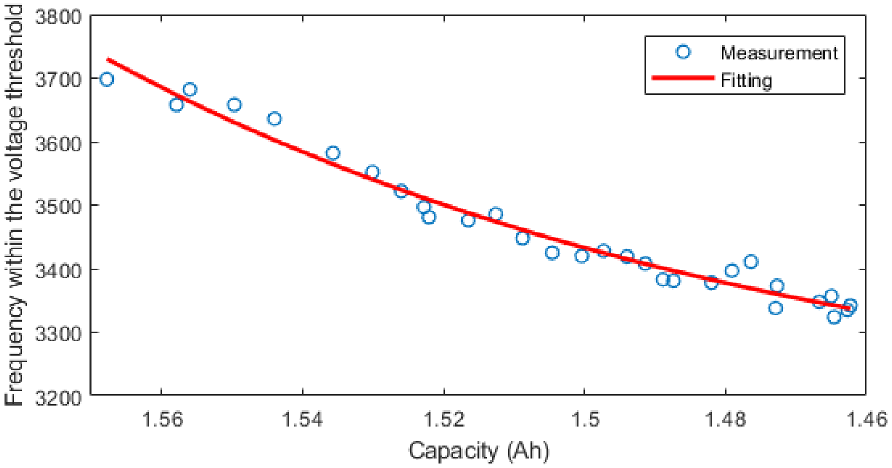

Figure 6.4: The relationship between the battery capacity and frequency N

$$N_n = b_1 C_n^{b_2} + b_3 \tag{6.2}$$

where N_n represents the frequency of voltage samples obtained within the voltage threshold in the nth cycle. C_n represents the measured capacity in the nth cycle. b_1, b_2 and b_3 are the parameters to fit the model. The parameters b_1, b_2 and b_3 are identified as $b_1 = 0.3756$, $b_2 = 13.32$ and $b_3 = 3152$ with the coefficient of determination $R^2 = 0.9506$.

According to Eq. (6.2), the battery capacity then can be calculated as shown in Eq. (6.3)

$$C_n = (\frac{(N_n - b_3)}{b_1})^{\frac{1}{b_2}} \tag{6.3}$$

Once the battery capacity is determined, the SOH of a battery can be estimated as $SOH = C_n/C_0 \times 100\%$.

6.4 SOH estimation based on the UKF algorithm

Adaptive filtering or observer algorithms have been widely used in battery state estimations, such as the application with equivalent circuit models and electrochemical models, etc. Based on a battery model, the adaptive filters can be used to identify the parameters in the battery model, such as battery capacity, internal resistance, OCV and other characterisation parameters. Once the parameters are identified, the battery SOH thus can be determined [130]. Adaptive filters also have been utilised for SOC and SOH joint estimation [40; 118; 119; 120]. However, the premise for this kind of joint estimation method to work well is to have an accurate estimation in SOC. As mentioned previously, accurate SOC estimation is also difficult to obtain in practical applications. Furthermore, such an adaptive structure may be subject to stability problem [121].

The key idea of the developed adaptive filter based SOH estimation method is to combine the advantages of the capacity regression based model and the PDF method. The accuracy of the capacity regression model highly depends on the last estimated capacity. If the previous estimated capacity has a large error, the new capacity calculated by the recursive algorithm will be biased, which leads to a larger estimation error due to the accumulation of errors. Therefore, the PDF method can be utilised as a feedback system for the capacity regression model. On the other hand, the PDF method only adopt the voltage data from the current cycle, the measurement noise and uncertainties may seriously affect the estimation results. Therefore, the capacity regression model can be used to improve the robustness of the PDF method. In order to form a closed loop system, the UKF algorithm is utilised in this work. The battery capacity is defined as the system sate, x, and the frequency of voltage samples (N) within the certain voltage threshold (3.37V - 3.45V) is defined as the system observation, y. According to Eq. (6.1) and (6.2), the system state equation and measurement equation can be respectively expressed as:

$$\begin{cases} x_n = a_1 x_{n-1} + a_2 & (6.4) \\ y_n = b_1 x_n^{b_2} + b_3 & (6.5) \end{cases}$$

where a_1, a_2, b_1, b_2 b_3 are the parameters determined in Section 6.2 and 6.3, respectively. The flowchart of the developed SOH estimation method is shown in Fig. 6.5

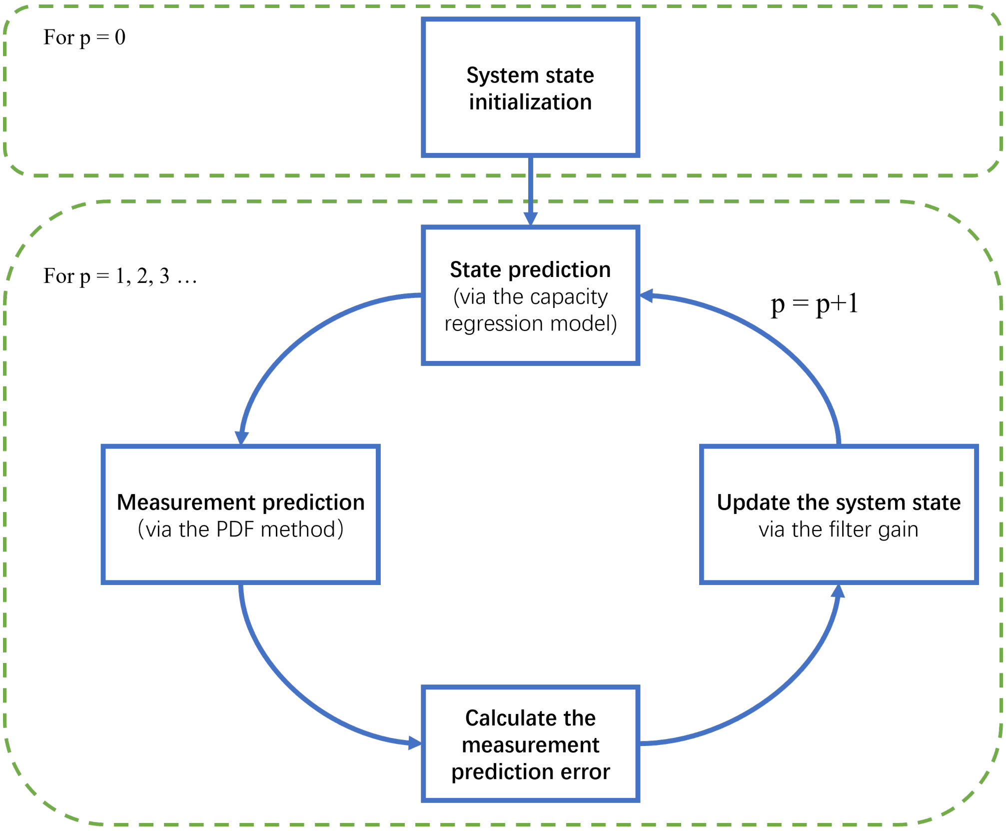

Figure 6.5: The flowchart of the developed SOH estimation method

6.5 Results and discussion

The estimation results of battery capacity and SOH via the methods in terms of the capacity regression model, PDF method and the developed UKF based method are presented and compared in this section. The data collected from Cell 1 is adopted for modelling, and the data collected from Cell 2, Cell 3 and Cell 4 are used for validation. For fair comparison, there is no battery calibration involved in any validation test, which means that the capacity estimated by the capacity regression model is based on the previous estimation value.

The battery capacity estimation results of Cell 2, Cell 3 and Cell 4 are presented in Fig. 6.6. It can be seen that the estimation error of the capacity regression model increases as the cycle number increases for all the tested cells. It indicates that the parameters of the capacity regression model obtained from Cell 1 are not well applicable to other cells. Since there is no capacity calibration during the entire estimation process, the errors caused by the inappropriate parameters are accumulated. Therefore, the estimation error of the capacity regression model increases as the cycle number increases. The PDF based method does not suffer from the problem of error accumulation because the capacity estimation is independent in each cycle. However, the actual charging current used in the reference cycle (0.625C) is much larger than the typical PDF charging current (0.04C) which causes larger errors in the counting of voltage samples N. Moreover, since the number of N counted in each cycle decreases as the battery capacity fades, the error caused by N counting has a grater impact on the estimation result as the cycle number increases. Therefore, the accuracy of PDF method in capacity estimation decreases as the cycle number increases. The developed adaptive filter method effectively combines the advantages of the capacity regression model and the PDF method. The value of capacity determined by the PDF method can provide new idea to the capacity regression model, the issue of error accumulation is thus avoided. Fur-

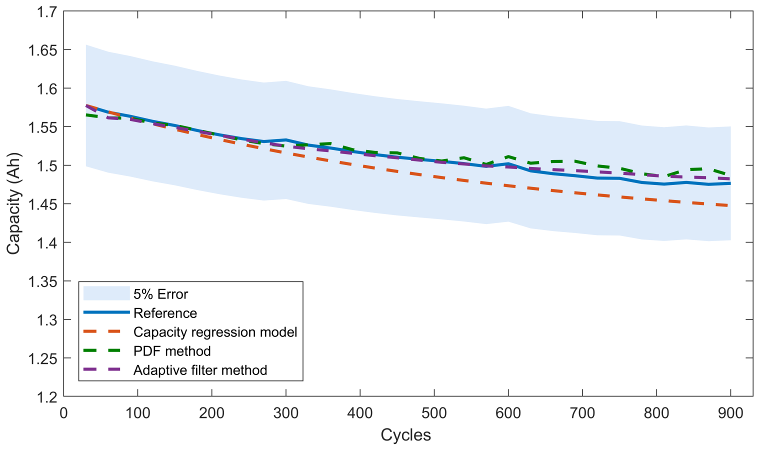

(a) Cell 2

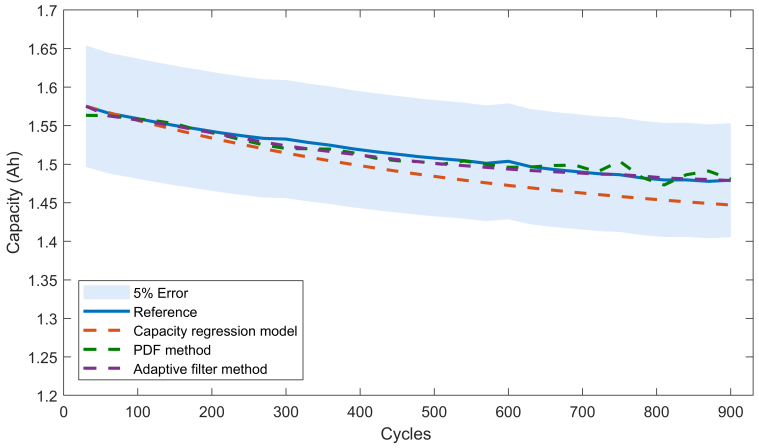

(b) Cell 3

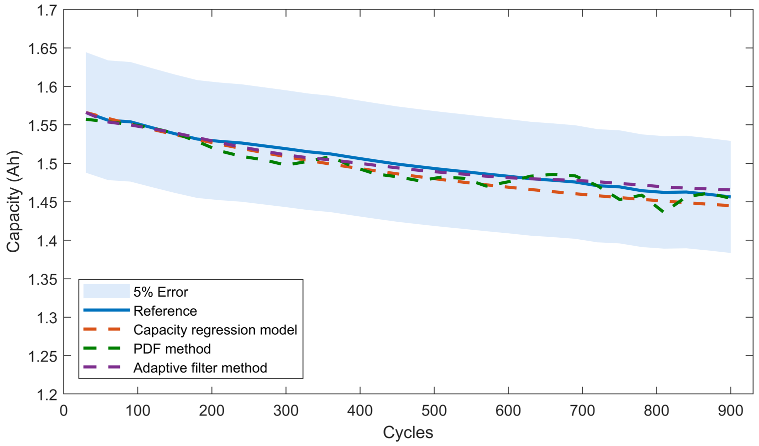

(c) Cell 4

Figure 6.6: Comparison of battery capacity estimation results

thermore, the influence of measurement noise on the estimation results is reduced due to the experience provided by the capacity regression model.

In order to further compare the accuracy of the capacity regression model, the PDF method and the developed adaptive filter method, the root mean square error (RMSE), mean absolute (MAE) and maximum absolute error (MaxAE) are used to assess the performance of these three methods in both of capacity estimation and SOH estimation. The formulas are defined as follows:

$$\begin{cases} \mathrm{RMSE}_C = \sqrt{\dfrac{\sum_{i=1}^{n}(y_i - \hat{y}_i)^2}{n}} & (6.6) \\ \mathrm{MAE}_C = \dfrac{1}{n}\displaystyle\sum_{i=1}^{n}|y_i - \hat{y}_i| & (6.7) \\ \mathrm{MaxAE}_C = \max(|y_i - \hat{y}_i|), i = 1, 2, ...n & (6.8) \end{cases}$$

$$\begin{cases} \mathrm{RMSE}_S = \sqrt{\dfrac{\sum_{i=1}^{n}((y_i - \hat{y}_i)/C_0)^2}{n}} \times 100\% & (6.9) \\ \mathrm{MAE}_S = \dfrac{1}{n}\displaystyle\sum_{i=1}^{n}|(y_i - \hat{y}_i)/C_0| \times 100\% & (6.10) \\ \mathrm{MaxAE}_S = \max((|y_i - \hat{y}_i|)/C_0) \times 100\%,\ i = 1, 2, ...n & (6.11) \end{cases}$$

where n represents the sample size of test data, C_0 represents the nominal capacity of the battery, which equals to 1.6 Ah in this study. y_i and $\hat{y}_i$ represent the measured and the corresponding estimated battery capacity in the $i\ th$ reference cycle, respectively. The subscripts C and S represent the corresponding assessments in the capacity estimation and SOH estimation, respectively.

The numerical estimation results of battery capacity and SOH are presented in Tables 6.2 and 6.3, respectively. It can be seen that the developed adaptive filter method generally have better performance in capacity and SOH estimation than the other two methods. For Cell 2 and Cell 3, the developed adaptive filter

Table 6.2: Comparison of the capacity estimation results

Cell	Assessment	Capacity regression model	PDF	Adaptive filter
Cell 2	RMSE_C(Ah)	0.0158	0.0094	**0.0065**
	MAE_C(Ah)	0.0139	0.0072	**0.0049**
	MaxAE_C(Ah)	0.0254	0.0201	**0.0127**
Cell 3	RMSE_C(Ah)	0.0190	0.0071	**0.0062**
	MAE_C(Ah)	0.0170	0.0057	**0.0049**
	MaxAE_C(Ah)	0.0283	0.0175	**0.0124**
Cell 4	RMSE_C(Ah)	0.0102	0.0118	**0.0099**
	MAE_C(Ah)	0.0091	0.0095	**0.0081**
	MaxAE_C(Ah)	**0.0139**	0.0261	0.0182
Average	RMSE_C(Ah)	0.0150	0.0094	**0.0075**
	MAE_C(Ah)	0.0133	0.0075	**0.0060**
	MaxAE_C(Ah)	0.0225	0.0212	**0.0144**

method has the best performance in terms of RMSE, MAE and MaxAE for both capacity estimation and SOH estimation. For Cell 4, the developed adaptive filter method also has the best performance in terms of RMSE and MAE. However, since the capacity values estimated by the PDF method during cycles 210 to 330 have large errors to the reference capacity, which means that the measurement equation in the developed adaptive filter method cannot accurately predict the observation values in these corresponding cycles. Therefore, due to the impact of the PDF method, the MaxAE of the developed method occurred in the $300th$ cycle. However, compared the developed method with the PDF method, the MaxAE obtained in Cell 4 is reduced by 30.27% in capacity estimation and 30.18% in SOH estimation. The average estimation results also indicate that the developed method has the best overall performance in both capacity estimation and SOH estimation.

Comparing the developed method with the capacity regression model, the developed method achieves a 50% improvement in term of RMSE and a 54.88%

Table 6.3: Comparison of the SOH estimation results

Cell	Assessment	Capacity regression model	PDF	Adaptive filter
Cell 2	RMSE_S (%)	0.9860	0.5868	**0.4086**
	MAE_S(%)	0.8680	0.4512	**0.3063**
	MaxAE_S(%)	1.5870	1.2591	**0.7929**
Cell 3	RMSE_S(%)	1.1892	0.4424	**0.3906**
	MAE_S(%)	1.0611	0.3542	**0.3077**
	MaxAE_S(%)	1.7695	1.0928	**0.7741**
Cell 4	RMSE_S(%)	0.6345	0.7363	**0.6187**
	MAE_S(%)	0.5699	0.5928	**0.5071**
	MaxAE_S(%)	**0.8673**	1.6325	1.1398
Average	RMSE_S(%)	0.9366	0.5885	**0.4726**
	MAE_S (%)	0.8330	0.4661	**0.3737**
	MaxAE_S (%)	1.4079	1.3281	**0.9023**

improvement in term of MAE in capacity estimation. The MaxAE is also reduced by 36%. For the SOH estimation, the developed method achieves a 49.54% improvement in term of RMSE and a 55.13% improvement in term of MAE. The MaxAE is reduced by 35.91%.

Comparing the developed method with the PDF method, the developed method achieves a 20.21% improvement in term of RMSE and a 20% improvement in term of MAE in capacity estimation. The MaxAE is reduced by 32.07%. For the SOH estimation, the developed method achieves a 19.69% improvement in term of RMSE and a 19.82% improvement in term of MAE. The MaxAE is reduced by 32.06%.

In summary, the developed method can effectively combine the advantages of the capacity regression model and the PDF method, more accurate estimation results in both capacity estimation and SOH estimation can be achieved.

6.6 Chapter summary

In this chapter, the performance of the capacity regression model and the PDF method in capacity and SOH estimation have been reviewed and compared. The test results indicate that the capacity regression model suffers from the problem of error accumulation, and the PDF method suffers from noise-sensitive issues. To further improve the SOH estimation accuracy, an adaptive filter based SOH estimation method is developed in this chapter by combining the advantages of the capacity regression model and the PDF method. The PDF method is utilised as a feedback system for the capacity regression model to provide a reference of capacity estimation. Meanwhile, the capacity regression model is utilised to provide experience for the PDF method to enhance the robustness. The test results confirm that the developed method can achieve the best overall performance in terms of RMSE, MAE and MaxAE for both capacity estimation and SOH estimation compared with the other two methods. The focus of this chapter is to develop a new concept of combining the advantages of different methods for battery SOH estimation. The models and filters that can be utilised in this framework are not limited to the ones mentioned in this chapter. How to choose the most suitable models and filters according to actual needs requires further study.

Chapter 7

Conclusions and Future work

7.1 Conclusion

A BMS is essential for lithium-ion batteries to protect the cell from working in inappropriate working conditions. Moreover, a BMS can also help prolong the service life of the cells and improve the battery efficiency. This thesis studies the BMS for lithium-ion batteries, and focuses on the methods of battery modelling, monitoring and states estimation. The contributions of this thesis are summarised as follows:

1. A battery test system aided with non-embedded FBG sensors has been set up in the laboratory. The FBG sensors are installed on the surface of the batteries in a non-embedded manner to avoid damage to the integrity of the cells. A battery tester (NEWARE BTS-4000) is used to control cells for different charging and discharging profiles simulation, and record the electrical signals such as battery terminal voltage and current. An optical sensing interrogator (Micron Optics SM-130) is utilised to capture and record the wavelength signals that obtained by the FBG sensors. Moreover, a thermal chamber (BINDER MK) is used to control the battery ambient temperature

during the tests. All test equipment, such as the battery tester, FBG interrogator and the thermal chamber are connected to the host computer via a wireless network.

Different types of lithium-ion batteries have been tested using this battery test system with various current profiles and temperature conditions. Sufficient test data have been obtained for the purposes of battery characterisation, modelling and state estimation, etc. This battery test system can capture both electrical signals (such as terminal voltage and current) and non-electrical signals (such as temperature and strain) of the batteries, and provide more comprehensive dynamic characteristics of the batteries. In addition to laying the foundation of this research, this battery test system can also serve other related research and contribute to future BMS development.

2. An extensive literature survey on BMS is presented in this thesis and mainly focuses on the following fields. Firstly, the properties of lithium-ion batteries have been reviewed, such as battery capacity, OCV, effects of temperature, and effects of ageing. Furthermore, different battery modelling methods have been reviewed and compared, including white-box models, grey-box models and black-box models. Moreover, different battery SOC estimation methods and SOH estimation methods are analysed and compared. Finally, the working principle and applications of FBG sensing technology are analysed. The literature not only provides a comprehensive understanding of the battery management system, but is also the important support for the innovative research in this paper.

3. In order to accurately capture the electrical dynamic characteristics of lithium-ion batteries at different temperatures, a DP model with temperature compensation is developed in this thesis. The parameters such as battery capac-

ity, OCV, internal resistances and capacitances are identified using the RLS algorithm over a wide range of battery operating temperature. The developed temperature compensated battery model is tested and verified under various dynamic profiles in different temperatures. To further analyse the importance of the temperature compensation, the developed battery model (with temperature compensation) is utilised for SOC estimation at different temperatures. Compared with the conventional DP model (without temperature compensation), the developed model can achieve more accurate results in SOC estimation. Therefore, the developed battery model with temperature compensation can provide effective support for lithium-ion batteries to operate at different temperatures, and also contribute to the development of advanced thermal management strategies.

4. A multi-point battery temperature monitoring method based on FBG sensing technology has been implemented in this thesis. Compared with the conventional temperature monitoring method for lithium-ion batteries, this method can realise the temperature measurement of multiple points with only one optical fiber, which greatly saves the costs in terms of space, wiring and management. In order to eliminate the influence of other factors on FBG measurement, a data driven based FBG temperature calibration method is then developed. Compared with the conventional temperature calibration method, the developed method can be used online without affecting the normal operation of the batteries. Moreover, the developed method does not require laboratory test environment and it is more friendly in engineering applications. The validation results show that the developed method has good accuracy and reliability in battery temperature monitoring. The developed method can not only be applied to the temperature monitoring of battery based energy storage systems, but also has the potential to serve

temperature monitoring systems in other fields.

5. Based on the signals obtained via the FBG sensors, a strain based battery SOC estimator is developed in this thesis. The developed SOC estimator can estimate battery SOC without the measurement of battery terminal voltage, thus it is suitable for the applications where battery voltage is difficult to measure. Furthermore, the developed SOC estimation method can also operate aided with both of strain and voltage signals. In this case, the influence of voltage measurement error can be significantly reduced and the robustness of SOC estimation can thus be enhanced. This enhanced SOC estimator is suitable for the applications where battery voltage cannot be accurately measured. Unlike insert FBG sensors inside the cell, the FBG sensors in this work are mounted on the surface of the cell to capture the strain signals. The non-embedded layout can ensure the integrity of the cell, and will not affect the battery performance in terms of capacity and lifespan, etc. Moreover, the non-embedded layout also makes the FBG sensors can be flexibly installed or uninstalled depending on the application needs, which is more friendly for engineering applications.

6. Finally, a UKF based SOH estimation method is developed in this thesis, which combines the advantages of the capacity regression model and the charging curve analysis method. The charging curve analysis method is utilised as a feedback system for the capacity regression model to provide a reference of capacity estimation. Meanwhile, the capacity regression model is utilised to provide experience for the charging curve analysis method to enhance the robustness. Comparing with the conventional SOH estimation methods, the developed method can achieve more accurate and reliable SOH estimation performance. The focus of this method is to develop a new con-

cept of combining the advantages of different methods for battery SOH estimation, to achieve more accurate, reliable and robust estimation results.

7.2 Future work

In this thesis, some key technologies of BMS, such as battery modelling, monitoring, states estimations have been deeply studied. However, there are several areas in BMS worthy of further improvement and research, such as the following aspects.

1. Characterisation of the battery ageing process. Battery ageing is a complex process which is caused by different mechanisms and the ageing rate can be influenced by various factors, such as storage and operating temperatures, profile load, depth of discharge (DOD), operating SOC range and cut-off voltages, etc. Although the battery accelerated ageing test used in this thesis can effectively obtain the battery capacity attenuation pattern and the charging curve characteristics change, it was performed under fixed operating conditions (i.e. constant operating temperature, DOD and cut-off voltages). Therefore, a comprehensive battery ageing experiment which considers different influencing factors needs to be carried out in the future, and the battery SOH estimation method developed in this thesis can be further evolved.

2. Battery protection and fault diagnosis. In order to protect the battery and avoid the occurrence of failures, real-time monitoring of the battery is necessary. In BMS, the commonly monitored signals of a battery include the battery current, terminal voltage, and surface temperature. However, the volume and internal structure of the battery electrodes may also have minor changes that are not easily detectable when or before the faults (such as

short-circuit, over-charging, over-discharging, over-voltage and under-voltage, etc.) occur. The monitoring of battery internal and external strain information can effectively detect these small changes. Therefore, using FBG sensors to monitor battery strain information can potentially support fault prevention and early warning.

3. Cascade utilisation of lithium-ion batteries. With the rapid development of EVs, a large number of lithium-ion batteries will be retired from EVs in the near future. How to handle the retired lithium-ion batteries from the EVs become to an emerging concern. Recycling the chemical materials is the conventional solution to deal with the retired EV batteries. However, it will be a great waste if these EV batteries are disposed as scrap batteries for recycling process. Although these retired EV batteries can no longer meet the energy or power for the EVs, they still have considerable residual value for other applications. Developing the management strategies for the retired lithium-ion batteries in second use applications will be one of the focuses of future research.

Publication List

Journal papers

1. Liu, X. and Li, K., 2020. Energy storage devices in electrified railway systems: A review. Transportation Safety and Environment, 2(3), pp.183-201.
2. Liu, C., Li, K., Liu, X. and Wang, Y., 2020. Distributed unknown input and state estimation for nonlinear multi-agent systems with applications to battery management. CSEE Journal of Power and Energy Systems.
3. Rente, B., Fabian, M., Vidakovic, M., Liu, X., Li, X., Li, K., Sun, T. and Grattan, K.T., 2020. Lithium-Ion battery state-of-charge estimator based on FBG-based strain sensor and employing machine learning. IEEE Sensors Journal, 21(2), pp.1453-1460.
4. Li, Y., Li, K., Liu, X. and Zhang, L., 2020. Fast battery capacity estimation using convolutional neural networks. Transactions of the Institute of Measurement and Control, p.0142331220966425.
5. Li, Y., Li, K., Liu, X., Wang, Y. and Zhang, L., 2021. Lithium-ion battery capacity estimation—A pruned convolutional neural network approach assisted with transfer learning. Applied Energy, 285, p.116410.

Conference papers

1. Liu, X., Li, K. and Li, X., 2018. The electrochemical performance and applications of several popular lithium-ion batteries for electric vehicles-a review. Advances in Green Energy Systems and Smart Grid, pp.201-213.

Papers under preparation

1. Liu, X. and Li, K. State of charge estimation of lithium-ion batteries based on a temperature-compensated dual polarisation battery model using extended Kalman filter.
2. Liu, X., Li, K., Li X, Rente, B., Fabian, M. and Sun, T. A data-driven based temperature calibration method for Fiber Bragg-grating sensors in real-time battery temperature monitoring application.
3. Liu, X., Li, K., Li X, Rente, B., Fabian, M. and Sun, T. Battery SOC estimation aided with non-embedded FBG strain sensors.

References

[1] Y. Nishi, “The development of lithium ion secondary batteries,” The Chemical Record, vol. 1, no. 5, pp. 406–413, 2001. xvii, 3

[2] V. Johnson, “Battery performance models in advisor,” Journal of power sources, vol. 110, no. 2, pp. 321–329, 2002. xvii, 35

[3] S. Haykin, Kalman filtering and neural networks, vol. 47. John Wiley & Sons, 2004. xviii, 124

[4] P. Agreement, “Paris agreement,” in Report of the Conference of the Parties to the United Nations Framework Convention on Climate Change (21st Session, 2015: Paris). Retrived December, vol. 4, p. 2017, HeinOnline, 2015. 1

[5] S. Koohi-Fayegh and M. A. Rosen, “A review of energy storage types, applications and recent developments,” Journal of Energy Storage, vol. 27, p. 101047, 2020. 1

[6] X. Liu and K. Li, “Energy storage devices in electrified railway systems: A review,” Transportation Safety and Environment, vol. 2, no. 3, pp. 183–201, 2020. 2

[7] A. Yoshino, “The birth of the lithium-ion battery,” Angewandte Chemie International Edition, vol. 51, no. 24, pp. 5798–5800, 2012. 2

[8] M. Li, J. Lu, Z. Chen, and K. Amine, “30 years of lithium-ion batteries,” Advanced Materials, vol. 30, no. 33, p. 1800561, 2018. 2

[9] M. Sabri, K. A. Danapalasingam, and M. F. Rahmat, “A review on hybrid electric vehicles architecture and energy management strategies,” Renewable and Sustainable Energy Reviews, vol. 53, pp. 1433–1442, 2016. 4

[10] K. Chau and Y. Wong, “Overview of power management in hybrid electric vehicles,” Energy conversion and management, vol. 43, no. 15, pp. 1953–1968, 2002. 4

[11] L. Rambaldi, E. Bocci, and F. Orecchini, “Preliminary experimental evaluation of a four wheel motors, batteries plus ultracapacitors and series hybrid powertrain,” Applied Energy, vol. 88, no. 2, pp. 442–448, 2011. 5

[12] S. S. Williamson and A. Emadi, “Comparative assessment of hybrid electric and fuel cell vehicles based on comprehensive well-to-wheels efficiency analysis,” IEEE transactions on vehicular technology, vol. 54, no. 3, pp. 856–862, 2005. 5

[13] S. Campanari, G. Manzolini, and F. G. De la Iglesia, “Energy analysis of electric vehicles using batteries or fuel cells through well-to-wheel driving cycle simulations,” Journal of Power Sources, vol. 186, no. 2, pp. 464–477, 2009. 5

[14] M. P. Hekkert, F. H. Hendriks, A. P. Faaij, and M. L. Neelis, “Natural gas as an alternative to crude oil in automotive fuel chains well-to-wheel analysis and transition strategy development,” Energy policy, vol. 33, no. 5, pp. 579–594, 2005. 5

[15] T. Feehally, A. Forsyth, R. Todd, M. Foster, D. Gladwin, D. Stone, and

D. Strickland, “Battery energy storage systems for the electricity grid: Uk research facilities,” 2016. 5

[16] I. Atteya, N. R. Fahmi, D. R. Strickland, and H. Ashour, “Utilization of battery energy storage systems (bess) in smart grid: A review,” Renewable Energy and Power Quality Journal, vol. 1, no. 14, pp. 855–861, 2016. 5

[17] J. Lin, X. Liu, S. Li, C. Zhang, and S. Yang, “A review on recent progress, challenges and perspective of battery thermal management system,” International Journal of Heat and Mass Transfer, vol. 167, p. 120834, 2021. 10

[18] X. Hu, F. Feng, K. Liu, L. Zhang, J. Xie, and B. Liu, “State estimation for advanced battery management: Key challenges and future trends,” Renewable and Sustainable Energy Reviews, vol. 114, p. 109334, 2019. 10

[19] B. Balasingam, M. Ahmed, and K. Pattipati, “Battery management systems—challenges and some solutions,” Energies, vol. 13, no. 11, p. 2825, 2020. 10

[20] S. Ma, M. Jiang, P. Tao, C. Song, J. Wu, J. Wang, T. Deng, and W. Shang, “Temperature effect and thermal impact in lithium-ion batteries: A review,” Progress in Natural Science: Materials International, vol. 28, no. 6, pp. 653–666, 2018. 11

[21] P. Kurzweil, “Gaston planté and his invention of the lead–acid battery—the genesis of the first practical rechargeable battery,” Journal of Power Sources, vol. 195, no. 14, pp. 4424–4434, 2010. 20

[22] S. Vazquez, S. M. Lukic, E. Galvan, L. G. Franquelo, and J. M. Carrasco, “Energy storage systems for transport and grid applications,” IEEE

Transactions on Industrial Electronics, vol. 57, no. 12, pp. 3881–3895, 2010. 21

[23] P. Ruetschi, "Aging mechanisms and service life of lead–acid batteries," Journal of power sources, vol. 127, no. 1-2, pp. 33–44, 2004. 21

[24] B. B. McKeon, J. Furukawa, and S. Fenstermacher, "Advanced lead–acid batteries and the development of grid-scale energy storage systems," Proceedings of the IEEE, vol. 102, no. 6, pp. 951–963, 2014. 21

[25] P. T. Moseley, D. A. Rand, and K. Peters, "Enhancing the performance of lead–acid batteries with carbon–in pursuit of an understanding," Journal of Power Sources, vol. 295, pp. 268–274, 2015. 21

[26] G. Liu, Y. Yu, J. Hou, W. Xue, X. Liu, Y. Liu, W. Wang, A. Alsaedi, T. Hayat, and Z. Liu, "An ecological risk assessment of heavy metal pollution of the agricultural ecosystem near a lead-acid battery factory," Ecological indicators, vol. 47, pp. 210–218, 2014. 21

[27] F. Putois, "Market for nickel-cadmium batteries," Journal of Power Sources, vol. 57, no. 1-2, pp. 67–70, 1995. 21

[28] C. Pillot, "The rechargeable battery market and main trends 2014–2025," in 31st International Battery Seminar & Exhibit, 2015. 21, 23

[29] T. B. Reddy, "Linden's handbook of batteries," New York, USA, 2011. 21

[30] V. G. Lacerda, A. B. Mageste, I. J. B. Santos, L. H. M. Da Silva, and M. d. C. H. Da Silva, "Separation of cd and ni from ni–cd batteries by an environmentally safe methodology employing aqueous two-phase systems," Journal of Power Sources, vol. 193, no. 2, pp. 908–913, 2009. 22

[31] T. Oshima, M. Kajita, and A. Okuno, “Development of sodium-sulfur batteries,” International Journal of Applied Ceramic Technology, vol. 1, no. 3, pp. 269–276, 2004. 22

[32] H. Chen, T. N. Cong, W. Yang, C. Tan, Y. Li, and Y. Ding, “Progress in electrical energy storage system: A critical review,” Progress in natural science, vol. 19, no. 3, pp. 291–312, 2009. 22

[33] A. González-Gil, R. Palacin, and P. Batty, “Sustainable urban rail systems: Strategies and technologies for optimal management of regenerative braking energy,” Energy conversion and management, vol. 75, pp. 374–388, 2013. 22

[34] M. R. Palacin, “Recent advances in rechargeable battery materials: a chemist’s perspective,” Chemical Society Reviews, vol. 38, no. 9, pp. 2565–2575, 2009. 22

[35] C.-H. Dustmann, “Advances in zebra batteries,” Journal of Power Sources, vol. 127, no. 1-2, pp. 85–92, 2004. 23

[36] R. Carter, L. Oakes, A. Douglas, N. Muralidharan, A. P. Cohn, and C. L. Pint, “A sugar-derived room-temperature sodium sulfur battery with long term cycling stability,” Nano letters, vol. 17, no. 3, pp. 1863–1869, 2017. 23

[37] D. Kumar, S. B. Kuhar, and D. Kanchan, “Room temperature sodium-sulfur batteries as emerging energy source,” Journal of Energy Storage, vol. 18, pp. 133–148, 2018. 23

[38] Y.-X. Wang, B. Zhang, W. Lai, Y. Xu, S.-L. Chou, H.-K. Liu, and S.-X. Dou, “Room-temperature sodium-sulfur batteries: A comprehensive review on research progress and cell chemistry,” Advanced Energy Materials, vol. 7, no. 24, p. 1602829, 2017. 23

[39] X. Liu, K. Li, and X. Li, “The electrochemical performance and applications of several popular lithium-ion batteries for electric vehicles-a review,” in Advances in Green Energy Systems and Smart Grid, pp. 201–213, Springer, 2018. 23, 24

[40] Y. Zou, X. Hu, H. Ma, and S. E. Li, “Combined state of charge and state of health estimation over lithium-ion battery cell cycle lifespan for electric vehicles,” Journal of Power Sources, vol. 273, pp. 793–803, 2015. 24, 44, 147

[41] J. Jaguemont, L. Boulon, and Y. Dubé, “A comprehensive review of lithium-ion batteries used in hybrid and electric vehicles at cold temperatures,” Applied Energy, vol. 164, pp. 99–114, 2016. 24

[42] Y. Ding, Z. P. Cano, A. Yu, J. Lu, and Z. Chen, “Automotive li-ion batteries: current status and future perspectives,” Electrochemical Energy Reviews, vol. 2, no. 1, pp. 1–28, 2019. 24

[43] C. Sandhya, B. John, and C. Gouri, “Lithium titanate as anode material for lithium-ion cells: a review,” Ionics, vol. 20, no. 5, pp. 601–620, 2014. 24

[44] N. Nitta, F. Wu, J. T. Lee, and G. Yushin, “Li-ion battery materials: present and future,” Materials today, vol. 18, no. 5, pp. 252–264, 2015. 24

[45] W. Wang, Q. Luo, B. Li, X. Wei, L. Li, and Z. Yang, “Recent progress in redox flow battery research and development,” Advanced Functional Materials, vol. 23, no. 8, pp. 970–986, 2013. 25

[46] P. Alotto, M. Guarnieri, and F. Moro, “Redox flow batteries for the storage of renewable energy: A review,” Renewable and Sustainable Energy Reviews, vol. 29, pp. 325–335, 2014. 25

[47] J. Campillo, N. Ghaviha, N. Zimmerman, and E. Dahlquist, "Flow batteries use potential in heavy vehicles," in Electrical Systems for Aircraft, Railway, Ship Propulsion and Road Vehicles (ESARS), 2015 International Conference on, pp. 1–6, IEEE, 2015. 25

[48] J. R. Belt, "Battery test manual for plug-in hybrid electric vehicles," tech. rep., Idaho National Laboratory (INL), 2010. 27

[49] M. Petzl and M. A. Danzer, "Advancements in ocv measurement and analysis for lithium-ion batteries," IEEE Transactions on energy conversion, vol. 28, no. 3, pp. 675–681, 2013. 28

[50] M. A. Roscher, O. Bohlen, and J. Vetter, "Ocv hysteresis in li-ion batteries including two-phase transition materials," International Journal of Electrochemistry, vol. 2011, 2011. 29

[51] A. A.-H. Hussein, N. Kutkut, and I. Batarseh, "A hysteresis model for a lithium battery cell with improved transient response," in Applied Power Electronics Conference and Exposition (APEC), 2011 Twenty-Sixth Annual IEEE, pp. 1790–1794, IEEE, 2011. 29

[52] W. Waag, S. Käbitz, and D. U. Sauer, "Experimental investigation of the lithium-ion battery impedance characteristic at various conditions and aging states and its influence on the application," Applied Energy, vol. 102, pp. 885–897, 2013. 30

[53] M. Ecker, J. B. Gerschler, J. Vogel, S. Käbitz, F. Hust, P. Dechent, and D. U. Sauer, "Development of a lifetime prediction model for lithium-ion batteries based on extended accelerated aging test data," Journal of Power Sources, vol. 215, pp. 248–257, 2012. 30

[54] D. MacNeil, Z. Lu, Z. Chen, and J. R. Dahn, “A comparison of the electrode/electrolyte reaction at elevated temperatures for various li-ion battery cathodes,” Journal of power sources, vol. 108, no. 1-2, pp. 8–14, 2002. 30

[55] A. Hammami, N. Raymond, and M. Armand, “Lithium-ion batteries: Runaway risk of forming toxic compounds,” Nature, vol. 424, no. 6949, p. 635, 2003. 30

[56] X. Feng, M. Fang, X. He, M. Ouyang, L. Lu, H. Wang, and M. Zhang, “Thermal runaway features of large format prismatic lithium ion battery using extended volume accelerating rate calorimetry,” Journal of Power Sources, vol. 255, pp. 294–301, 2014. 30

[57] Z. Ling, Z. Zhang, G. Shi, X. Fang, L. Wang, X. Gao, Y. Fang, T. Xu, S. Wang, and X. Liu, “Review on thermal management systems using phase change materials for electronic components, li-ion batteries and photovoltaic modules,” Renewable and Sustainable Energy Reviews, vol. 31, pp. 427–438, 2014. 31

[58] M. Petzl, M. Kasper, and M. A. Danzer, “Lithium plating in a commercial lithium-ion battery–a low-temperature aging study,” Journal of Power Sources, vol. 275, pp. 799–807, 2015. 31, 83

[59] Z. Li, J. Huang, B. Y. Liaw, V. Metzler, and J. Zhang, “A review of lithium deposition in lithium-ion and lithium metal secondary batteries,” Journal of power sources, vol. 254, pp. 168–182, 2014. 31

[60] H. Teng, Y. Ma, K. Yeow, and M. Thelliez, “An analysis of a lithium-ion battery system with indirect air cooling and warm-up,” SAE International Journal of Passenger Cars-Mechanical Systems, vol. 4, no. 2011-01-2249, pp. 1343–1357, 2011. 31

[61] X. Li, F. He, and L. Ma, “Thermal management of cylindrical batteries investigated using wind tunnel testing and computational fluid dynamics simulation,” Journal of power sources, vol. 238, pp. 395–402, 2013. 31

[62] Z. Ling, X. Wen, Z. Zhang, X. Fang, and T. Xu, “Warming-up effects of phase change materials on lithium-ion batteries operated at low temperatures,” Energy Technology, vol. 4, no. 9, pp. 1071–1076, 2016. 31

[63] G. Zhang, S. Ge, T. Xu, X.-G. Yang, H. Tian, and C.-Y. Wang, “Rapid self-heating and internal temperature sensing of lithium-ion batteries at low temperatures,” Electrochimica Acta, vol. 218, pp. 149–155, 2016. 31

[64] L. Li, S. Basu, Y. Wang, Z. Chen, P. Hundekar, B. Wang, J. Shi, Y. Shi, S. Narayanan, and N. Koratkar, “Self-heating–induced healing of lithium dendrites,” Science, vol. 359, no. 6383, pp. 1513–1516, 2018. 31

[65] Y. Ji and C. Y. Wang, “Heating strategies for li-ion batteries operated from subzero temperatures,” Electrochimica Acta, vol. 107, pp. 664–674, 2013. 31

[66] A. Barré, B. Deguilhem, S. Grolleau, M. Gérard, F. Suard, and D. Riu, “A review on lithium-ion battery ageing mechanisms and estimations for automotive applications,” Journal of Power Sources, vol. 241, pp. 680–689, 2013. 31, 32, 33

[67] D. Abraham, E. Reynolds, E. Sammann, A. Jansen, and D. Dees, “Aging characteristics of high-power lithium-ion cells with lini0. 8co0. 15al0. 05o2 and li4/3ti5/3o4 electrodes,” Electrochimica Acta, vol. 51, no. 3, pp. 502–510, 2005. 31

[68] Q. Zhang and R. E. White, “Capacity fade analysis of a lithium ion cell,” Journal of Power Sources, vol. 179, no. 2, pp. 793–798, 2008. 31

[69] M. Wohlfahrt-Mehrens, C. Vogler, and J. Garche, “Aging mechanisms of lithium cathode materials,” Journal of power sources, vol. 127, no. 1-2, pp. 58–64, 2004. 32

[70] H. Buqa, A. Würsig, J. Vetter, M. Spahr, F. Krumeich, and P. Novák, “Sei film formation on highly crystalline graphitic materials in lithium-ion batteries,” Journal of power sources, vol. 153, no. 2, pp. 385–390, 2006. 32

[71] S. J. An, J. Li, C. Daniel, D. Mohanty, S. Nagpure, and D. L. Wood III, “The state of understanding of the lithium-ion-battery graphite solid electrolyte interphase (sei) and its relationship to formation cycling,” Carbon, vol. 105, pp. 52–76, 2016. 32

[72] I. Bloom, B. Cole, J. Sohn, S. Jones, E. Polzin, V. Battaglia, G. Henriksen, C. Motloch, R. Richardson, T. Unkelhaeuser, et al., “An accelerated calendar and cycle life study of li-ion cells,” Journal of Power Sources, vol. 101, no. 2, pp. 238–247, 2001. 32, 45

[73] S. Zhang, K. Xu, and T. Jow, “Electrochemical impedance study on the low temperature of li-ion batteries,” Electrochimica acta, vol. 49, no. 7, pp. 1057–1061, 2004. 32

[74] M. Ecker, N. Nieto, S. Käbitz, J. Schmalstieg, H. Blanke, A. Warnecke, and D. U. Sauer, “Calendar and cycle life study of li (nimnco) o2-based 18650 lithium-ion batteries,” Journal of Power Sources, vol. 248, pp. 839–851, 2014. 32, 33

[75] K. Nunotani, F. Yoshida, Y. Kamiya, Y. Daisho, K. Abe, M. Kono, and H. Matsuo, “Development and performance evaluation of lithium iron phosphate battery with superior rapid charging performance—second report:

Evaluation of battery capacity loss characteristics," in Vehicle Power and Propulsion Conference (VPPC), 2011 IEEE, pp. 1–4, IEEE, 2011. 32

[76] E. Thomas, I. Bloom, J. Christophersen, and V. Battaglia, "Statistical methodology for predicting the life of lithium-ion cells via accelerated degradation testing," Journal of Power Sources, vol. 184, no. 1, pp. 312–317, 2008. 32

[77] J. R. Belt, C. D. Ho, C. G. Motloch, T. J. Miller, and T. Q. Duong, "A capacity and power fade study of li-ion cells during life cycle testing," Journal of Power Sources, vol. 123, no. 2, pp. 241–246, 2003. 33

[78] G. Ning, B. Haran, and B. N. Popov, "Capacity fade study of lithium-ion batteries cycled at high discharge rates," Journal of Power Sources, vol. 117, no. 1-2, pp. 160–169, 2003. 33

[79] A. Fotouhi, D. J. Auger, K. Propp, S. Longo, and M. Wild, "A review on electric vehicle battery modelling: From lithium-ion toward lithium–sulphur," Renewable and Sustainable Energy Reviews, vol. 56, pp. 1008–1021, 2016. 34

[80] X. Han, M. Ouyang, L. Lu, and J. Li, "Simplification of physics-based electrochemical model for lithium ion battery on electric vehicle. part i: Diffusion simplification and single particle model," Journal of Power Sources, vol. 278, pp. 802–813, 2015. 34

[81] W. Luo, C. Lyu, L. Wang, and L. Zhang, "A new extension of physics-based single particle model for higher charge–discharge rates," Journal of Power Sources, vol. 241, pp. 295–310, 2013. 34

[82] S. J. Moura, F. B. Argomedo, R. Klein, A. Mirtabatabaei, and M. Krstic,

“Battery state estimation for a single particle model with electrolyte dynamics,” IEEE Transactions on Control Systems Technology, vol. 25, no. 2, pp. 453–468, 2016. 34

[83] N. Lotfi, J. Li, R. G. Landers, and J. Park, “Li-ion battery state of health estimation based on an improved single particle model,” in 2017 American Control Conference (ACC), pp. 86–91, IEEE, 2017. 34

[84] M. Doyle, T. F. Fuller, and J. Newman, “Modeling of galvanostatic charge and discharge of the lithium/polymer/insertion cell,” Journal of the Electrochemical society, vol. 140, no. 6, p. 1526, 1993. 34

[85] X. Song, Y. Lu, F. Wang, X. Zhao, and H. Chen, “A coupled electro-chemo-mechanical model for all-solid-state thin film li-ion batteries: The effects of bending on battery performances,” Journal of Power Sources, vol. 452, p. 227803, 2020. 34

[86] M. Xu, R. Wang, P. Zhao, and X. Wang, “Fast charging optimization for lithium-ion batteries based on dynamic programming algorithm and electrochemical-thermal-capacity fade coupled model,” Journal of Power Sources, vol. 438, p. 227015, 2019. 34

[87] S.-c. Yang, Y. Hua, D. Qiao, Y.-b. Lian, Y.-w. Pan, and Y.-l. He, “A coupled electrochemical-thermal-mechanical degradation modelling approach for lifetime assessment of lithium-ion batteries,” Electrochimica Acta, vol. 326, p. 134928, 2019. 34

[88] X. Hu, S. Li, and H. Peng, “A comparative study of equivalent circuit models for li-ion batteries,” Journal of Power Sources, vol. 198, pp. 359–367, 2012. 36

[89] H. Zhang and M.-Y. Chow, "Comprehensive dynamic battery modeling for phev applications," in Power and Energy Society General Meeting, 2010 IEEE, pp. 1–6, IEEE, 2010. 36

[90] C. M. Shepherd, "Design of primary and secondary cells: Ii. an equation describing battery discharge," Journal of the Electrochemical Society, vol. 112, no. 7, p. 657, 1965. 37, 119

[91] L. Unnewehr and S. Naser, Electric vehicle technology. John Wiley and Sons, New York, NY, 1982. 37, 119

[92] H. Fang, X. Zhao, Y. Wang, Z. Sahinoglu, T. Wada, S. Hara, and R. A. De Callafon, "State-of-charge estimation for batteries: A multi-model approach," in 2014 American Control Conference, pp. 2779–2785, IEEE, 2014. 37, 119

[93] G. L. Plett, "Extended kalman filtering for battery management systems of lipb-based hev battery packs: Part 3. state and parameter estimation," Journal of Power sources, vol. 134, no. 2, pp. 277–292, 2004. 37, 119

[94] H. He, R. Xiong, H. Guo, and S. Li, "Comparison study on the battery models used for the energy management of batteries in electric vehicles," Energy Conversion and Management, vol. 64, pp. 113–121, 2012. 37, 119

[95] X. Tang, Y. Wang, and Z. Chen, "A method for state-of-charge estimation of lifepo4 batteries based on a dual-circuit state observer," Journal of Power Sources, vol. 296, pp. 23–29, 2015. 37, 119

[96] X. Liu, D. Guo, Y. Chen, H. Geng, G. Yang, L. Lu, and M. Ouyang, "Bp neural network model of lithium-iron phosphate battery based on step-discharge current response," in 2018 IEEE International Power Electronics

and Application Conference and Exposition (PEAC), pp. 1–6, IEEE, 2018. 38

[97] C. Zhang, Y. Zhu, G. Dong, and J. Wei, "Data-driven lithium-ion battery states estimation using neural networks and particle filtering," International Journal of Energy Research, vol. 43, no. 14, pp. 8230–8241, 2019. 38

[98] W. Junping, C. Quanshi, and C. Binggang, "Support vector machine based battery model for electric vehicles," Energy conversion and management, vol. 47, no. 7-8, pp. 858–864, 2006. 38

[99] C. Zhang, Z. Yang, and K. Li, "Modeling of electric vehicle batteries using rbf neural networks," in 2014 International Conference on Computing, Management and Telecommunications (ComManTel), pp. 116–121, IEEE, 2014. 39

[100] K. Li, J.-X. Peng, and G. W. Irwin, "A fast nonlinear model identification method," IEEE Transactions on Automatic Control, vol. 50, no. 8, pp. 1211–1216, 2005. 39

[101] S. Rodrigues, N. Munichandraiah, and A. Shukla, "A review of state-of-charge indication of batteries by means of ac impedance measurements," Journal of power Sources, vol. 87, no. 1-2, pp. 12–20, 2000. 40

[102] F. Orsini, M. Dollé, and J.-M. Tarascon, "Impedance study of the li/electrolyte interface upon cycling," Solid State Ionics, vol. 135, no. 1-4, pp. 213–221, 2000. 40

[103] T. Gallien, H. Krenn, R. Fischer, S. Lauterbach, B. Schweighofer, and H. Wegleiter, "Magnetism versus lifepo 4 battery's state of charge: A feasibility study for magnetic-based charge monitoring," IEEE Transactions on

Instrumentation and Measurement, vol. 64, no. 11, pp. 2959–2964, 2015. 40

[104] C. Lin, A. Tang, and J. Xing, "Evaluation of electrochemical models based battery state-of-charge estimation approaches for electric vehicles," Applied Energy, vol. 207, pp. 394–404, 2017. 40, 41

[105] R. Xiong, L. Li, and Q. Yu, "Improved single particle model based state of charge and capacity monitoring of lithium-ion batteries," in 2019 IEEE 89th Vehicular Technology Conference (VTC2019-Spring), pp. 1–5, IEEE, 2019. 40, 41

[106] Y. Wang, C. Liu, R. Pan, and Z. Chen, "Modeling and state-of-charge prediction of lithium-ion battery and ultracapacitor hybrids with a co-estimator," Energy, vol. 121, pp. 739–750, 2017. 40, 41, 125

[107] C. Lin, H. Mu, R. Xiong, and W. Shen, "A novel multi-model probability battery state of charge estimation approach for electric vehicles using h-infinity algorithm," Applied energy, vol. 166, pp. 76–83, 2016. 40, 41

[108] X. Hu, S. Li, H. Peng, and F. Sun, "Robustness analysis of state-of-charge estimation methods for two types of li-ion batteries," Journal of power sources, vol. 217, pp. 209–219, 2012. 40

[109] M. Charkhgard and M. Farrokhi, "State-of-charge estimation for lithium-ion batteries using neural networks and ekf," IEEE transactions on industrial electronics, vol. 57, no. 12, pp. 4178–4187, 2010. 41, 42

[110] M. Hossain Lipu, M. Hannan, A. Hussain, and M. Saad, "Optimal bp neural network algorithm for state of charge estimation of lithium-ion battery using pso with pca feature selection," Journal of Renewable and Sustainable Energy, vol. 9, no. 6, p. 064102, 2017. 41, 42

[111] G. Welch, G. Bishop, et al., "An introduction to the kalman filter," 1995. 41

[112] S. Afshar, K. Morris, and A. Khajepour, "State-of-charge estimation using an ekf-based adaptive observer," IEEE Transactions on Control Systems Technology, vol. 27, no. 5, pp. 1907–1923, 2018. 41

[113] C. Zhang, K. Li, L. Pei, and C. Zhu, "An integrated approach for real-time model-based state-of-charge estimation of lithium-ion batteries," Journal of Power Sources, vol. 283, pp. 24–36, 2015. 41

[114] W. Wang, X. Wang, C. Xiang, C. Wei, and Y. Zhao, "Unscented kalman filter-based battery soc estimation and peak power prediction method for power distribution of hybrid electric vehicles," Ieee Access, vol. 6, pp. 35957–35965, 2018. 41

[115] N. Peng, S. Zhang, X. Guo, and X. Zhang, "Online parameters identification and state of charge estimation for lithium-ion batteries using improved adaptive dual unscented kalman filter," International Journal of Energy Research, vol. 45, no. 1, pp. 975–990, 2021. 41

[116] K. Dai, J. Wang, and H. He, "An improved soc estimator using time-varying discrete sliding mode observer," IEEE Access, vol. 7, pp. 115463–115472, 2019. 41

[117] L. Lu, X. Han, J. Li, J. Hua, and M. Ouyang, "A review on the key issues for lithium-ion battery management in electric vehicles," Journal of power sources, vol. 226, pp. 272–288, 2013. 42

[118] S. Li, K. Li, E. Xiao, and C.-K. Wong, "Joint soc and soh estimation for zinc–nickel single-flow batteries," IEEE Transactions on Industrial Electronics, vol. 67, no. 10, pp. 8484–8494, 2019. 44, 147

[119] Q. Yu, R. Xiong, R. Yang, and M. G. Pecht, "Online capacity estimation for lithium-ion batteries through joint estimation method," Applied Energy, vol. 255, p. 113817, 2019. 44, 147

[120] X. Hu, H. Jiang, F. Feng, and B. Liu, "An enhanced multi-state estimation hierarchy for advanced lithium-ion battery management," Applied Energy, vol. 257, p. 114019, 2020. 44, 147

[121] P. A. Ioannou and J. Sun, Robust adaptive control. Courier Corporation, 2012. 44, 147

[122] M. V. Micea, L. Ungurean, G. N. Cârstoiu, and V. Groza, "Online state-of-health assessment for battery management systems," IEEE Transactions on Instrumentation and Measurement, vol. 60, no. 6, pp. 1997–2006, 2011. 45

[123] K.-H. Tseng, J.-W. Liang, W. Chang, and S.-C. Huang, "Regression models using fully discharged voltage and internal resistance for state of health estimation of lithium-ion batteries," energies, vol. 8, no. 4, pp. 2889–2907, 2015. 45

[124] X. Han, M. Ouyang, L. Lu, and J. Li, "A comparative study of commercial lithium ion battery cycle life in electric vehicle: Capacity loss estimation," Journal of Power Sources, vol. 268, pp. 658–669, 2014. 45, 46

[125] J. Wang, P. Liu, J. Hicks-Garner, E. Sherman, S. Soukiazian, M. Verbrugge, H. Tataria, J. Musser, and P. Finamore, "Cycle-life model for graphite-lifepo4 cells," Journal of Power Sources, vol. 196, no. 8, pp. 3942–3948, 2011. 45

[126] M. Dalal, J. Ma, and D. He, "Lithium-ion battery life prognostic health management system using particle filtering framework," Proceedings of the

Institution of Mechanical Engineers, Part O: Journal of Risk and Reliability, vol. 225, no. 1, pp. 81–90, 2011. 46

[127] Y. E. A. Eldahab, N. H. Saad, and A. Zekry, "Enhancing the design of battery charging controllers for photovoltaic systems," Renewable and Sustainable Energy Reviews, vol. 58, pp. 646–655, 2016. 47

[128] B. Arabsalmanabadi, N. Tashakor, A. Javadi, and K. Al-Haddad, "Charging techniques in lithium-ion battery charger: Review and new solution," in IECON 2018-44th Annual Conference of the IEEE Industrial Electronics Society, pp. 5731–5738, IEEE, 2018. 47

[129] K. Liu, K. Li, Z. Yang, C. Zhang, and J. Deng, "An advanced lithium-ion battery optimal charging strategy based on a coupled thermoelectric model," Electrochimica Acta, vol. 225, pp. 330–344, 2017. 47

[130] R. Xiong, L. Li, and J. Tian, "Towards a smarter battery management system: A critical review on battery state of health monitoring methods," Journal of Power Sources, vol. 405, pp. 18–29, 2018. 48, 147

[131] C. Weng, X. Feng, J. Sun, and H. Peng, "State-of-health monitoring of lithium-ion battery modules and packs via incremental capacity peak tracking," Applied Energy, vol. 180, pp. 360–368, 2016. 48

[132] J. Tian, R. Xiong, and Q. Yu, "Fractional-order model-based incremental capacity analysis for degradation state recognition of lithium-ion batteries," IEEE Transactions on Industrial Electronics, vol. 66, no. 2, pp. 1576–1584, 2018. 48

[133] M. Ouyang, Z. Chu, L. Lu, J. Li, X. Han, X. Feng, and G. Liu, "Low temperature aging mechanism identification and lithium deposition in a large

format lithium iron phosphate battery for different charge profiles," Journal of Power Sources, vol. 286, pp. 309–320, 2015. 48

[134] R. R. Richardson, C. R. Birkl, M. A. Osborne, and D. A. Howey, "Gaussian process regression for in situ capacity estimation of lithium-ion batteries," IEEE Transactions on Industrial Informatics, vol. 15, no. 1, pp. 127–138, 2018. 48

[135] X. Feng, J. Li, M. Ouyang, L. Lu, J. Li, and X. He, "Using probability density function to evaluate the state of health of lithium-ion batteries," Journal of Power Sources, vol. 232, pp. 209–218, 2013. 48, 144, 145

[136] L. Wang, C. Pan, L. Liu, Y. Cheng, and X. Zhao, "On-board state of health estimation of lifepo4 battery pack through differential voltage analysis," Applied energy, vol. 168, pp. 465–472, 2016. 48

[137] P. Pei, Q. Zhou, L. Wu, Z. Wu, J. Hua, and H. Fan, "Capacity estimation for lithium-ion battery using experimental feature interval approach," Energy, vol. 203, p. 117778, 2020. 48

[138] Y. Li, M. Abdel-Monem, R. Gopalakrishnan, M. Berecibar, E. Nanini-Maury, N. Omar, P. van den Bossche, and J. Van Mierlo, "A quick on-line state of health estimation method for li-ion battery with incremental capacity curves processed by gaussian filter," Journal of Power Sources, vol. 373, pp. 40–53, 2018. 48

[139] A. Eddahech, O. Briat, and J.-M. Vinassa, "Determination of lithium-ion battery state-of-health based on constant-voltage charge phase," Journal of Power Sources, vol. 258, pp. 218–227, 2014. 49

[140] M. Nascimento, M. S. Ferreira, and J. L. Pinto, “Real time thermal monitoring of lithium batteries with fiber sensors and thermocouples: A comparative study,” Measurement, vol. 111, pp. 260–263, 2017. 50, 89, 105

[141] J. Peng, S. Jia, H. Yu, X. Kang, S. Yang, and S. Xu, “Design and experiment of fbg sensors for temperature monitoring on external electrode of lithium-ion batteries,” IEEE Sensors Journal, vol. 21, no. 4, pp. 4628–4634, 2020. 50, 51

[142] M. Nascimento, T. Paixão, M. S. Ferreira, and J. L. Pinto, “Thermal mapping of a lithium polymer batteries pack with fbgs network,” Batteries, vol. 4, no. 4, p. 67, 2018. 50, 51

[143] S. Novais, M. Nascimento, L. Grande, M. F. Domingues, P. Antunes, N. Alberto, C. Leitão, R. Oliveira, S. Koch, G. T. Kim, et al., “Internal and external temperature monitoring of a li-ion battery with fiber bragg grating sensors,” Sensors, vol. 16, no. 9, p. 1394, 2016. 51, 84, 105

[144] J. Fleming, T. Amietszajew, E. McTurk, D. P. Towers, D. Greenwood, and R. Bhagat, “Development and evaluation of in-situ instrumentation for cylindrical li-ion cells using fibre optic sensors,” HardwareX, vol. 3, pp. 100–109, 2018. 51, 105

[145] L. W. Sommer, P. Kiesel, A. Ganguli, A. Lochbaum, B. Saha, J. Schwartz, C.-J. Bae, M. Alamgir, and A. Raghavan, “Fast and slow ion diffusion processes in lithium ion pouch cells during cycling observed with fiber optic strain sensors,” Journal of Power Sources, vol. 296, pp. 46–52, 2015. 51, 92

[146] J. Peng, X. Zhou, S. Jia, Y. Jin, S. Xu, and J. Chen, “High precision strain monitoring for lithium ion batteries based on fiber bragg grating sensors,”

Journal of Power Sources, vol. 433, p. 226692, 2019. 51, 52, 88, 89, 92, 105, 112

[147] C.-J. Bae, A. Manandhar, P. Kiesel, and A. Raghavan, "Monitoring the strain evolution of lithium-ion battery electrodes using an optical fiber bragg grating sensor," Energy technology, vol. 4, no. 7, pp. 851–855, 2016. 51, 52, 92, 105

[148] A. Raghavan, P. Kiesel, L. W. Sommer, J. Schwartz, A. Lochbaum, A. Hegyi, A. Schuh, K. Arakaki, B. Saha, A. Ganguli, et al., "Embedded fiber-optic sensing for accurate internal monitoring of cell state in advanced battery management systems part 1: Cell embedding method and performance," Journal of Power Sources, vol. 341, pp. 466–473, 2017. 51, 105

[149] A. Ganguli, B. Saha, A. Raghavan, P. Kiesel, K. Arakaki, A. Schuh, J. Schwartz, A. Hegyi, L. W. Sommer, A. Lochbaum, et al., "Embedded fiber-optic sensing for accurate internal monitoring of cell state in advanced battery management systems part 2: Internal cell signals and utility for state estimation," Journal of Power Sources, vol. 341, pp. 474–482, 2017. 51, 52, 92, 93, 105

[150] B. Rente, M. Fabian, M. Vidakovic, X. Liu, X. Li, K. Li, T. Sun, and K. Grattan, "Lithium-ion battery state-of-charge estimator based on fbg-based strain sensor and employing machine learning," IEEE Sensors Journal, 2020. 52, 105, 129

[151] Y. Xing, W. He, M. Pecht, and K. L. Tsui, "State of charge estimation of lithium-ion batteries using the open-circuit voltage at various ambient temperatures," Applied Energy, vol. 113, pp. 106–115, 2014. 56

[152] K.-T. Lee, M.-J. Dai, and C.-C. Chuang, “Temperature-compensated model for lithium-ion polymer batteries with extended kalman filter state-of-charge estimation for an implantable charger,” IEEE Transactions on Industrial Electronics, vol. 65, no. 1, pp. 589–596, 2017. 56

[153] X. Wu, X. Li, and J. Du, “State of charge estimation of lithium-ion batteries over wide temperature range using unscented kalman filter,” Ieee Access, vol. 6, pp. 41993–42003, 2018. 57

[154] H. He, R. Xiong, and J. Fan, “Evaluation of lithium-ion battery equivalent circuit models for state of charge estimation by an experimental approach,” Energies, vol. 4, no. 4, pp. 582–598, 2011. 57

[155] U. ABC, “Us abc electric vehicle battery test procedures manual, revision 2,” principal author: Gary Hunt, Idaho National Engineering Laboratory (INEL), US Department of Energy Idaho Field Office, DOE/ID-10479, Rev, vol. 2, 1996. 63

[156] X. Sun, J. Ji, B. Ren, C. Xie, and D. Yan, “Adaptive forgetting factor recursive least square algorithm for online identification of equivalent circuit model parameters of a lithium-ion battery,” Energies, vol. 12, no. 12, p. 2242, 2019. 65

[157] K. S. Ng, C.-S. Moo, Y.-P. Chen, and Y.-C. Hsieh, “Enhanced coulomb counting method for estimating state-of-charge and state-of-health of lithium-ion batteries,” Applied energy, vol. 86, no. 9, pp. 1506–1511, 2009. 74

[158] J. Li, Z. Du, R. E. Ruther, S. J. An, L. A. David, K. Hays, M. Wood, N. D. Phillip, Y. Sheng, C. Mao, et al., “Toward low-cost, high-energy density, and

high-power density lithium-ion batteries," Jom, vol. 69, no. 9, pp. 1484–1496, 2017. 83

[159] X. Feng, M. Ouyang, X. Liu, L. Lu, Y. Xia, and X. He, "Thermal runaway mechanism of lithium ion battery for electric vehicles: A review," Energy Storage Materials, vol. 10, pp. 246–267, 2018. 83

[160] S. Panchal, I. Dincer, M. Agelin-Chaab, R. Fraser, and M. Fowler, "Experimental and theoretical investigation of temperature distributions in a prismatic lithium-ion battery," International Journal of Thermal Sciences, vol. 99, pp. 204–212, 2016. 84

[161] C. Zhang, K. Li, and J. Deng, "Real-time estimation of battery internal temperature based on a simplified thermoelectric model," Journal of Power Sources, vol. 302, pp. 146–154, 2016. 84

[162] L. Raijmakers, D. Danilov, R.-A. Eichel, and P. Notten, "A review on various temperature-indication methods for li-ion batteries," Applied energy, vol. 240, pp. 918–945, 2019. 84

[163] Y. Zhao and Y. Liao, "Discrimination methods and demodulation techniques for fiber bragg grating sensors," Optics and Lasers in Engineering, vol. 41, no. 1, pp. 1–18, 2004. 84

[164] G. Pereira, M. McGugan, and L. P. Mikkelsen, "Method for independent strain and temperature measurement in polymeric tensile test specimen using embedded fbg sensors," Polymer Testing, vol. 50, pp. 125–134, 2016. 85, 88, 107

[165] Z. Kang, J. Sun, Y. Bai, and S. Jian, "Twin-core fiber-based erbium-doped fiber laser sensor for decoupling measurement of temperature and strain," IEEE Sensors Journal, vol. 15, no. 12, pp. 6828–6832, 2015. 85

[166] G. Yang, C. Leitão, Y. Li, J. Pinto, and X. Jiang, "Real-time temperature measurement with fiber bragg sensors in lithium batteries for safety usage," Measurement, vol. 46, no. 9, pp. 3166–3172, 2013. 85, 89, 105

[167] M. Nascimento, M. S. Ferreira, and J. L. Pinto, "Temperature fiber sensing of li-ion batteries under different environmental and operating conditions," Applied Thermal Engineering, vol. 149, pp. 1236–1243, 2019. 89

[168] Y. Lu, T. Ma, C. Yin, X. Xie, W. Tian, and S. Zhong, "Implementation of the fuzzy c-means clustering algorithm in meteorological data," International Journal of Database Theory and Application, vol. 6, no. 6, pp. 1–18, 2013. 90

[169] J. H. Lee, H. M. Lee, and S. Ahn, "Battery dimensional changes occurring during charge/discharge cycles—thin rectangular lithium ion and polymer cells," Journal of power sources, vol. 119, pp. 833–837, 2003. 91

[170] V. Agubra and J. Fergus, "Lithium ion battery anode aging mechanisms," Materials, vol. 6, no. 4, pp. 1310–1325, 2013. 93

[171] N. E. Huang, Z. Shen, S. R. Long, M. C. Wu, H. H. Shih, Q. Zheng, N.-C. Yen, C. C. Tung, and H. H. Liu, "The empirical mode decomposition and the hilbert spectrum for nonlinear and non-stationary time series analysis," Proceedings of the Royal Society of London. Series A: mathematical, physical and engineering sciences, vol. 454, no. 1971, pp. 903–995, 1998. 93

[172] A. Zeiler, R. Faltermeier, I. R. Keck, A. M. Tomé, C. G. Puntonet, and E. W. Lang, "Empirical mode decomposition-an introduction," in The 2010 International Joint Conference on Neural Networks (IJCNN), pp. 1–8, IEEE, 2010. 93

[173] Z. Shang-yue, L. Yuan-yuan, and Y. Gong-liu, “Emd interval thresholding denoising based on correlation coefficient to select relevant modes,” in 2015 34th Chinese Control Conference (CCC), pp. 4801–4806, IEEE, 2015. 94

[174] X. Lin, “Analytic analysis of the data-dependent estimation accuracy of battery equivalent circuit dynamics,” IEEE Control Systems Letters, vol. 1, no. 2, pp. 304–309, 2017. 104

[175] X. Lin, “Theoretical analysis of battery soc estimation errors under sensor bias and variance,” IEEE Transactions on Industrial Electronics, vol. 65, no. 9, pp. 7138–7148, 2018. 104

[176] A. Fortier, M. Tsao, N. D. Williard, Y. Xing, and M. G. Pecht, “Preliminary study on integration of fiber optic bragg grating sensors in li-ion batteries and in situ strain and temperature monitoring of battery cells,” Energies, vol. 10, no. 7, p. 838, 2017. 105

[177] M. Nascimento, S. Novais, M. S. Ding, M. S. Ferreira, S. Koch, S. Passerini, and J. L. Pinto, “Internal strain and temperature discrimination with optical fiber hybrid sensors in li-ion batteries,” Journal of Power Sources, vol. 410, pp. 1–9, 2019. 105

[178] W.-Y. Chang, “Estimation of the state of charge for a lfp battery using a hybrid method that combines a rbf neural network, an ols algorithm and aga,” International Journal of Electrical Power & Energy Systems, vol. 53, pp. 603–611, 2013. 109

[179] N. Guo, Y. Fang, Z. Tian, and S. Cao, “Research on soc fuzzy weighted algorithm based on ga-bp neural network and ampere integral method,” The Journal of Engineering, vol. 2019, no. 15, pp. 576–580, 2019. 109

[180] K. W. E. Cheng, B. Divakar, H. Wu, K. Ding, and H. F. Ho, "Battery-management system (bms) and soc development for electrical vehicles," IEEE transactions on vehicular technology, vol. 60, no. 1, pp. 76–88, 2010. 109

[181] Y. Li, K. Li, S. Li, and Y. Li, "Fra and ekf based state of charge estimation of zinc-nickel single flow batteries," in Advances in Green Energy Systems and Smart Grid, pp. 183–191, Springer, 2018. 109

[182] A. A.-H. Hussein and I. Batarseh, "An overview of generic battery models," in 2011 IEEE Power and Energy Society General Meeting, pp. 1–6, IEEE, 2011. 119

[183] S. J. Julier and J. K. Uhlmann, "Unscented filtering and nonlinear estimation," Proceedings of the IEEE, vol. 92, no. 3, pp. 401–422, 2004. 123

[184] A. Giannitrapani, N. Ceccarelli, F. Scortecci, and A. Garulli, "Comparison of ekf and ukf for spacecraft localization via angle measurements," IEEE Transactions on aerospace and electronic systems, vol. 47, no. 1, pp. 75–84, 2011. 123

[185] H. He, H. Qin, X. Sun, and Y. Shui, "Comparison study on the battery soc estimation with ekf and ukf algorithms," Energies, vol. 6, no. 10, pp. 5088–5100, 2013. 123